

Institut für Chemie  
Optical Spectroscopy and Chemical Imaging

---

A novel approach to study  
low-energy electron-induced damage  
to DNA oligonucleotides  
– *Influence of DNA sequence, topology and nucleobase modification*

Dissertation

zur Erlangung des akademischen Grades  
"doctor rerum naturalium"  
(Dr. rer. nat.)  
in der Wissenschaftsdisziplin "Physikalische Chemie"

eingereicht an der  
Mathematisch-Naturwissenschaftlichen Fakultät  
der Universität Potsdam

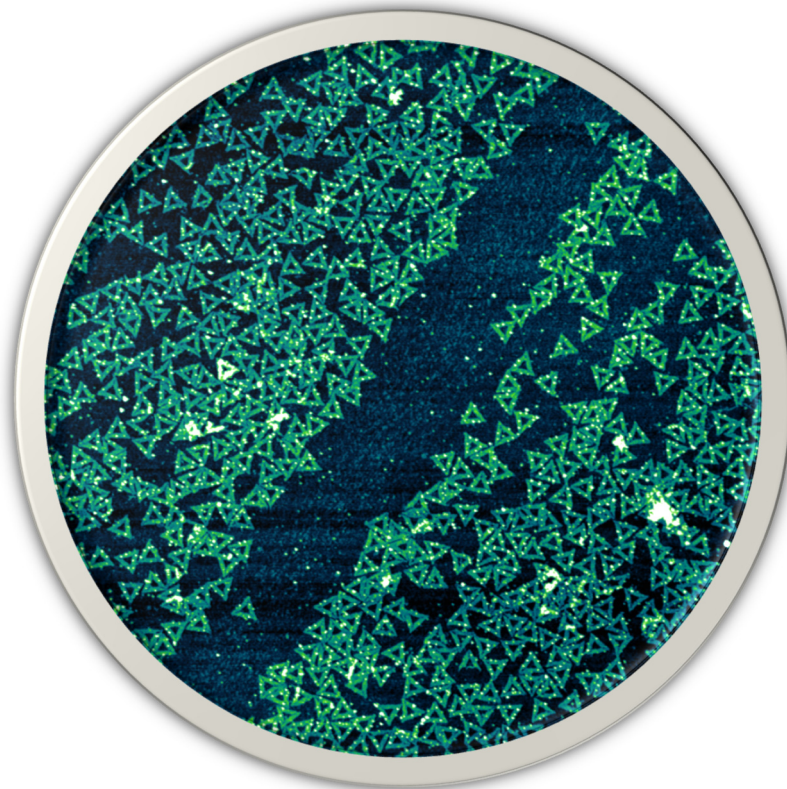
von  
Jenny Rackwitz  
geb. 02.05.1989 (Berlin)

**Potsdam, den 06.06.2016**

Gutachter: Prof. Dr. I. Bald, Universität Potsdam  
Prof. Dr. H. Sturm, Technische Universität Berlin  
Apl. Prof. Dr. S. Denifl, Universität Innsbruck

„There is a question I could ask you that has a definite correct answer – either yes or no – but it is logically impossible for you to give the correct answer. You might *know* what the correct answer is, but you cannot give it. Anybody other than you might possibly be able to give the correct answer, but you cannot! Can you figure out what question I could have in mind?”

*“to mock a mockingbird”, Raymond Smullyan  
(Oxford University Press, 2000)*





# Abstract

During radio- and chemoradiotherapy, high energy radiation generates a broad distribution of secondary low-energy electrons. These secondary electrons play a major role in DNA radiation damage. The present work investigates the energy and sequence dependent DNA backbone cleavage caused by such low-energy electrons. Well-defined oligonucleotide sequences were positioned on DNA origami triangles to achieve the quantitative determination of absolute strand break cross sections of the target oligonucleotides. The analysis was performed at a single-molecule level by atomic force microscopy, yielding the number of induced strand breaks as a function of fluence. From this correlation, the energy and sequence dependent strand break cross sections of various oligonucleotides have been determined and will be discussed in the present work.

To improve the fundamental understanding of DNA damage caused by radiosensitizers during chemoradiotherapy, two fluorinated nucleobases (5-fluorouracil <sup>5F</sup>U and 2-fluoro-adenine <sup>2F</sup>A) were incorporated into different oligonucleotide sequences and irradiated at 5.5 eV and 10 eV. <sup>2F</sup>A showed an increased sensitivity at 5.5 eV, while <sup>5F</sup>U had a constant strand break cross section at both energies. The neighboring nucleobases (A or T), as well as the amount of F-modified nucleobases in oligonucleotides of the same length seem to have no significant influence on the strand break cross section at 10 eV. Both F modified nucleobases showed a similar enhancement in strand breakage at 10 eV when compared to oligonucleotides containing their natural derivatives. In addition, an increased sensitivity towards 5.5 eV electrons was obtained for the A containing oligonucleotide in comparison with its strand break cross section at 10 eV.

In addition to modifications in the nucleotide, also the influence of topological effects in natural DNA sequences is investigated in this work. Since the telomere sequence is biologically relevant for chromosome protection and is known to fold complex topological systems, telomere derived oligonucleotides were irradiated at 10 eV. The results discussed in the following work indicate a sequence and cation dependent folding of G-hairpin, G-triplex and G-quadruplex structures in the telomere sequences. With increasing length of the oligonucleotide, both the variety of topology and the strand break cross sections increases. Addition of K<sup>+</sup> ions decreased the absolute strand break cross section for all sequences that are able to fold G-intermediates or G-quadruplexes, while the strand break cross section of intermixed telomere sequence was unchanged. The latter sequence furthermore revealed a decreased strand break cross section for the sequence with no neighboring G nucleobases, confirming the unique electronic properties resulting from G-stacking.



# Abstract (DE)

In der Medizin spielt die Bestrahlung von kanzerogenem Gewebe eine bedeutende Rolle. Die Strahlentherapie nutzt in der Regel hochenergetische Strahlung, welche in der Zelle unter anderem eine Vielzahl an niederenergetischen Sekundärelektronen generiert. Diese Sekundärelektronen können innerhalb der bestrahlten Zelle die DNA schädigen. Genutzt wird dieser Effekt besonders in der Radiochemotherapie, bei der das zu bestrahlende Gewebe mit radiosensitiven Medikamenten angereichert wird. Diese können verschiedene Prozesse in der Zelle, besonders im Bereich der DNA-Reproduktion manipulieren. In der vorliegenden Arbeit wird der Einfluss der direkten Einbettung zweier verschiedener fluorierter Nukleinbasen in DNA-Sequenzen auf den Wirkungsquerschnitt für Strangbrüche bei Elektronen-Bestrahlung untersucht. Des Weiteren wird der Einfluss der Topologie innerhalb eines Oligonukleotids auf die Sensitivität gegenüber niederenergetischen Elektronen diskutiert. Als Testsequenzen werden die menschliche Telomersequenz sowie mehrere Derivate verwendet. Da die Telomersequenz in großer Zahl an den Enden der Chromosomen lokalisiert ist, ist der Einfluss verschiedener Topologien auf die Sensitivität gegenüber niederenergetischen Elektronen von besonderer Bedeutung. Beide Aspekte, der Einfluss fluorierter Nukleinbasen und die Topologie innerhalb der Oligonukleotide auf die Wirkungsquerschnitte für Elektronen-induzierte Strangbrüche können durch die Anwendung der DNA-Origami-Technik quantitativ bestimmt werden. Die zu betrachtenden Oligonukleotidsequenzen werden auf dreieckigen DNA Origamis positioniert, wodurch eine Untersuchung auf Einzelmolekülniveau mittels Rasterkraftmikroskopie ermöglicht wird.

Die beiden fluorierten Nukleinbasen 2-Fluoradenin und 5-Fluoruracil erhöhen den Strangbruchwirkungsquerschnitt in identischen Oligonukleotidsequenzen bei der Bestrahlung mit 10 eV Elektronen. Bei 5.5 eV erhöhen sich die entsprechenden Wirkungsquerschnitte von Adenin- und 2-Fluoradenin-haltigen DNA-Sequenzen, der einer 5-Fluoruracil-haltigen Sequenz hingegen bleibt auf dem gleichen Niveau wie bei 10 eV. Basierend auf diesen und weiteren Ergebnissen lässt sich eine resonante Fragmentierung innerhalb der Einzelstrang-DNA vermuten. Die Anzahl der fluorierten Nukleinbasen innerhalb des gleichlangen Stranges sowie die benachbarte Nukleinbase verändern die Sensitivität gegenüber 10 eV Elektronen hingegen nur unwesentlich.

Betrachtungen der Telomersequenz und ihrer Derivate zeigen eine deutliche Verringerung der Sensitivität gegenüber 10 eV Elektronen bei G-Hairpin-, G-Triplex- und G-Quadruplex-Strukturen. Dabei erhöht sich durch zunehmende Stranglänge die

Anzahl an Faltungsmöglichkeiten, sowie die Sensitivität des Stranges. Die Strangfaltung wurde durch die Zugabe von  $K^+$  gefördert, was zu einer Absenkung der Strangbruchraten in gefalteten Strukturen führt. Als Konsequenz ergibt sich eine deutliche Steigerung der Sensitivität innerhalb der Telomersequenz gegenüber 10 eV Elektronen, wenn diese im ungefalteten Zustand vorliegt.

# Contents

1. Introduction.....	1
2. Theoretical and experimental basics	
2.1. Deoxyribonucleic acid (DNA).....	4
2.2. Dissociative electron attachment (DEA) in DNA.....	7
2.3. The telomere sequence in DNA.....	10
2.4. Radiosensitizers for cancer therapy .....	13
2.5. Established experiments to study LEE-induced fragmentation in DNA ....	16
2.6. Experimental methods .....	18
3. Development of a novel experimental approach for condensed phase DEA studies	
3.1. A vacuum chamber for irradiation.....	24
3.2. Characterization of the electron beam .....	29
3.3. Fluence calculation .....	34
3.4. AFM analysis.....	38
3.5. DNA origami preparation and stability .....	42
3.6. Two methods to determine absolute strand break cross sections .....	52
3.7. Biotin label for oligonucleotide visualization.....	55
4. Radiosensitizers – nucleobases modified with fluorine	
4.1. 2-Fluoroadenine ( <sup>2</sup> F A).....	56
4.2. 5-Fluoruracil .....	63
4.3. Discussion.....	67
5. Secondary structures - Telomere derived sequences	
5.1. Order of the nucleotides.....	76
5.2. Length dependency .....	78
5.3. Influence of loop base replacement .....	81
5.4. Influence of potassium ions on the topology .....	84
5.5. Conclusion .....	88
6. Summary.....	89

## II

7. Supplement	
7.1. Sample preparation.....	93
7.2. Chamber manual .....	97
7.3. Software .....	102
7.4. Ratios between the natural and F modified oligonucleotide sequences in chapter 4.....	115
References .....	117

## List of abbreviations

<sup>2</sup> F A	2-fluoroadenine
<sup>5</sup> F U	5-fluorouracil
A	adenine
AD	autodetachment
AFM	atom force microscopy
AGE	agarose gel electrophoresis
ANO	second electrostatic lens in the electron gun
ara-A	<i>Vidarabine</i>
Bt	biotin
C	cytosine
Cl-ara	<i>Chlofarabine</i>
DEA	dissociative electron attachment
DNA	deoxyribonucleic acid
DSB	double strand break
dsDNA	double stranded DNA
EA	electron affinity
EMS	amperemeter for the filament emission current
ENG	voltage for electron acceleration
EXT	third electrostatic lens in the electron gun
F-ara	<i>Fludarabine</i>
FC	faraday cup
FIL	filament
FWHM	full width at half maximum
G	guanine
HPLC	high-pressure liquid chromatography
LEE	low energy electron
LUMO	lowest unoccupied MO
MO	molecular orbital
nt	nucleotide
PIA	picoamperemeter
QMS	quadrupole mass spectrometer
RNA	ribonucleic acid
SAM	self-assembled monolayer

## IV

SA <sub>v</sub>	streptavidin
SHU	first electrostatic lens in the electron gun
SSB	single strand break
ssDNA	single stranded DNA
T	thymine
T <sub>m</sub>	melting temperature, where 50 % of dsDNA is de-hybridized into ssDNA
TNI	transient negative ion
U	uracil
UHV	ultra-high vacuum
VDE	vertical detachment energy
WEH	wehnelt cylinder, surrounding FIL in the electron gun

## 1. Introduction

Cancer is the second most common cause of death in highly developed countries, only exceeded by heart disease.<sup>1</sup> In 2012, 14.1 million new cancer cases and 8.2 million cancer deaths were recorded.<sup>2</sup> The 5-year survival rate depends strongly on the cancer type, the time of diagnosis and the social structure.<sup>2,3</sup> Therefore, an early diagnosis and precise, improved treatment is very important. Cancer is defined as a group of diseases characterized by uncontrolled and abnormal cell growth and spread.<sup>3</sup> If the spread is not stopped, it can cause death of the patient. The disease can be caused by internal or external reasons. Internal reasons are aging, less effective repair mechanisms, hormones and immune conditions, and inherited genetic mutations. Risks that can be reduced are external reasons, such as unhealthy diets, chemicals, overdosed sunlight and radiation, and certain bacteria and viruses<sup>2,4</sup>

Cancer can be treated with surgery, chemotherapy, radiation therapy or a combination thereof.<sup>5</sup> Hormone therapy and immunotherapy are more recent developments.<sup>6-9</sup> The type of therapy is chosen according to cancer stage, its spreading in the body, the genetic features of the tumor, and the time of diagnosis. Surgery is the classic method to treat cancer.<sup>10</sup> For solid tumors with low operative risk this is still the preferred treatment. For delocalized cancer types or inoperable tumors, other forms of treatment are needed. In the 1960s the US government launched the first national cancer chemotherapy protocol.<sup>10</sup> This led to the discovery of many anticancer drugs, mainly antimetabolites and alkylating agents. Typically, the chemotherapeutic drug is cytotoxic with a competitive uptake of cancer cells and healthy tissue. This results in various side effects, such as hair loss, inflammations and immunosuppression. As an alternative, radiation therapy developed immensely during the 1940s with numerous new therapy attempts.<sup>10</sup> Technical innovations, including the linear electron accelerator, opened up a wide field of application. Depending on cancer type and location, different types of ionizing high-energy radiation are commonly used, such as ionized particles, X-ray,  $\gamma$ -ray and high-energy electron beams. The type of radiation chosen for the therapy depends on the particle penetration depth. Along the high energy radiation track, low-energy electrons (LEEs) with a broad energy distribution and a local maximum around 10 eV are generated.<sup>11</sup> At energies below 15 eV those electrons induce strand breaks in the nuclear DNA by dissociative electron attachment (DEA).<sup>12</sup> If those strand breaks are not repaired by proteins, apoptosis (cell death) occurs.<sup>13</sup> The aim of radiation therapy is to selectively damage only cancer cells. To improve the selectivity, chemotherapy and radiation therapy are combined.<sup>14</sup> Since cancer cells have a faster metabolism, the uptake of radiosensitive

anti-cancer drugs, including modified nucleobases, is higher in that tissue.<sup>15</sup> The precise determination and differentiation of the radiation induced damage and cell toxicity of the chemoradiotherapeutical drug is extremely important to evaluate the efficiency of the therapy. Yet this differentiation is difficult with classic medical studies, since apoptosis can result from both effects, cell toxicity and radiation induced damage.<sup>14,15</sup> Therefore, both aspects have to be analyzed separately.

Medical studies investigate the overall ability of radiosensitizers to cause apoptosis in living cells. On the other hand, experiments with small building blocks of the complete system can reveal very detailed information about the interaction of LEEs with the DNA backbone<sup>16</sup>, the nucleobases<sup>17-20</sup> or typically used radiosensitizers<sup>21</sup>. Yet those experiments carry the risk of misinterpretation, since the molecular and environmental interactions, such as surrounding water, hydrogen bonds, and stacking interactions, are missing. Therefore it is necessary to create a link between both extremes.

The experiments with small building blocks are typically DEA experiments with LEEs, done in the gas phase. Therefore, those experiments are limited by the size of the molecule and its ability to evaporate. Thus, an experiment to study DEA in more complex structures has to be transferred into condensed phase. One approach is the irradiation of thin plasmid films with LEEs and gel electrophoresis to study single and double strand breaks.<sup>12</sup> Yet the penetration depth of LEEs is very low and thus, it is difficult to irradiate the plasmid film homogeneously. Furthermore, this method cannot precisely analyze the detailed interaction of neighboring or modified nucleobases and higher geometrical order in the DNA strand. Irradiation of short, well-defined oligonucleotides instead of plasmid DNA delivers information about strand break locations. The resulting fragments can be analyzed with high-pressure liquid chromatography (HPLC).<sup>22</sup> Those experiments are limited to very short oligonucleotides<sup>23</sup> and still have the problem that thin films are combined with very low penetration depth of LEEs resulting in inhomogeneously irradiated samples. To avoid all these problems, single-molecule approaches using well-defined oligonucleotides of varying length and sub-monolayer coverage are required. With the invention of the DNA origami technique in 2006<sup>24</sup> such desired sub-monolayer films of well-defined oligonucleotides can now be prepared. The experimental approach to use DNA origami triangles with attached single stranded DNA oligonucleotides to study DEA to DNA was first published in 2012 by Keller *et al.*<sup>25</sup>

The theoretical basics of this novel and versatile approach to study LEE-induced DEA in DNA oligonucleotides are discussed in chapter 2 of this work. In the subsequent chapter 3 an experimental setup is developed and optimized to yield highly reproducible and accurate data for the quantification of DNA strand breaks. Based on a sensitive current

detection and variable electron energy from 5 – 10 eV, the absolute strand break cross sections for a variety of different oligonucleotide sequences are determined. Additionally, an optimized sample preparation protocol is developed, since DNA origami triangles turned out to be rather susceptible towards deformation and degradation on silicon surfaces (see chapter 3.4).

Chapter 4 presents an investigation of two radiosensitizers incorporated into DNA oligonucleotides. First, the absolute strand break cross sections of 2-fluoroadenine ( $^2\text{F}A$ ) are determined in dependence of the electron energy. In comparison with the unmodified nucleobase adenine (A),  $^2\text{F}A$  shows a significant enhancement by a factor of 1.7 at 10 eV and 5.5 eV. These experiments are supported by additional fragmentation studies of  $^2\text{F}A$  in a classic DEA gas phase experiment. For comparison, also 5-fluoruracil ( $^5\text{F}U$ ) as a commonly used cytotoxic agent and radiosensitizer is studied. Similar enhancement factors are obtained as for  $^2\text{F}A$  at 10 eV, while at 5.5 eV for  $^5\text{F}U$  no enhancement was observed.

The influence of higher order DNA topologies during irradiation with LEEs is discussed in chapter 5. A well-suited sequence for those studies is the human telomere sequence. In the presence of alkali cations it can fold into rigid G-quadruplexes.<sup>26</sup> As a key sequence at the chromosome end, the telomere sequence can be used as a target for cancer treatment.<sup>27</sup> Therefore, its sensitivity towards LEEs is important to study. This work focusses on the influence of length, nucleobase sequence, and topology on the LEE-induced strand breakage. The absolute strand break cross sections for different telomere derivatives are determined. Comparing those results, a clear increase in sensitivity with telomere length is evident. The polarity of the sequence does not influence the sensitivity, while the scrambled oligonucleotide sequence shows a significant reduction of sensitivity towards 10 eV electrons. In the presence of  $\text{K}^+$  ions the absolute strand break cross section is significantly decreased, thus indicating a stabilization of the oligonucleotide through G-quadruplex formation.

Both aspects, the nucleobases modified with fluorine and the telomere derived sequences, reveal relevant aspects for chemoradiotherapy. Compared to their natural nucleobase derivatives, the F modified nucleobases increase the strand break cross section significantly at 10 eV, the most probable energy of secondary electrons during radiotherapy with high-energy radiation. The telomere derived sequences revealed significant differences between the folded and unfolded state. These telomeres are located at the chromosome ends and are folded and unfolded during different states of the cell reproductive cycle. Therefore, the variations in the strand break cross sections between both states suggest an optimum time for irradiation depending on the cell state.

## 2. Theoretical and experimental basics

### 2.1. Deoxyribonucleic acid (DNA)

DNA was first isolated by Friedrich Miescher in 1869.<sup>28</sup> Almost one century later, in 1953, James Watson and Francis Crick identified the molecular structure of the DNA double helix.<sup>29</sup> It stores the genetic instructions for development, functioning and reproduction of all living organisms.<sup>30</sup> Together with proteins and carbohydrates, these three types of macromolecules are most essential for all known forms of life. The DNA strand is a polymer formed by a large number of nucleotide units.<sup>31</sup> Each nucleotide is a composition of one nitrogen-containing nucleobase, a 2'-deoxyribose monosaccharide sugar, and a phosphate group (Figure 1.a). The sugar and phosphate groups represent identical subunits that form the sugar phosphate backbone by negatively charged phosphodiester bonds between the third and the fifth carbon atoms of the sugar rings adjacent to the central phosphate. These asymmetric bonds create a polarity of the DNA strand, with a terminal phosphate group at the 5' end and a terminal hydroxyl group at the 3' end. There are four different nucleobases, which form a unique sequence along the DNA strand.<sup>31</sup> These nucleobases are the two purine bases adenine (A) and guanine (G), and the two pyrimidine bases cytosine (C) and thymine (T) (Figure 1.a). The non-deoxidized RNA on the other hand contains uracil (U) instead of thymine, which is the non-methylated derivative of T.<sup>31</sup> Through hydrogen bonds, these nucleobases can form complementary A-T or G-C base pairs, hybridizing two DNA strands to form the DNA double helix (Figure 1.b). The double helical structure results from stacking interactions between neighboring base pairs.<sup>31</sup> In the aqueous environment of the cell, the negatively charged DNA backbone is stabilized by cations, usually  $\text{Na}^+$  and  $\text{Mg}^{2+}$ , and a solvation shell. When DNA is dried, it changes its conformation from the natural B type<sup>32</sup> to the A type (Figure 2).<sup>33</sup> Depending on factors such as the degree of hydration, sequence, topology, protein binding, and cation concentration, more conformations are possible.<sup>34</sup> Both DNA strands can be reversibly de-hybridized either by heat, mechanical force or enzyme interactions, which is vital for DNA replication. The temperature at which 50 % of the double stranded DNA (dsDNA) is de-hybridized and exists as two separate single stranded DNA (ssDNA) is defined as the melting temperature ( $T_m$ ).<sup>31</sup> This melting can also occur at low salt concentrations and high pH. The stability of the dsDNA depends on the G-C content, since this base pair stabilizes the double helix with three hydrogen bonds, compared to the two hydrogen bonds in the A-T base pair. Furthermore, the overall

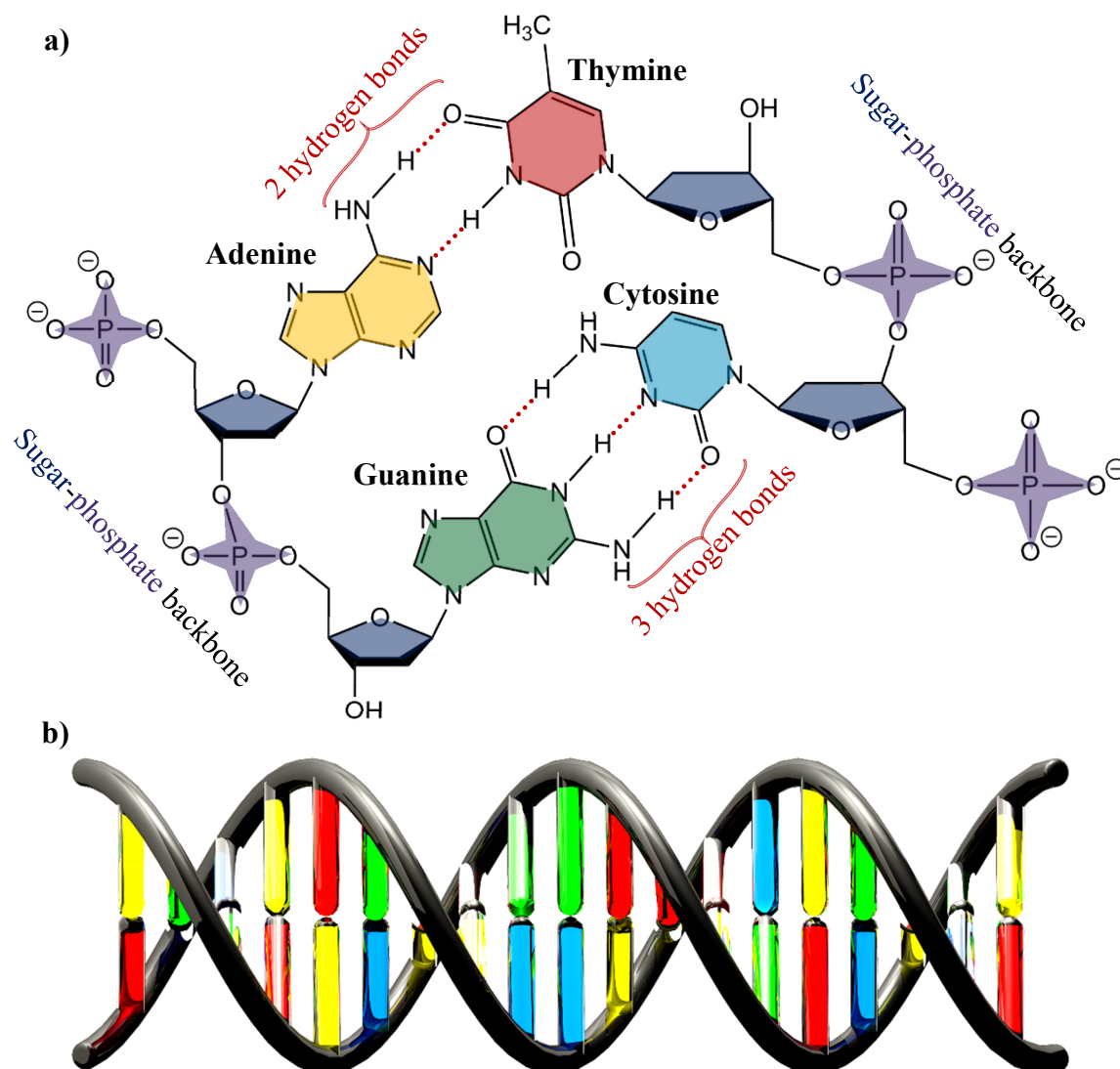


Figure 1. a) Scheme of the DNA double helix, with two nucleobases in each strand. The complementary nucleobase pairs adenine (yellow)-thymine (red) and guanine (green)-cytosine (blue) stabilize the double helix by hydrogen bonds (red dotted lines). The nucleobases are attached to 2'-deoxyribose (dark blue), forming nucleosides. The 5'-C of the sugar is connected to phosphates (purple), forming a nucleotide. Each nucleotide is connected to its neighbor at 3'-C of the sugar, forming the sugar phosphate backbone of the polynucleotide DNA. b) 3D model of the DNA double helix.

length of the double helix influences its melting temperature, with higher  $T_m$  for longer helices.

Each of the two single strands stores the same genetic information. During DNA replication the strands are separated from each other.<sup>35</sup> The sequence of the nucleobases form the genetic code, with three neighboring bases coding one amino acid. The nucleobase sequence that codes an entire protein is called gene.<sup>36</sup> In the eukaryotic cell, the DNA is organized in the chromosomes. Within these structures, chromatin proteins such as histones condense and compact the DNA double helix. At the ends of the chromosomes, ssDNA with a certain sequence called telomere is found, exhibiting a large number of repeating units.<sup>37</sup> The main function of this telomere region is to allow chromosome replication.<sup>38</sup> It furthermore protects the chromosome ends. In human cells, the telomere sequence TTA GGG appears as ssDNA strand with several thousand repeats. It can fold into higher geometric structures with various different patterns (see chapter 2.3).

In medicine, modified nucleosides play a major role in treating cancers and viral diseases, for instance as selective enzyme inhibitors,<sup>39</sup> or as nucleic acid chain terminators, which interrupt DNA replication.<sup>40-43</sup> Furthermore, they can be incorporated into DNA strands. During radiochemotherapy the incorporated modified nucleosides can act as sensitizers, increasing the single and double strand break yield. While single strand breaks (SSBs) can be repaired enzymatically, double strand breaks (DSBs) lead to apoptosis.

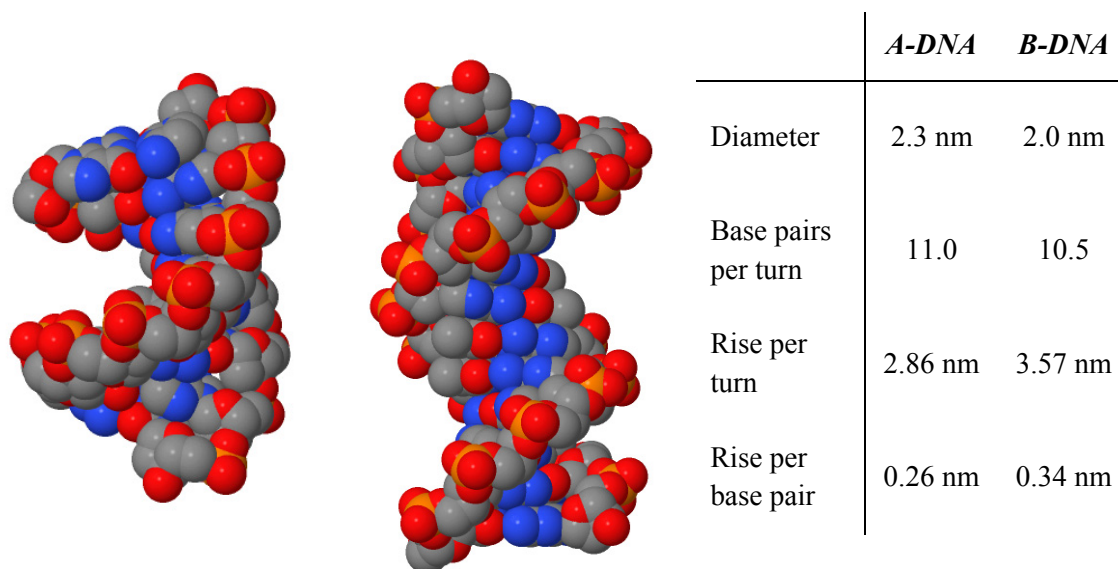
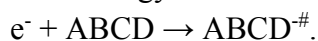


Figure 2. Crystal structures of a dried A-DNA octamer (left)<sup>33</sup> and a hydrated B-DNA dodecamer (right)<sup>32</sup> with a table of geometric properties of both structures.

## 2.2. Dissociative electron attachment (DEA) in DNA

The interaction of high energy radiation with cells does not necessarily lead directly to DNA strand breaks. The primary effect of this radiation is the ionization and dissociation of the water molecules inside the cell. Along the radiation track, collisions between the high energy radiation and water molecules occur. The subsequent ionization of water molecules generates a broad distribution of low-energy electrons (LEEs) with a most probable energy around 10 eV.<sup>44</sup> These secondary electrons are generated with an estimated quantity of  $\approx 4 \cdot 10^4$  electrons per MeV primary quantum deposited.<sup>45</sup> They are able to directly induce DNA single and double strand breaks *via* DEA) through negative ion resonances.<sup>12,46,47</sup> In DEA, a transient negative ion (TNI) is formed, which decays by dissociation. The generated short living TNI can be formed and localized in the various DNA components and lead to bond cleavage.<sup>48</sup> Those TNI are generated by resonant transitions from the neutral to an anionic state at specific energies below its ionization threshold. The decay of this TNI occurs *via* competitive processes. Either the extra electron is re-ejected, leading to the initial molecule (resonant elastic scattering), or the molecule will be vibrationally excited (resonant vibrational excitation). Additionally, the dissociation of the TNI yielding a relatively stable anion and one or more fragments can occur.

The first step of DEA is the formation of the TNI through the Franck Condon transition, which is a vertical transition from the electronic ground state of the neutral molecule to the potential energy surface of the anion



“#” signifies the transient anionic state.<sup>48</sup> The necessary excitation energy  $E$  is the incident energy of the attached electron and thus corresponds to the electron affinity of the molecule.<sup>48</sup> In case the molecule has a positive electron affinity, the ground state of the anion is energetically lower than the associated neutral precursor state. The interaction between the incoming electron and the target molecule is at large distances dominated by the attractive charge-induced dipole potential, while at short distances the repulsive centrifugal potential from the angular momentum of the electron takes over. In result, the interaction can be described by the sum of both potentials. If the angular momentum of the electron is  $\neq 0$ , the electron could be trapped temporarily in the potential. Since this resonance depends on the centrifugal barrier and thus on the shape of the interaction potential, it is called shape resonance.<sup>49,50</sup> In case the electron occupies a molecular orbital (MO), which was previously empty and the electron configuration of the molecule is otherwise unchanged, it is furthermore called single particle shape resonance.<sup>48</sup> The TNI formed by this resonance is only vibrationally excited. Figure 3 shows the neutral

molecule ABCD and a single particle shape resonance, where the electron with the vertical attachment energy (VAE) is captured into the lowest unoccupied MO (LUMO) or a higher orbital, forming the TNI.<sup>48</sup> The excited ion can lose the additional electron by autodetachment (AD). As a competitive process, DEA can occur, forming an anion fragment. The energetic difference between the ground state of the neutral molecule and the ground state of the formed anion corresponds to the adiabatic electron affinity (EA). The anionic ground state can be reached by solvation, thus in gas phase this stabilized state cannot be generated. The single particle shape resonance usually occurs below 4 eV with short lifetimes in the range from  $10^{-15}$  to  $10^{-10}$  s.<sup>49,50</sup> However, the lifetime can be extended through internal energy redistribution.<sup>48</sup>

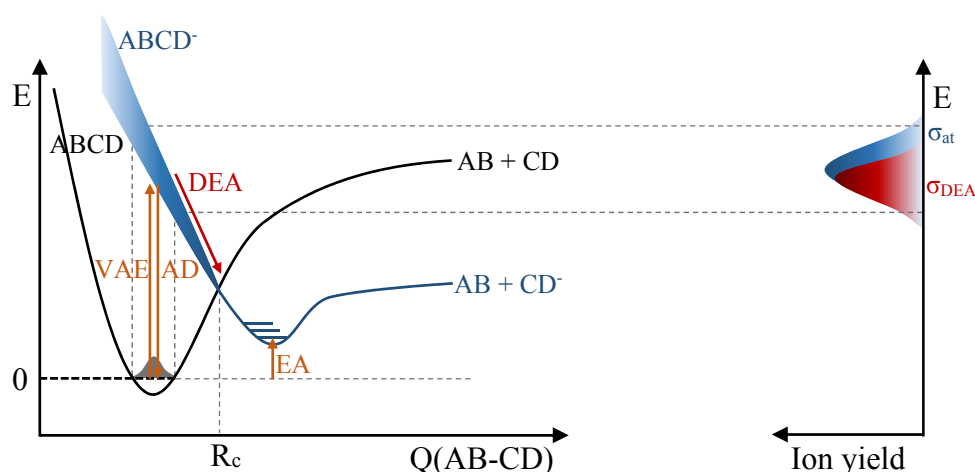


Figure 3. Simplified two-dimensional potential energy diagram for the formation of a transient negative ion (TNI) in the molecule ABCD. An electron attaches to ABCD with the vertical attachment energy (VAE). The TNI can relax by auto detachment (AD) of the electron, or competitively by dissociative electron attachment (DEA), until the crossing point  $R_c$  is reached. The energy difference between the ground states of ABCD and  $ABCD^-$  corresponds to the electron affinity of the neutral molecule ABCD. The ion yield shown on the right side reflects the initial Franck-Condon transition with the cross sections of the electron attachment  $\sigma_{at}$  and DEA process  $\sigma_{DEA}$ .

For a higher electron energy, electronic excitation can occur where two electrons occupy a formerly empty MO.<sup>48</sup> These electronically excited resonances are called core excited or two particles-one hole (2p-1h) resonances. In addition, if the TNI is energetically above the corresponding electronically excited neutral molecule, the electron is bound by the centrifugal barrier in the potential. Due to its similarity to a shape resonance, this state is referred to as core excited shape resonance.<sup>48</sup> In case the TNI is energetically below the corresponding electronically excited neutral molecule, it cannot relax by ejection of the electron. In result, this TNI can relax only into lower excited states through a two electron transition by rearrangement of the electronic structure, extending the lifetime compared to the shape resonance. These resonances are referred to as core excited Feshbach resonances.<sup>48</sup> In addition, Feshbach resonances will be formed at low energies, if the vibrationally excited TNIs are below the corresponding state of the neutral molecule.<sup>51</sup> These vibrational Feshbach resonances (VFRs) appear at energies close to 0 eV for excitations close to the ground state of the neutral molecule or for complex structures where the intramolecular energy redistribution delays the re-ejection of the electron. Furthermore it can be observed from dipole-bound states, where highly polarizable molecules bind the electron in a diffuse Rydberg-type orbital.<sup>48</sup> In gas phase DEA experiments, the measured ion yield at a certain energy corresponds to the appearance energy of the resonance (Figure 3).

The cross section of the DEA process  $\sigma_{\text{DEA}}$  corresponds to the product of the electron attachment cross section  $\sigma_{\text{at}}$  and the dissociation probability, thus the probability of the TNI to reach the crossing point  $R_c$  of the potential energy curves of the neutral molecule and the TNI before the electron is re-ejected.<sup>48</sup> In general, the cross section in physics defines an area of interaction for certain dynamic processes, such as the particle scattering experiments of Rutherford<sup>52</sup> and Hofstadter.<sup>53</sup> The scattering of particles can be either elastic or inelastic. In addition to scattering, resonances can influence the cross section of the particle-particle interaction. This process depends on the particles. For example, a photon can excite a molecule only in case the photon energy corresponds to the energy of the transition, i.e. it is resonant, while an electron can excite a molecule in case the kinetic energy is higher than the threshold of excitation.<sup>54</sup> In this work, the cross section between LEEs and oligonucleotides leading to single strand breaks are studied and referred to as absolute strand break cross sections.

### 2.3. The telomere sequence in DNA

The telomere is a non-coding, G-rich tandem sequence, with the 5'-d(TTAGGG) repeating unit in vertebrates.<sup>55</sup> It is a nucleoprotein complex located at eukaryotic chromosome ends<sup>56</sup> and in some promoter regions of several proto-oncogenes including *c-myc*, *c-kit* and *k-ras*.<sup>57</sup> The telomere maintains the integrity of the genome and protects the chromosomes from recombination, exonuclease degradation, and end-to-end fusion.<sup>37</sup> The estimated amount of repeated telomere sequence is up to 10 kb in humans.<sup>58,59</sup> The replication circle erodes the telomere ends, thus the sequence shortens by 50 - 100 bases per copy.<sup>60</sup> In consequence, the sequence will finally be too short for replication, leading to apoptosis of the cell. This process can be reversed by the transcriptase ribonucleoprotein telomerase, which repairs and elongates the telomere sequence.<sup>61</sup> In contrast to the healthy tissue, cancer cells have a high telomerase activity, thus the telomere sequence gets extended, allowing an unlimited DNA replication.<sup>62</sup> Thus, the telomere sequence is a potential therapeutic target in oncology.<sup>27,63</sup>

Due to the G-rich sequence, four telomere repeating units can fold into a G-quadruplex in the presence of monovalent cations *via* Hoogsteen base pairing (Figure 4).<sup>64</sup> The structures of G-quadruplexes and their intermediates were intensively studied,<sup>38,65-67</sup> e.g. by high-speed atom force microscopy (AFM).<sup>68-70</sup> The G-quadruplex can be formed intramolecularly with one strand, or intermolecularly with two or more different strands. The pattern of the backbone depends on the strand orientations (Figure 5), resulting in parallel or anti-parallel G-quadruplexes. Both can occur *via* intra- and intermolecular folding. Furthermore, the folding pattern depends on the loop regions between the G repeat units, and particularly their sequence and length. Most important is, however, the nature of the central monovalent alkali metal ion, which coordinates with the 6-O guanine atoms in a G-tetrad (Figure 4). Different ions result in different conformations. For instance, the human telomere sequence 5'-d(TTA GGG) is folded into a propeller type G-quadruplex with a fully parallel strand pattern with external loops by  $K^+$  (Figure 6.a), while  $Na^+$  is known to fold into a basket type G-quadruplex with two parallel and two antiparallel strands exhibiting an ab/ba pattern with lateral loops (Figure 6.b).<sup>69,71,65</sup>

To understand the folding mechanism, intermediates were experimentally detected and analyzed with high-speed AFM and the DNA origami technique in 2014.<sup>70</sup> Here, a DNA origami frame controls the structure and stoichiometry of telomere sequences, thus the intermediates can be formed and analyzed in real-time. Within the presence of  $K^+$  and  $Mg^{2+}$ , the human telomere sequence proofed to fold into two intermediates, the G-hairpin and G-triplex. The authors concluded, that  $Mg^{2+}$  stabilizes the G-hairpin, while in the G-triplex both cations interact competitively and the Hoogsteen G-quadruplex is

predominantly folded by  $K^+$ . In cell plasma, both ions are most abundant. Thus, this process may be biologically relevant.<sup>70</sup>

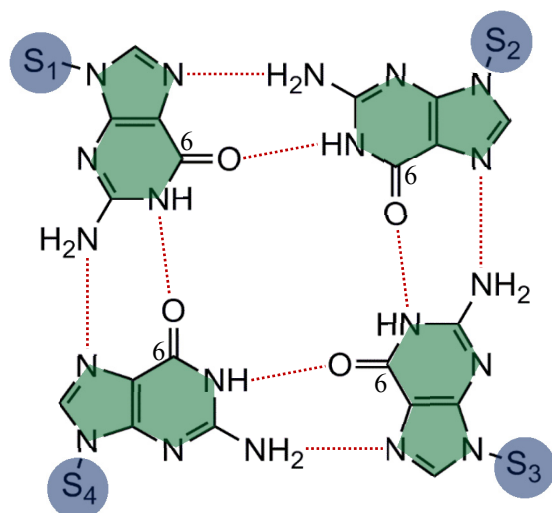


Figure 4. Hoogsteen base pairing (red dotted line) of four G nucleobases (green) attached to sugars S1 - S4, forming one tetrad of the G-quadruplex.

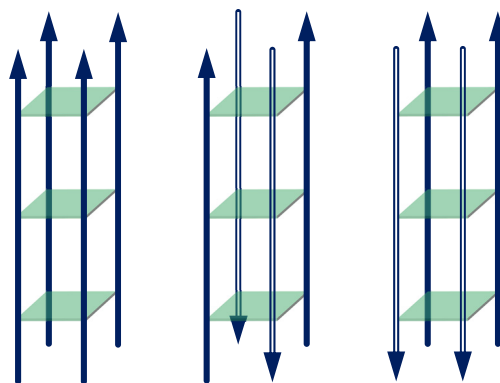


Figure 5. Schematic drawing of the backbone polarity (blue) in the G-quadruplex (green) folding pattern, showing the folding of 4 parallel strands (left). 2 parallel and 2 antiparallel strands in ab/ba (center) and aa/bb (right) type, folding either inter- or intramolecularly.

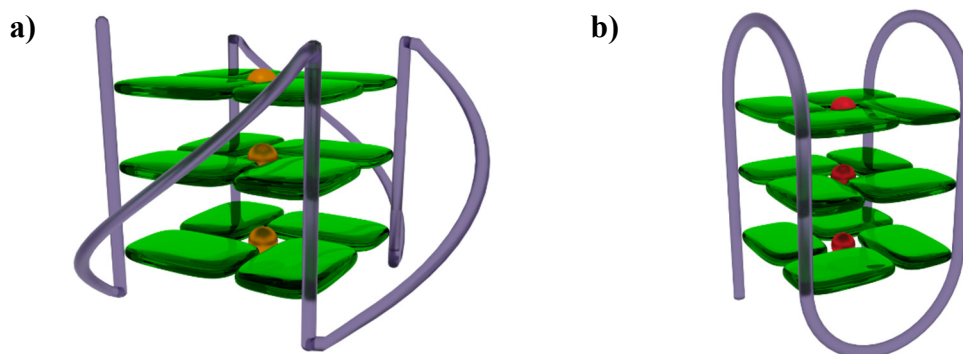


Figure 6. Folding of the human telomere sequence with a)  $K^+$  into a propeller type, and b)  $Na^+$  into a basket type G-quadruplex.

The unique electronic properties of the telomere sequence were previously studied by photoelectron transmission through self-assembled monolayers.<sup>72</sup> The authors found a special affinity to electrons, caused by the high clustering level of G with an additional neighboring A. They assumed furthermore that the increased electron affinity of the telomere sequence helps protecting the coding DNA sequences from electron damage by directing the electron damage into the telomere non-coding sequence at the end of the chromosomes.<sup>72</sup> These studies did not consider the actual DNA damage in the form of strand breaks and the influence of folded G-quadruplex structures in the telomere sequence. Thus, the influence of the telomere sequence and topology on electron induced strand breakage was up to now unknown, but is studied in detail within the present work.

## 2.4. Radiosensitizers for cancer therapy

Several antiviral, chemotherapeutic, and radiochemotherapeutic drugs directly interact with and modify DNA in the cell. The most important ones are cis-platin (Figure 7.a),<sup>73-76</sup> which induces structural distortions upon binding, and chemically modified nucleoside analogues, which are directly incorporated into the DNA structure.<sup>15,77-81</sup> Among the latter, fluoronucleosides have gained tremendous importance in clinical practice and research.<sup>82-84</sup>

In the form of phosphates, modified nucleosides can be incorporated into the DNA sequence. Since cancer cells have a higher nutrient uptake due to their enhanced metabolism, those cells tend to accumulate the drug. As long as the modified nucleoside does not inhibit enzyme activity during the cell metabolism, they are only marginally cytotoxic. The fluorine substitution even increases the metabolic stability.<sup>85-87</sup> Attached to the 2'- or 3'-position of the sugar, F increases the chemical stability of the nucleoside analogue, especially in an acidic environment.<sup>88</sup> The drug mimics uptake and metabolism of natural nucleosides, but finally induces apoptosis.<sup>89</sup>

The influence of F in biologically active molecules is based on the following characteristics.<sup>90</sup> First, it mimics hydrogen, since it is the second smallest atom. Therefore no significant geometrical distortions are induced by F substitutions. Second, F is the most electronegative atom. Thus, electron density is drawn away from the neighboring carbon atom. Third, F is isopolar and isosteric with OH, therefore it mimics the hydroxygroup (C-F bond 1.35 Å, C-O bond 1.43 Å). Forth, F is a hydrogen bond acceptor, and fifth, the C-F bond is much stronger than the C-H bond, which leads to higher biological and chemical stability. In result, F changes biological activities drastically and is thus frequently used in medicine in the form of fluorinated drugs.

The first F modified nucleobase was 5-fluoropyrimidine, which was first synthesized in 1957.<sup>91</sup> In 2006, a review of fluorinated nucleosides as anti-cancer drugs mentioned the chemotherapeutical drug *Fludarabine* (F-ara) as one of the most important fluorinated anti-cancer drugs (Figure 7.d).<sup>92</sup> A derivative of F-ara without the F modification at the nucleobase is the anti-viral drug *Vidarabine* (ara-A) (Figure 7.c). The only difference to the natural DNA is the arabinose sugar instead of deoxyribose. It is one of the most important nucleoside antibiotics due to its high toxicity to mammalian cells. Furthermore, ara-A inhibits the growth of many bacteria and DNA viruses.<sup>93,94</sup> In result, it is used mainly for herpes encephalitis in humans. While ara-A is not resistant to deamination by adenosine deaminase, F-ara phosphate is. Furthermore, F-ara is water-soluble. The prodrug is rapidly dephosphorylated, transported into the cell, and rephosphorylated by deoxycytidine kinase, to the triphosphate.<sup>90</sup> This molecule inhibits DNA synthesis by

inhibiting DNA polymerase, ribonucleotide reductase, DNA primase and DNA ligase.<sup>90</sup> It prevents DNA extension through direct incorporation into DNA.<sup>90</sup> F-ara was modified to the new drug *Clofarabine* (Cl-ara).<sup>95,96</sup> Cl-ara showed stronger enzyme inhibition,<sup>97</sup> with longer intracellular retention in acute myeloid leukemia. In combination with irradiation both Cl-ara and F-ara showed potential to be used as a drug in chemoradiation therapy.<sup>98,99</sup> Another classic anti-cancer drug is *Fluorouracil* (<sup>5</sup>FU) (Figure 7.b), used in chemotherapy and radiochemotherapy for over 60 years.<sup>100</sup> It is listed on the World Health Organization list of essential medicines.<sup>101</sup> <sup>5</sup>FU inhibits the thymidine synthase, and stops the 5'-C-methylation for the conversion of 2'-deoxyuracil-monophosphate to 2'-deoxythymine-monophosphate.<sup>84</sup> Thus, the sensitizing effect of <sup>5</sup>FU results from DNA synthesis inhibition and accumulation of cells in the early S phase of the cell cycle. In addition, <sup>5</sup>FU slows down the repair of DSBs, thus enhancing the rate of cell death through radiation.<sup>84</sup> A modern F containing anti-cancer drug of clinical importance is *Gemcitabine* (<sup>d</sup>FdC; 2',2'-difluorodeoxycytidine) (Figure 7.e) with broad spectrum in cancer therapy. In this drug, F is located at the sugar instead of the nucleobase. <sup>d</sup>FdC inhibits DNA reproduction by competitive incorporation into the growing DNA<sup>102</sup> and it is used as a combined radiosensitizer and cell toxic agent.<sup>103,104</sup> The modification of the nucleoside is not limited to F. Especially halo-uracils were studied in detail with regard to their medical potential<sup>84</sup> as well as their fragmentation behavior when irradiated with LEEs.<sup>79</sup> In addition to the obtained different fragmentation behavior of the modified nucleobases compared to the unmodified ones, a nucleotide sequence dependency of bromo- and iodo-uracil was found when incorporated into the DNA single strand.<sup>105,106</sup>

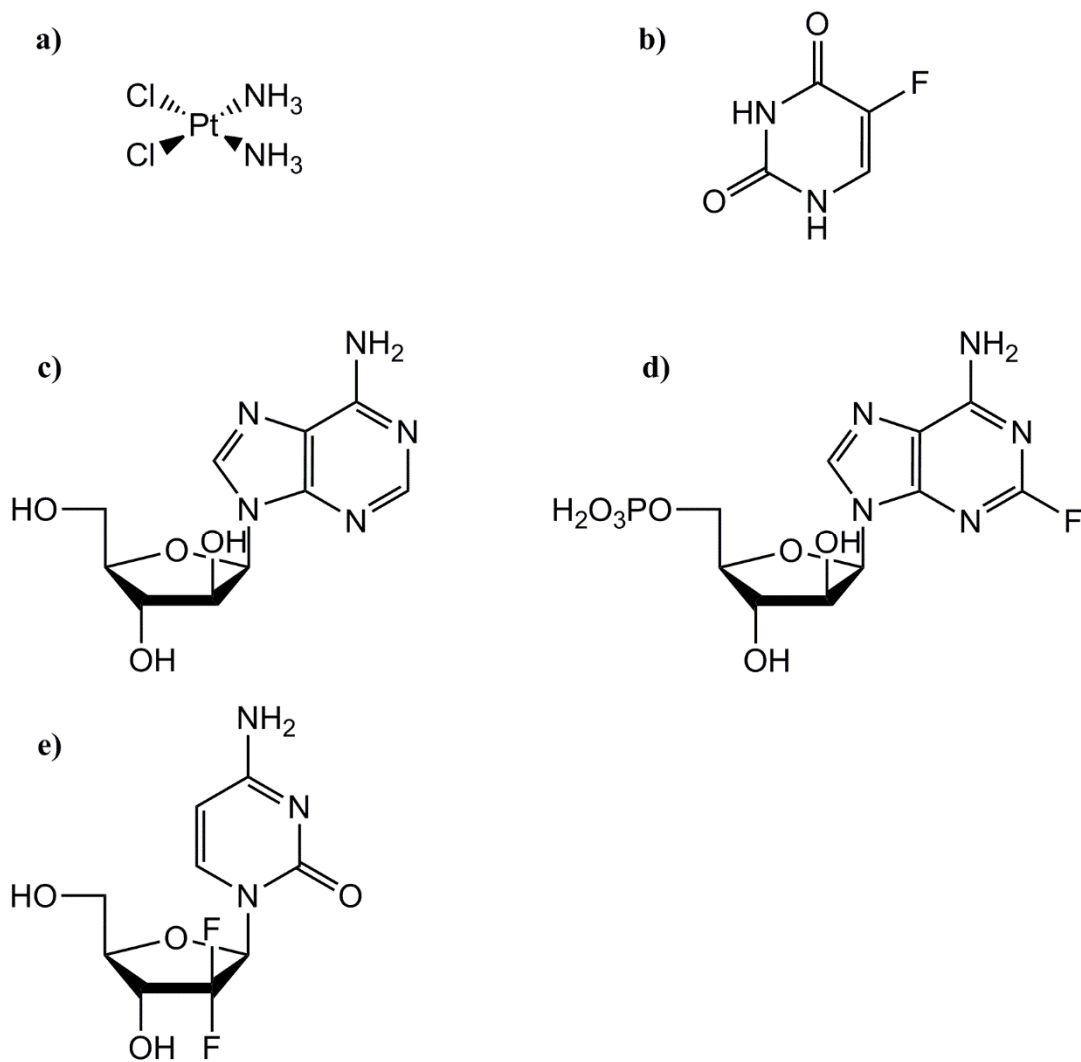


Figure 7. Chemical structures of a) cis-platin, b) 5-fluorouracil ( $^5\text{FU}$ ), c) Vidarabine (ara-A), d) Fludarabine (F-ara), and e) Gemcitabine ( $^d\text{FdC}$ ).

## **2.5. Established experiments to study LEE-induced fragmentation in DNA**

In the cell, DNA is packed with proteins, forming a chromosome. Surrounded by water and various ions, the DNA double helix inside the chromosome is mainly formed by hydrogen bonds between the nucleobases of two strands and stacking interactions between neighboring nucleobases. In result, the highly complex system can be studied experimentally with model systems of reduced complexity. However, the results obtained with the simplified model systems are not necessarily representative for these complex systems. Medical and biological studies analyze the influence of radiosensitizing drugs on cells exposed to high energy irradiation with determination of cell death rates and tumor cell development.<sup>104</sup> The molecular mechanisms leading to cell death, however, are rather difficult to analyze within those experiments.

Due to the low penetration depth of LEEs, physico-chemical experiments using condensed DNA films are hindered by the small amounts of irradiated material. Therefore highly sensitive methods are needed to quantify LEE-induced strand break damage. In previous studies supercoiled plasmid DNA with several thousand base pairs was irradiated with LEEs.<sup>12,46</sup> The DNA strand breaks were mostly quantified with agarose gel electrophoresis (AGE). These LEEs induce SSBs and DSBs, changing the conformation from supercoiled to cyclic for SSB or linear for DSB. Even very small amounts of damaged material can be separated due to the different DNA conformations by AGE. This method, however, does not yield any specific information about sequence dependency or topologic influences in the DNA.

A method to analyze sequence-specific strand breaks is the high-performance liquid chromatography (HPLC).<sup>23</sup> Due to the increasing amount of different fragmentation products in longer sequences, only short oligonucleotides up to tetramers can be analyzed. With longer nucleotides, the amount of each generated fragment lies below the detection limit of HPLC. To overcome the problem of sensitivity limitations, highly sensitive techniques need to be applied. Fluorescence spectroscopy of DNA self-assembled monolayers (SAMs) with oligonucleotides of well-defined sequence was used to quantify DNA damage in single strands.<sup>107,108</sup> However, this method does not yield information about topologic influences either and it is limited to single stranded DNA. Oligonucleotides can be furthermore analyzed with photoelectron transmission, yielding sequence specific electronic properties,<sup>72</sup> yet the strand break yield is not accessible.

For small molecules on the other hand, detailed studies of the fragmentation behavior are available.<sup>47,48</sup> Isolated building blocks of the DNA can be transported into the gas phase, where a crossed monochromatic electron beam irradiates the target molecule. Below the

ionization potential, structure specific DEA resonances can occur (see chapter 2.2), generating charged fragments which can be analyzed with a mass spectrometer. The intensity of the fragments can thus be detected as a function of electron energy. Although mass spectrometry provides detailed information about fragmentation pathways of the target molecule, quantification of DNA strand breaks is extremely challenging. Furthermore, sequence dependence and topological influences are difficult to be analyzed with this method either. Between the small DNA building blocks which yield detailed information about fragmentation pathways and the complex DNA structures of greater biological importance such as plasmids, an information gap appears (Figure 8). The plasmid analyses lack the possibility to investigate sequence-dependent effects. HPLC studies, however, are limited to short sequences.<sup>23</sup> The DEA studies with mass spectrometry on the other hand are limited by the necessity to transport molecules into the gas phase. To overcome this problem, irradiation has to be performed in the condensed phase with well-defined oligonucleotides of certain length and sequence. A novel approach combining both aspects was first published in 2012.<sup>25</sup> The aim of the present work is to establish and further improve this approach, which is based on the AFM analysis of oligonucleotide targets attached to DNA nanostructures.

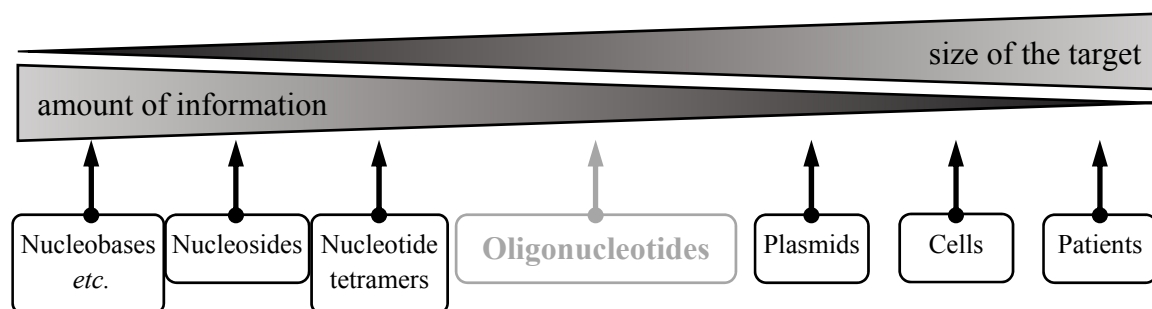


Figure 8. Illustration of the qualitative correlation between the size of the studied target and the amount of information extracted from one experiment. From left to right the size of the target increases, from DNA building blocks, such as the nucleobases, sugar or the phosphate group, to nucleosides, and nucleotide trimers. So far, the oligonucleotides are studied in microarrays on gold surfaces. With decreasing amount of information, plasmids can be studied towards LEE interaction. Finally, clinical studies with animals and human patients can deliver information about survival rates and drug influences, while fragmentation mechanisms and influences of structural order in the DNA are inaccessible.

## 2.6. Experimental methods

### 2.6.1. DEA in the gas phase

In the experimental setup used for this work, the anions were extracted by a weak electric field ( $< 1$  V/cm) and analyzed by a quadrupole mass spectrometer (QMS). In general, the QMS consists of four parallel positioned, cylindrical rods. Based on the mass/charge ( $m/z$ ) ratio of the charged fragment, the QMS is filtering the ions. They are separated by an oscillating electric field, which is applied to the rods. In dependence of the stability of their trajectories, the ions are forced onto a circular path through the quadrupole. Within the experimental setup for gas phase DEA experiments, the QMS can be switched between two modes. The first mode is the one usually used for mass spectrometry. At one defined energy all generated anion fragments were detected with the QMS. This option is used for gaining an overview of possible fragments generated at various energies. Additional to this mode, the  $m/z$  ratio of one certain anion can be chosen. In this second mode, the energy of the electrons is varied, resulting in an energy dependence of the anion formation. This mode is used for analysis of the energy dependent fragmentation and to determine the DEA resonances within the entire molecule (see chapter 2.2).

### 2.6.2. DEA in the condensed phase

This work presents an approach to study LEE-induced bond dissociation in well-defined oligonucleotides on a quantitative, single-molecule level. The method is based on detailed AFM analysis of well-defined oligonucleotides precisely localized on discrete template structures. The target sequences are attached to DNA origami templates and rendered visible *via* protein labelling. Due to the discrete templates, the SSBs can be analyzed quantitatively.

**The DNA origami technique** was developed by Rothmund in 2006.<sup>24</sup> It is a nanomanufacturing technique that uses a long single stranded DNA scaffold and folds it by hybridization with specially designed short staple strands into a certain geometric pattern. The number of possible shapes is nearly unlimited, from the two dimensional rectangle and triangle,<sup>24</sup> up to three dimensional objects, such as the cubic box.<sup>109,110</sup> While 3D DNA origami are so far discussed in literature mainly as drug carriers for medical applications,<sup>111,112</sup> 2D origami are used as versatile tools for analytical applications, *e.g.* as templates for single-molecule studies,<sup>113</sup> since they can be decorated with enzymes,<sup>114</sup> nanoparticles,<sup>115</sup> fluorescent dyes<sup>116</sup> and other functional entities with nanometer accuracy.

One of the structurally most stable 2D DNA origami shapes is the Rothemund triangle,<sup>24</sup> consisting of three trapezoids that are attached to each other at the corners. It is quite rigid, which results in well-defined spatial separations of attached entities.<sup>117</sup> Furthermore, the triangles do not tend to aggregate and adsorb as flat and dispersed monomers on surfaces.

Like most DNA origami, the triangle is assembled from the m13mp18 scaffold strand, which is a single stranded viral DNA containing 7249 nucleotides (nt) (Figure 9). 208 specially designed oligonucleotides with an average length of 32 nucleotides act as staple strands, folding the scaffold strand into the desired shape.<sup>24</sup> Each staple strand has a unique position, defined by its sequence and the opposing sequence in the scaffold strand. By Watson-Crick base pairing,<sup>29</sup> a DNA double helix structure is formed. Each staple strand is attached to several different positions on the scaffold strand, forming double helices connected by backbone crossovers. The shape and stability of the resulting DNA origami depends on the length, position, and sequence of the staple strands. The annealing of both, the scaffold and the staple strands, is done by rapidly heating the mixture above the melting temperature and slowly cooling down to room temperature. The thermodynamically driven process of annealing ensures that each staple strand assumes its correct location along the scaffold strand. During cooling, a staple strand which is attached only by few nucleobases to the scaffold is displaced by a staple strand with a more adequate nucleobase sequence. Thus, if a staple strand is extended at one end by a nucleobase sequence with no complementary sequence on the scaffold strand, this extension will protrude from the DNA origami. Since each staple strand has a fixed position in the pattern, the protruding strand will have this position as well. Thus, an oligonucleotide of well-defined sequence can be implemented in the DNA origami triangle at a certain position and can be identified afterwards by reference to this position.

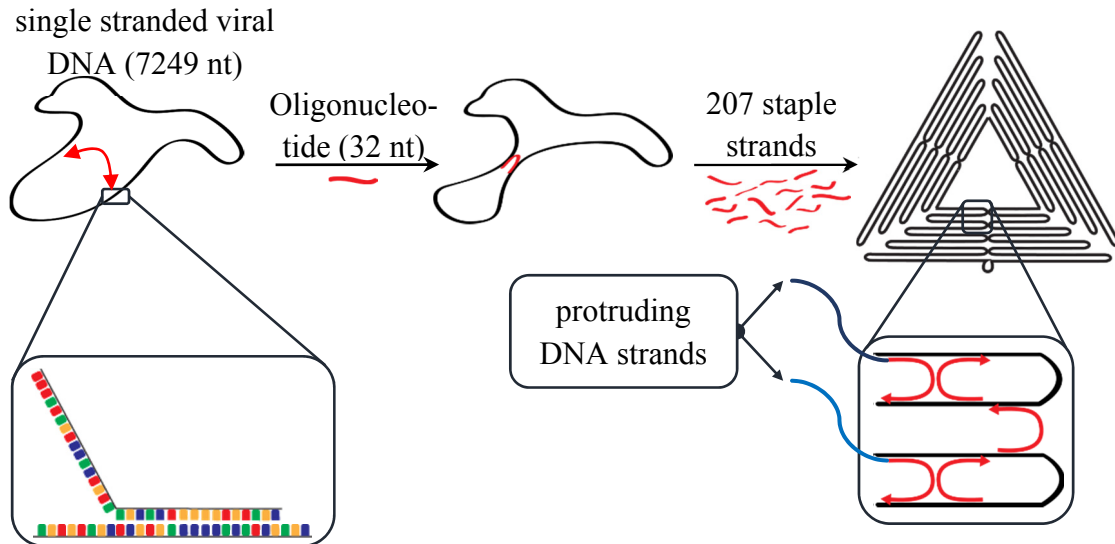


Figure 9. Schematic drawing of the DNA origami assembly process.

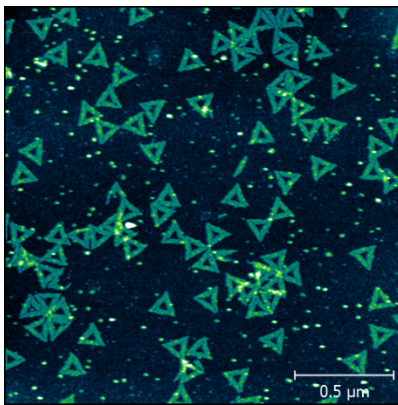


Figure 10. AFM image of DNA origami with triangular shape, immobilized on silicon (height scale: -0.5 to 2.0 μm).

This identification can be done by **AFM** (Figure 10).<sup>69,113,118</sup> AFM is an ideal method for DNA origami analysis, since only a very small amount of material immobilized with sub-monolayer coverage is necessary. With few-nanometer resolution, AFM can image surface structures well below the optical diffraction limit.<sup>119</sup> The information is gained by mechanical interaction between a probe and the sample surface. The probe consists of a cantilever with a sharp tip at its end, which is moved over the sample by piezoelectric elements, scanning the surface with high lateral precision.<sup>120</sup> The cantilever is typically made from silicon and carries a sharp pyramid tip with an apex radius below 10 nm. Additionally, coated cantilevers are available, as well as ultra-sharp tips

with a radius  $\sim 1$  nm. In any case, when the tip is brought into proximity of the sample, forces between the surface molecules and the tip first attract the tip to the sample, until this attraction is overcome by repulsive forces.<sup>121</sup> This results in a macroscopic bending

of the cantilever, which can be detected and plotted as force measurement (Figure 11.a). Usually the bending is measured with a laser beam that is reflected from the backside of the cantilever. The degree of deformation is compared to the setpoint value and the tip height is modified accordingly (feedback loop). The applied voltage on the piezo to modify the height value is detected as a measurement point. By scanning the surface with many points of measurement, an image of the surface topology is calculated. The scanning can be done in numerous operation modes, usually separated in static and dynamic modes. The first one is also called contact mode, indicating the basic principle of measurement. The tip is positioned in the range of the Pauli repulsion and held in this position during the entire scanning process. Therefore, the tip height is changed according to the detected height change of the surface (Figure 11.b). The dynamic mode is also called tapping mode, as well indicating the behavior of the tip during the scanning process. Here, the cantilever is oscillating near its resonance frequency while scanning over the surface. When the height of the sample increases, the amplitude of the resonance frequency is decreased. Depending on the stiffness and electrostatic properties of the surface, the response of the induced resonance frequency can be shifted, detectable as phase shift between the inducing oscillation of the piezo element and the detected oscillation of the cantilever. As long as the height increase or decrease of the surface is rather small, the vertical position of the cantilever is unchanged (Figure 11.c).

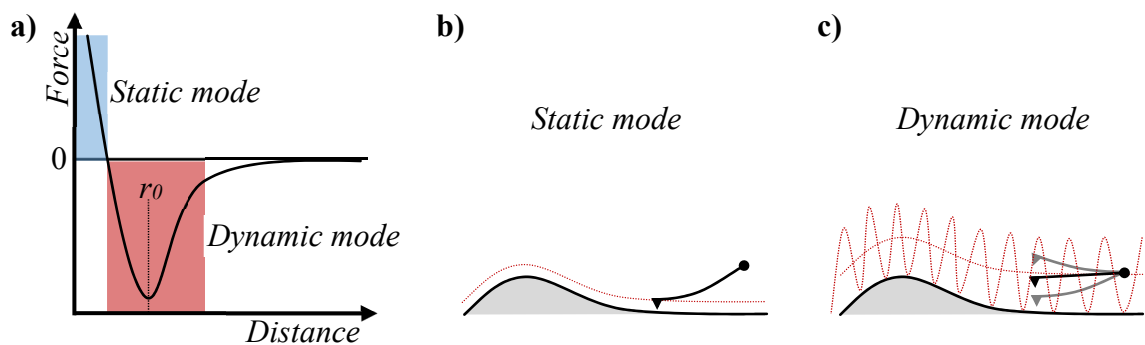


Figure 11. Schematic drawing of a) a force-distance curve, b) a cantilever tip scanning the surface in static mode, and c) a cantilever tip scanning the surface in dynamic mode.

From the AFM images of different samples irradiated at different fluences, the absolute strand break cross section of a certain sequence is directly obtained and can be correlated with the electron energy. To visualize strand breaks, a label is necessary. Previous studies used the combination of biotin (Bt) and streptavidin (SAv) for labelling intact oligonucleotides protruding from the DNA origami.<sup>25,105,113,122</sup> Bt, also known as vitamin B<sub>7</sub>, is essential for the metabolism. It has an exceptionally high binding affinity to the protein SAv, with a dissociation constant of the order of  $10^{-4}$  to  $10^{-5}$  mol/L.<sup>123</sup> Since the Bt-SAv binding is among the strongest known non-covalent interactions, it is used in numerous applications in nanotechnology.<sup>124–126</sup> Due to the possible attachment to nucleotides it is increasingly used for single molecule studies on DNA origami templates by AFM.<sup>25,127,128</sup> The stability of Bt during irradiation with 18 eV electrons was studied before.<sup>129</sup> In the present work, the stability was analyzed at 10 eV. The SAv is bound to the remaining intact strands with Bt after irradiation. Thus, SAv is not irradiated with LEEs.

Figure 12 illustrates the basic idea of the experiments done in this work. Especially two main aspects will be discussed in the following chapters – the energy and sequence dependent dissociation of the oligonucleotide backbone and the influence of DNA topology. A sequence dependency was found in previous experiments with DNA origami irradiated at 18 eV by Keller *et al.*<sup>105</sup> Furthermore, a strong influence of the amount of G in the oligonucleotide was discussed in various experiments.<sup>72,108,130</sup> The topology of oligonucleotides on the other hand, was already studied with AFM and DNA origami by Rajendran *et al.*,<sup>69</sup> within the human telomere sequence. Since this is a well-studied and biologically relevant sequence,<sup>37,38,58</sup> the topology studies in this work are based on this sequence, exploring many topology influencing aspects. Especially the influence of K<sup>+</sup> towards the telomere sequence will be discussed. Since the K<sup>+</sup> association constant on DNA origami/telomeres was calculated to be  $2.6 \cdot 10^4 \text{ M}^{-2}$ , compared to the one of K<sup>+</sup> with free telomeres of  $1.5 \cdot 10^4 \text{ M}^{-2}$ ,<sup>131</sup> the folding process is expected to be largely unaffected by the DNA origami.

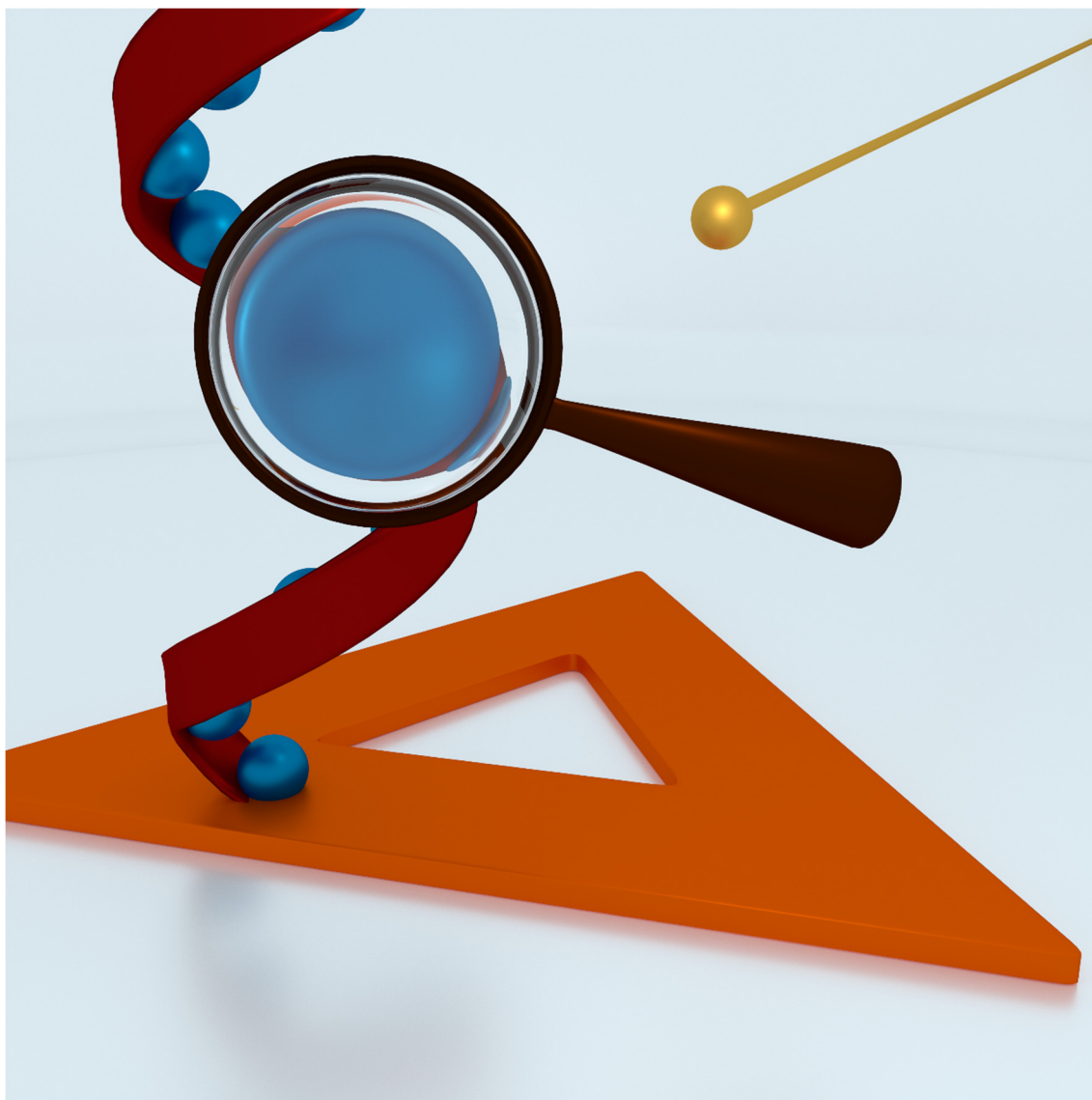


Figure 12. Illustration of the main aspects of this work. An oligonucleotide with well-defined sequence (red backbone with blue nucleobases) protrudes from a triangular DNA origami (orange triangle). The strand is irradiated with LEE (golden ball) and analyzed by AFM. The energy dependent correlation of the nucleobase influence on the fragmentation behavior is studied and discussed based on the absolute strand break cross sections.

### 3. Development of a novel experimental approach for condensed phase DEA studies

#### 3.1. A vacuum chamber for irradiation

##### 3.1.1. The chamber assembly

LEEs of well-defined energy can only be generated in a high vacuum surrounding. A DN100 six-way cross with CF flanges and copper sealings is the central element of the vacuum chamber (Figure 13.f, red). The total volume to be evacuated has to be as small as possible to reduce evacuation time. The current setup takes 4 hours to reach a pressure of  $1.0 \cdot 10^{-7}$  mbar. The vacuum is generated by a turbomolecular pump (*Agilent TwissTorr 304 FS*), which reaches a minimum pressure of  $1.0 \cdot 10^{-8}$  mbar within 24 hours (Figure 13.f, dark blue). Inside the pump, the gas molecules hit a rapidly spinning set of rotor fans at the inlet, given them a momentum towards the exhaust (Figure 13.b). The repeated collisions with the moving solid surfaces creates a vacuum at the inlet. At atmospheric pressure, air behaves according to the laws of fluid dynamics. Thus, particle-particle interactions dominate over particle-surface interaction at atmospheric pressure. Therefore, a rough pump is needed, which creates a medium vacuum before the turbomolecular pump can be started. To generate the necessary pre-vacuum for the turbomolecular pump, a dual stage rotary vane pump (*Agilent DS 102*) is used. A circular rotor is located offset in a circular cavity. During the rotation silicon oil is transported from the inlet towards a chamber of increased volume and then through the outlet of same volume, creating a vacuum down to  $10^{-3}$  mbar. At this pressure, the turbomolecular pump can be started.

The pressure gauge is connected through a T-flange and an extension below the table, to bring the magnet around the gauge as far away from the electron gun as possible (Figure 13.f, dark green). The full range gauge (*Agilent FRG-700 CF35*) measures the pressure inside the vacuum chamber. The gauge combines a pirani gauge with an inverted magnetron detector to allow full range detection. The pirani gauge measures the pressure by thermal conductivity and thus can be used only from  $10^2$  mbar down to  $10^{-4}$  mbar. Below that pressure, the vacuum pump controller switches to the inverted magnetron gauge, also referred to as cold cathode or cold ionization gauge. This gauge can measure the pressure down to  $5 \cdot 10^{-9}$  mbar. Within the gauge, a direct current leads to emission of thermal electrons from the cathode. Those electrons collide with gas molecules, generating secondary electrons and positive ions. Again, these ions are accelerated towards the cathode, generating new electrons upon impact. In result, a strong electric

near field can be detected close to the cathode. The intensity of this detected signal can be calibrated and correlated with the pressure inside the vacuum chamber.

The electron gun is aligned horizontally at the six-way cross (Figure 13.f). The LEE source is a flood gun (*Omnivac* FS100) with a tungsten hairpin filament (FIL), generating thermal electrons, and a Wehnelt cylinder (WEH). An electrostatic lens (EXT) in front of the Wehnelt cylinder extracts the electrons and accelerates them toward the sample. A Mu-metal housing around the electron gun shields it from magnetic fields. It is connected with a metal ring (ANO), grounding both with the vacuum chamber. Two ceramic rings isolate WEH and EXT from the grounded construction.

### **3.1.2. The custom built sample stages**

The first custom built sample stage is aligned vertically to the electron gun. It consists of an eight sided sample holder which is insulated from the chamber with a ceramic between two metal rods (Figure 13.d). The Si/SiO<sub>2</sub> samples (Figure 13.e) are fixed with conductive copper tape. The maximum sample size is 12 x 12 mm<sup>2</sup>. The sample holder is electrically connected *via* a copper sliding contact (DN16 ring) and a BNC feed through with the picoammeter (*Keithley* 6485E). The electron current can therefore be measured in real-time during irradiation. The stage can be positioned vertically with a z-translator over 50 mm travel distance (Figure 13.f, orange) and rotated by 360° (Figure 13.f, yellow).

Although the described sample stage allows real-time measurements during irradiation, beam profile determination is rather difficult, since the current on the whole stage is measured. Therefore, another stage was constructed in cooperation with *Miloš Lj. Ranković* (Institute of Physics, University of Belgrade) within a joint DAAD project. This stage is grounded on the outside along with the samples and contains an isolated faraday cup, held in position by two teflon rings (Figure 13.c). An 8 mm diameter hole in the aluminum housing in front of the faraday cup allows to collect the complete electron beam. To determine the beam profile, a cover with a central hole of 1 mm diameter can be attached at the sample stage. Since the sample stage is grounded, no real-time measurements during irradiation can be done in this configuration. Therefore, this stage is used only for beam characterization while the insulated stage is used for sample irradiation itself, since the electron current is in general not constant during irradiations (see chapter 3.2).

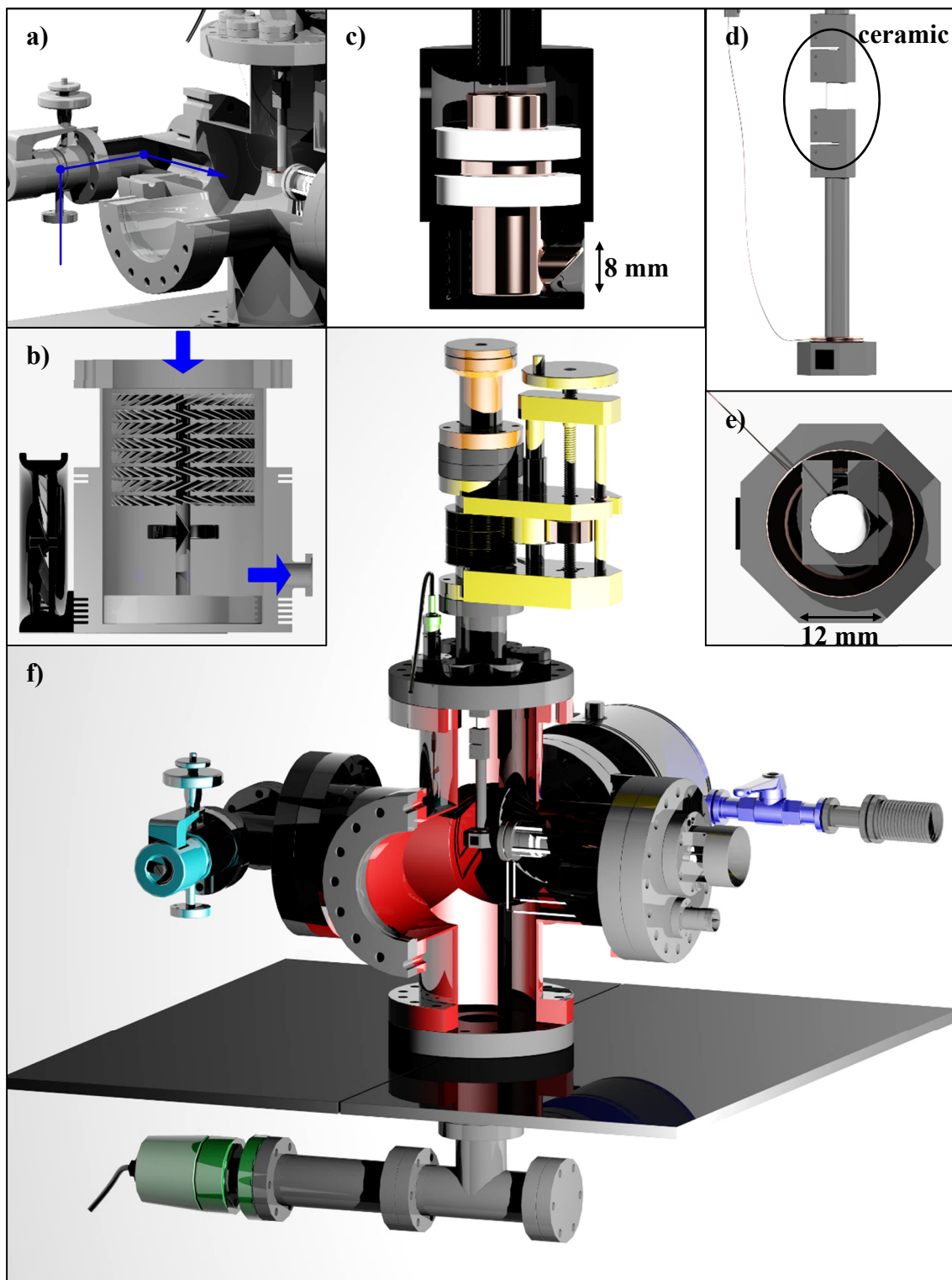


Figure 13. 3D model of the vacuum chamber. The central figure **f**) shows the final setup with the six-way cross (red), the rotor (orange), the z-translator (yellow), the BNC feed through (bright green), the valve (bright blue), the turbomolecular pump (dark blue), the pressure gauge (dark green), the electron gun and the sample stage. Additionally, in **a**) the gas inlet pathway is shown and in **b**) the gas outlet pathway. In **c**) the faraday cup sample stage is shown in cross section. The measurement sample stage is shown in **d**) from the side with the ceramic and in **e**) in top view.

### 3.1.3. Modification of the electron gun

The commercial flood gun is intended to provide high electron currents. To avoid that too many electrons hit the sample in short time, charging the surface<sup>132</sup> as well as reduce the irradiation time to extremely short times, the electron gun was modified. In order to defocus the beam, a small potential was applied to the last electrostatic lens (ANO, Figure 14, green). Since this lens was originally grounded *via* the Mu-metal housing, the housing was removed and ANO connected *via* a new electric 5-pin feed through and asymmetric reduction flange (DN100 to DN40 and DN16) to a power supply (*GW Instek* GPD-2303S), applying a small voltage (1.5 V for 10 eV, 1.3 V for 5.5 eV). With decreasing kinetic energy of the electrons the defocusing influence of ANO increases. In result, fewer electrons reach the sample. To keep the current at the sample constant, the voltage at ANO needs to be reduced.

To control the electron beam, an electron beam shutter is needed. Therefore, an additional custom built electrostatic lens (SHU, Figure 14, red) was positioned in front of the electron flood gun with ceramic spacers. If SHU is grounded, the electrons will pass the 4 mm diameter aperture. If a voltage of 14 V is applied (*Voltcraft* VSP 2653), the beam will be totally defocused and no electrons will reach the sample.

For a precise control of the electron beam, the commercial flood gun controller (*Omnivac* PS-FS100) is replaced by manually tunable power supplies (Figure 15). The optimal setup has been determined for 10 eV and 3 nA current on a silicon sample.

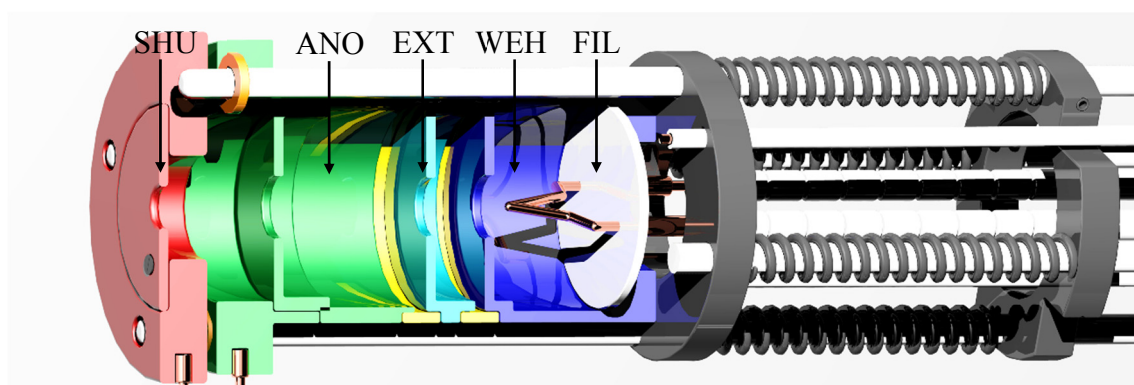


Figure 14. 3D model of the electron gun with the filament FIL (copper), the Wehnelt cylinder (dark blue), the electrostatic lens EXT (bright blue) between two ceramics (yellow), the modified electrostatic lens ANO (green), the ceramic spacer (orange) and the additionally implemented electrostatic lens SHU (red).

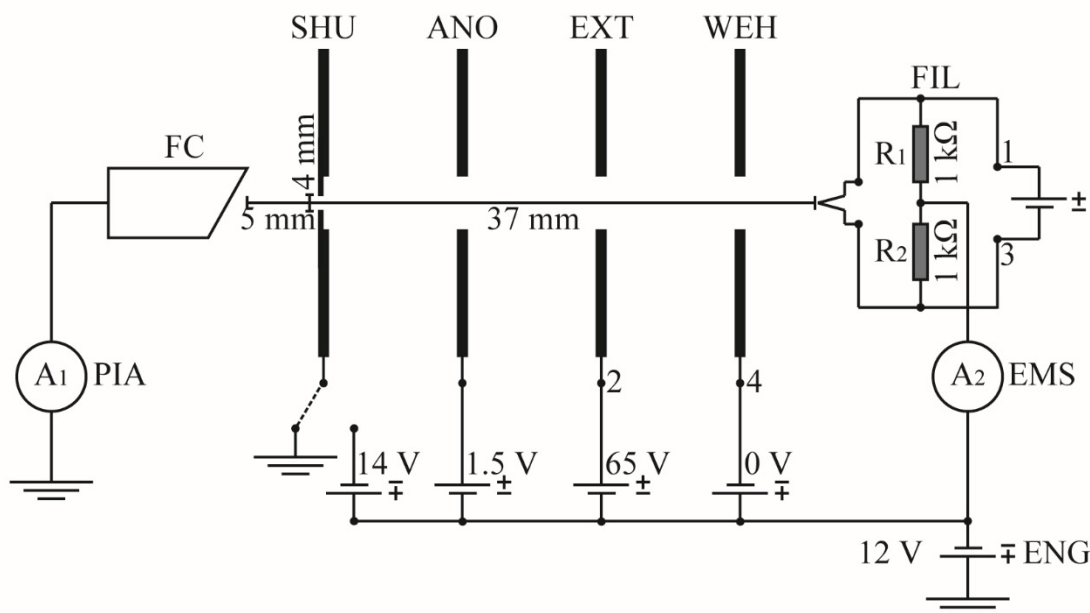


Figure 15. Technical drawing of the circuit of the electron gun, with the picoammeter (PIA) connected to the faraday cup (FC), the shutter (SHU) either grounded or set to -14 V, the anode (ANO) set to 1.5 V, the extractor (EXT) set to 65 V, and the Wehnelt cyclinder (WEH), and the beam voltage of 12 V (ENG). A multimeter (EMS) controls the emission current from the filament (FIL). The 4 pins of the electric feed through at the electron gun are numbered with 1-4. SHU and ANO are connected at the additional feed trough. ENG and ANO have to be varied depending on the desired energy of the electrons.

#### **3.1.4. Improvement of the venting process**

The venting system (Figure 13.a) was carefully modified since it turned out that a rapid venting can decompose the DNA origami structures (see chapter 3.5). Therefore, a UHV dosage valve with gas inlet and sapphire seal (*Vacom* 11LVM-4016CF-MS-S) is used for very soft venting, connected by a DN40 T-flange, resulting in two 90° angles to create many small turbulences in the airflow. In this way fast entering of gas molecules is avoided that can create a pressure front hitting the sample surface. Additionally, the sample stage is moved up to the highest position during venting to take the sample out of the direct airflow.

## **3.2. Characterization of the electron beam**

### ***3.2.1. Defined settings for the electron gun***

The beam is shaped by the settings of the electron gun. Those settings are defined by three experimental aspects. First, the desired electron energy has to be set. Second, only a small electron current shall illuminate the sample to minimize sample charging.<sup>132</sup> Third, the beam needs to be slightly defocused to increase the homogeneously irradiated area. The optimization process resulted in 2.1 A for FIL and 65 V for EXT. The ANO voltage was set to 1.5 V for 10 eV electron energy to defocus the electron beam. For experiments with lower electron energies, ANO needs to be reduced to increase the electron current on the sample.

The potential difference between the filament and the sample has to be at least 10 V for 10 eV electrons. However, charging of the silicon surface may result in an additional repulsive potential, reducing the electron energy. Thus an experiment was performed to determine the surface charging (Figure 16). Below 2.0 V no electrons passed the silicon surface. Therefore, the voltage to accelerate the electrons (ENG) was set to 12 V to compensate the surface charging and irradiate the sample with 10 eV electrons. For irradiations with 5.5 eV, ENG was set to 7.5 V. Additionally, the energy distribution of the electron beam was obtained (Figure 16). A beam containing only electrons of identical energy would exhibit a current voltage characteristics similar to a Heaviside step function. However, the filament generates electrons with a finite energy distribution, resulting in a gradual increase of the current with increasing electron energy. The energy distribution can be obtained from the full width at half maximum (FWHM) of the gauss fit of the first derivative of the measured current. The electron energy distribution was experimentally measured to be  $1.2 \pm 0.1$  eV.

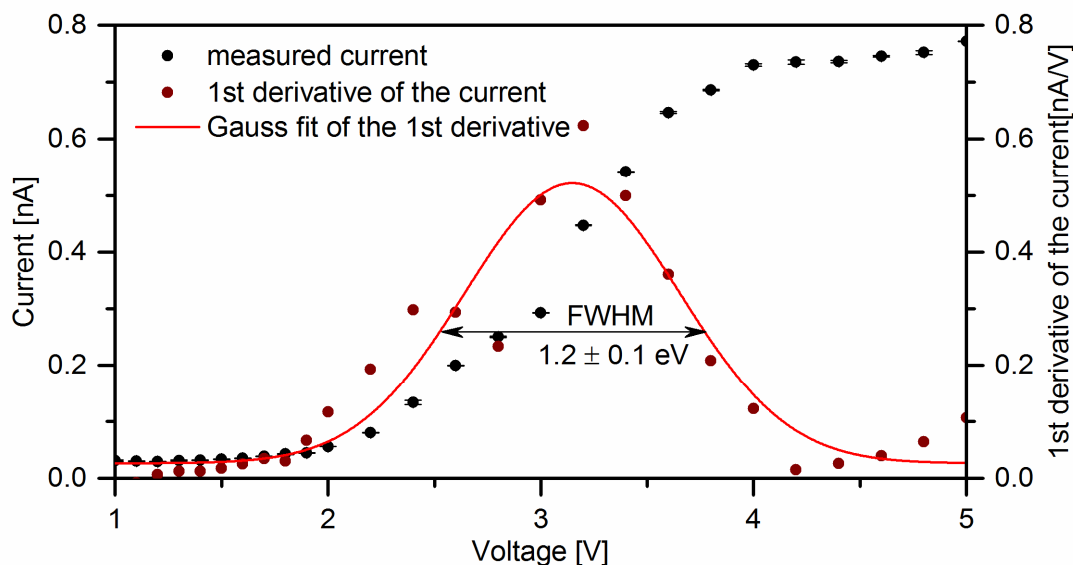


Figure 16. Diagram of the measured charging effect of the silicon surface with calculation of the energy distribution of the electron beam.

### 3.2.2. *Characterization of the beam profile*

For fluence determination at a certain position on the sample, it is necessary to characterize the beam profile. The faraday cup containing sample stage was used to determine the beam profile by moving it vertically through the beam at defined height increments of 0.2 mm. At each height position the current was measured and averaged over 15 seconds. The average and error of each current measurement was plotted as a function of the  $z$  coordinate to visualize the beam profile (Figure 17). Here,  $z = 0$  mm corresponds to a height position of the faraday cup aperture of 29.6 mm. To account for aging of the filament, the beam profile was determined periodically (see chapter 3.3, table 1).

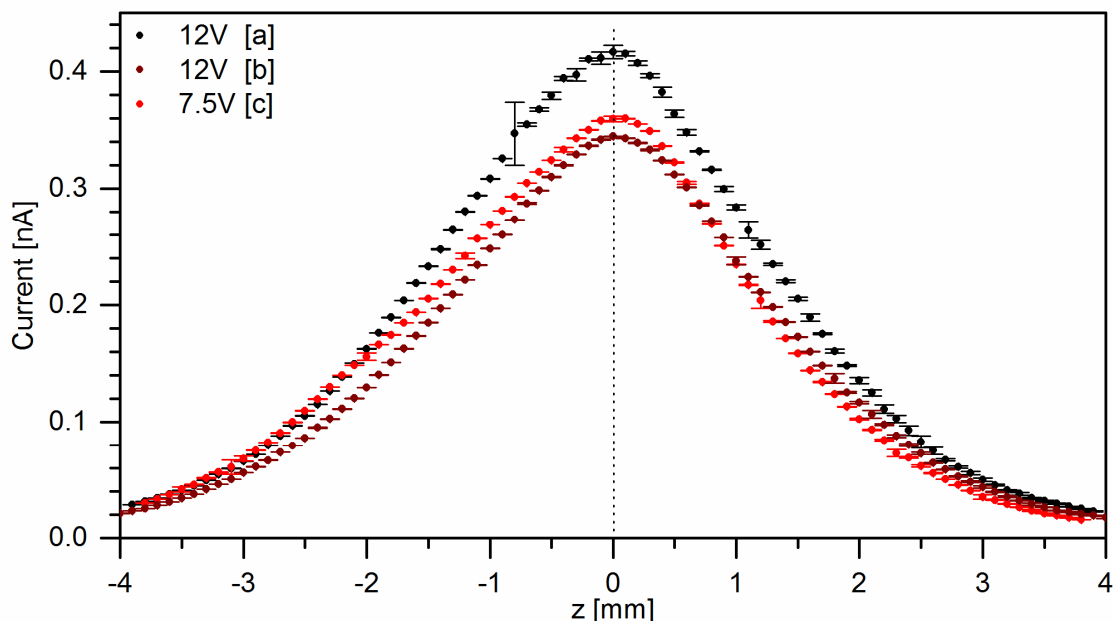
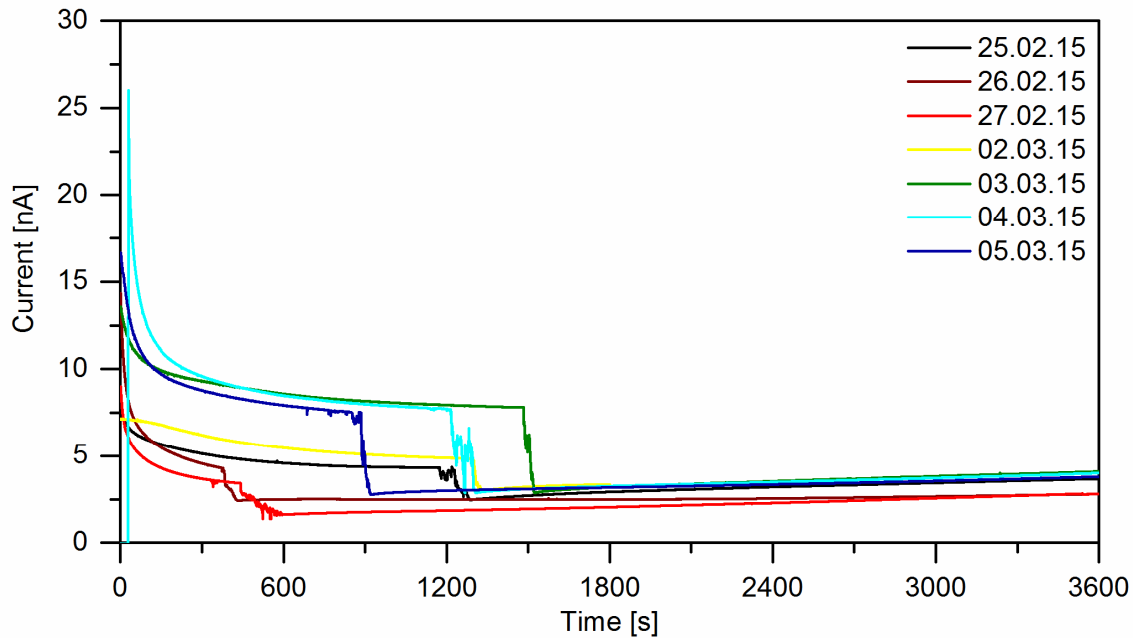


Figure 17. Beam profile for three separate experiments, a) a warm-up period of 90 minutes and 12V, b) a warm-up period of 30 minutes and 12V, and c) a warm-up period of 30 minutes and 7.5V to accelerate the electrons.

### 3.2.3. *Influence of the warm-up period on the beam profile*

Experiments have shown, that longer warm-up periods of the electron gun result in a slightly more focused beam profile (Figure 17.[a]). The filament current is set to 2.1 A and is instantly warm. However, the electronic lenses and surrounding of the electron gun warm up slowly, influencing the beam profile in diameter and electron current. Usually, this warm-up period is chosen to be exactly 30 minutes (see chapter 7.2.2.6.5.). Longer warm-up periods result in a slightly better focused beam. This effect results from the slow stabilization of the electron beam over several hours. Since scattered electrons and heat from the filament over such extended periods of time may damage the origami samples, the warm-up period was kept at 30 minutes and the beam current during irradiation was monitored in real-time. On the other hand, a shorter warm-up period is not advisable, since a rapid drop in the beam current from around 10 nA to less than 5 nA occurs within the first 30 minutes, probably caused by the thermal evaporation of residual adsorbates inside the electron gun (Figure 18).



#### 3.2.4. *Influence of the electrostatic shutter on the electron current*

The beam shutter SHU have also shown a critical influence on the beam current. In initial experiments, SHU was closed for changing the sample between irradiations by rotating the stage. When opened afterwards, a strong decrease of the current was measured on the sample within the first few seconds (Figure 19). To eliminate this effect, irradiations have also been performed with open shutter between irradiations. The change of samples was performed within a 2 seconds interval in which the current measurement was interrupted. This modification results in a more constant irradiation current without the initial drop of the electron current (Figure 20). Due to the short 2 seconds interval for changing the samples, the effect of stray electrons on the fluence is estimated to be below 10 %.

Figure 18. Measurements of the beam current over time during an electron gun warm-up period of one hour.

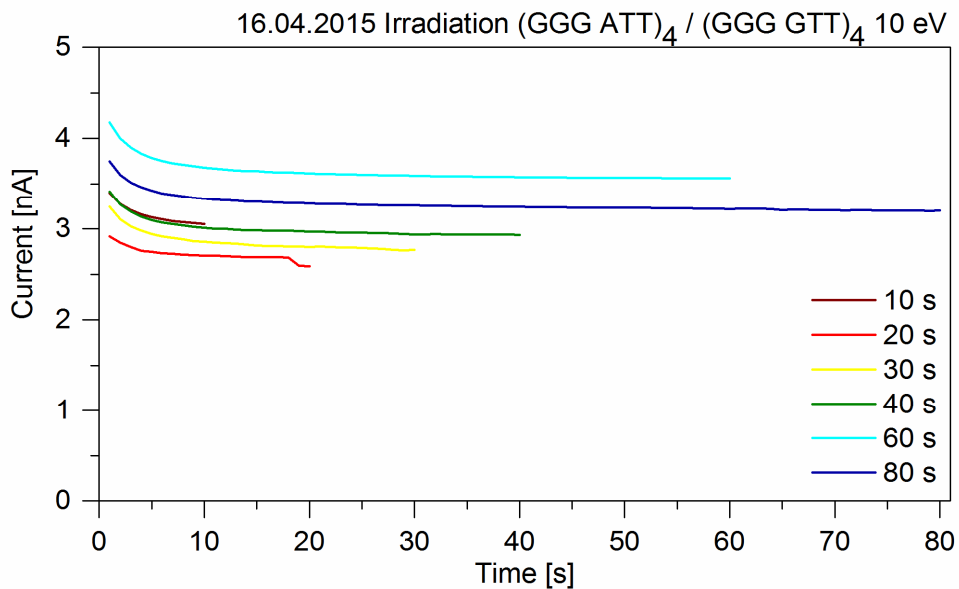


Figure 19. The irradiation of Telo4/Telo4G as an example of current measurements performed with closed shutter between experiments (Detection with “PIA Single.py”).

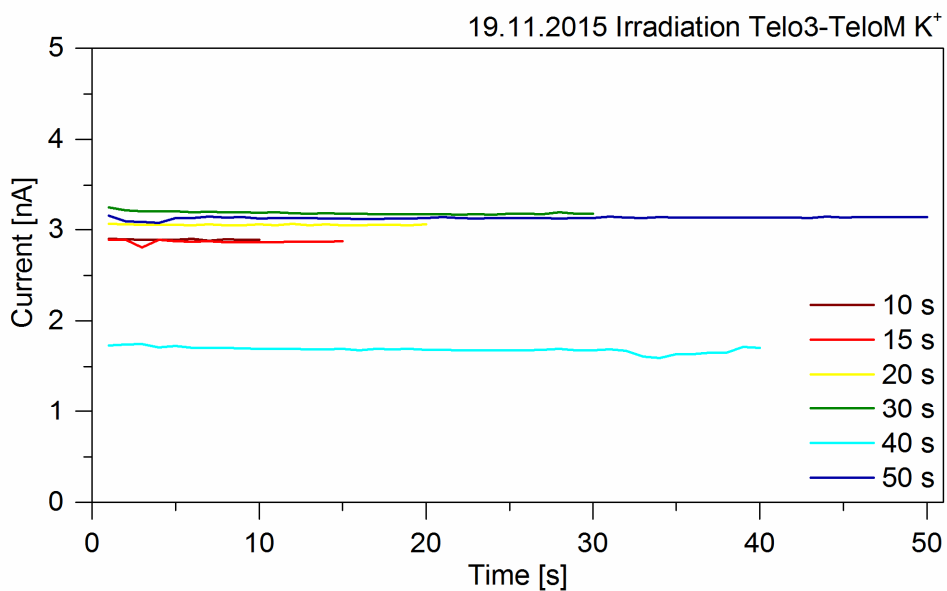


Figure 20. The irradiation of Telo3/TeloM as an example of current measurements performed with the shutter left open between experiments (Detection with “PIA All.py”).

### 3.3. Fluence calculation

#### 3.3.1. Definition of the electron fluence on the sample

The fluence  $F$  is defined as the ratio of the total number of electrons  $N_e$  and the area of irradiation  $A$  (eq. 01). The number of electrons  $N_e$  can be calculated from the time of irradiation  $t$  multiplied by the current  $I$  measured at the sample, divided by the elementary charge  $e$ .

$$F = N_e/A = (t \cdot I/e)/A \quad (01)$$

With  $1A = 1C/s$  and  $1C = 6.24 \cdot 10^{18}$  electrons, the number of electrons illuminating the surface is calculated directly from the current in nano ampere. For the experiments, the fluence was calculated with the measured current in nA by using

$$F [1/cm^2] = I[nA] \cdot 6.24 \cdot 10^9 [1/(nA \cdot s)] \cdot t[s]/A[cm^2].$$

In real-time measurements during irradiation, the total current at the sample is measured. Thus, the area of irradiation  $A$  corresponds to the total area irradiated by the beam. According to the beam profile measurements (see chapter 3.2.2) the width of the beam profile is between 7 and 8 mm. Due to the shape of the beam profile, more electrons reach the sample at the central region than at the outer regions. Therefore, if the fluence  $F$  is calculated with the total current  $I_{total}$  and the total area  $A_{total}$ , an average value for  $F$  is the result. The surface analysis is done using AFM images of  $4 \times 4 \mu m^2$  size. Thus, even with several AFM images, only a small fraction out of the total irradiated area  $A_{total}$  can be analyzed in the single molecule studies. As a result, the determined number of strand breaks for each image would vary strongly due to the correlation to the average fluence. To solve this problem it is necessary to determine precisely the fluence at the position of the AFM image within the beam profile. For this, a constant subarea  $A_i$  has to be defined and the current  $I_i$  in this area needs to be determined. This current  $I_i$  cannot be determined during irradiation, since only the total current  $I_{total}$  is measured. However, in a separate experiment with the faraday cup, the current  $I_i$  can be measured at a position  $z_i$  within the beam profile.

### 3.3.2. Determination of the current in a discrete area

The 2D beam profile is divided into discrete, non-overlapping areas  $A_i$  for which the corresponding  $I_i$  values are determined. Since the aperture of the faraday cup sample stage used for beam profile measurements has a diameter of 0.1 cm, each  $A_i$  is defined as a discrete circle with  $r_c = 0.05$  cm and a center with a distance  $r_i$  to the center of the beam profile (Figure 21.a). For each  $A_i$  the corresponding  $r_i$  can be calculated with the 2D coordinates and the Pythagorean theorem  $r_i = \sqrt{z_i^2 + y_i^2}$ .

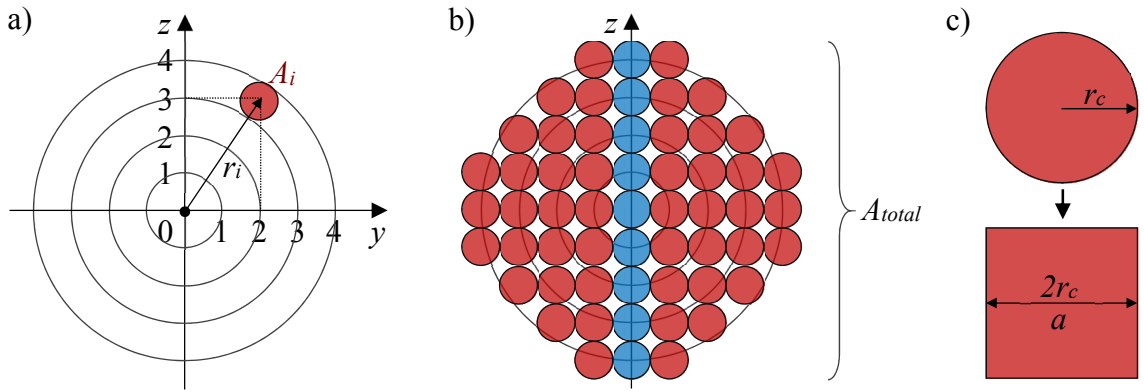


Figure 21. a) Schematic drawing of the total beam profile  $A_{total}$  with one discrete area  $A_i$  with a distance of  $r_i$  to the center of the beam. b) Drawing of the beam profile with discrete areas  $A_i$  along the  $z$ -axis (blue) and determined from  $r_i$  (red). c) Drawing to illustrate the conversion of the circular area  $A_i$  into a square with the size of  $2r_c$ .

The beam profile is assumed to have rotational symmetry. Thus, all  $A_i$  with distance  $r_i$  from the center of the beam can be correlated to corresponding areas on the  $z$ -axis with  $z_i = r_i$  (Figure 21.b). The  $I_i$  for these  $z_i$  can be measured by changing the stage height and position of the aperture in front of the faraday cup.

The fluence within one area  $A_i$  is assumed to be homogeneous. To cover the whole area of the beam profile, the circular area is transformed into a square. The circular area is defined as  $A_{circle} = \pi r_c^2$ , while the square is defined as  $A_{square} = a^2$ . The length  $a$  of the square is twice the radius of the circle  $r_c$ . Thus, for the current value transformation from the circle  $I_i$  to the square  $I_i^*$ ,  $I_i$  needs to be multiplied by  $4/\pi$ .

$$(A_{circle}/\pi) \cdot 4 = A_{square}$$

$$I_i \cdot 4/\pi = I_i^*$$

The total current  $I_{total}$  is then calculated by summing up all currents  $I_i^*$ .

$$I_{total} = \sum_{n=0}^i I_i^*$$

For each area  $A_i$  a current percentage  $I_{\%}$  is defined as

$$I_{\%} = I_i^*/I_{total} \quad (02).$$

This method allows for the direct calculation of the fluence at a certain sample subarea  $A_i$  from measured current values along the  $z$ -axis. Thus, no further theoretical models or fits are required. This makes the fluence calculation more reliable and precise.

For the data presented in this work, the fluence of the central area of the beam was calculated and is listed below (Table 1). Since the profile slightly changes during the lifetime of the filament, the beam profile determination was repeated several times. The experiments were done with very short irradiation times of below 2 minutes, thus the beam profile can be assumed to be constant over this short time. With an electron gun warm-up period of exactly 30 minutes, the determined beam profile can be used for  $I_{\%}$  calculation of the subareas on the samples irradiated with identical conditions.

Table 1 contains five different beam profiles. Profile 1 was obtained with a fresh filament had a slightly more focused beam profile than profiles 2 and 3 taken later. For several months the profile stayed constant at both energies 12 V and 7.5 V. After a large number of irradiation experiments, the beam profile was slightly narrowed (profile 4 and 5). Both profiles 4 and 5 were measured directly after each other. Compared with profile 4, the  $I_{\%}$  value of profile 5 is increased in the central area. This underlines the importance of a defined and constant warm-up period. While the warm-up period of profile 4 was exactly 30 minutes, for profile 5 the period was three times longer. The  $I_{\%}$  value in the central area is increased by 4 % for the three times longer period. The increase of 4 % in 60 minutes confirms the assumption of a constant beam profile during few minutes irradiation.

Table 1. List of all beam profile characterizations with calculated percentage of the current  $I\%$  [%] of each discrete circular area  $A_i$  from the measured current  $I_i$  [nA] at the corresponding position  $r_i$  [mm] within the beam profile.

		Profile 1		Profile 2		Profile 3		Profile 4		Profile 5	
		06.03.15 / 12 V		06.08.15 / 12 V		03.11.15 / 7.5 V		04.12.15 / 12 V		04.12.15 / 7.5 V	
$r_i$ [mm]	Occurence	$I_i$ [nA]	$I\%$ [%]	$I_i$ [nA]	$I\%$ [%]	$I_i$ [nA]	$I\%$ [%]	$I_i$ [nA]	$I\%$ [%]	$I_i$ [nA]	$I\%$ [%]
0	1	0.1393	<b>7.04</b>	0.4169	<b>5.96</b>	0.0420	<b>5.94</b>	0.2306	<b>6.36</b>	0.0674	<b>6.62</b>
1	4	0.0823	4.16	0.2964	4.24	0.0278	3.93	0.1596	4.40	0.0445	4.37
2	4	0.0416	2.10	0.1491	2.13	0.0154	2.17	0.0751	2.07	0.0213	2.10
3	4	0.0198	1.00	0.0580	0.83	0.0064	0.91	0.0297	0.82	0.0085	0.84
4	4	0.0058	0.29	0.0264	0.38	0.0025	0.35	0.0125	0.34	0.0032	0.31
1.4	4	0.0646	3.27	0.2340	3.34	0.0222	3.14	0.1221	3.37	0.0321	3.15
2.2	8	0.0351	1.77	0.1249	1.79	0.0132	1.87	0.0627	1.73	0.0187	1.83
2.8	4	0.0204	1.03	0.0706	1.01	0.0077	1.09	0.0366	1.01	0.0107	1.05
3.2	8	0.0143	0.72	0.0479	0.68	0.0055	0.78	0.0247	0.68	0.0070	0.69
3.6	8	0.0064	0.33	0.0336	0.48	0.0035	0.50	0.0171	0.47	0.0047	0.46
4.1	8	0.0073	0.37	0.0240	0.34	0.0022	0.31	0.0117	0.32	0.0029	0.29

### 3.4. AFM analysis

#### 3.4.1. Strand positions on the DNA origami

The DNA origami triangles are assembled according to the original protocol by Rothmund (see chapter 2.6.2).<sup>24</sup> The circular single stranded genome m13mp18 with 7249 nucleotides is used as the scaffold. With specially designed oligonucleotides the viral strand is folded into the triangle pattern (protocol see chapter 7.1). Those 208 staple strands bind by Watson-Crick base pairing<sup>29</sup> at three separate positions of the scaffold strand with each third of the strand. The resulting DNA origami triangles can be analyzed by AFM imaging (Figure 22).

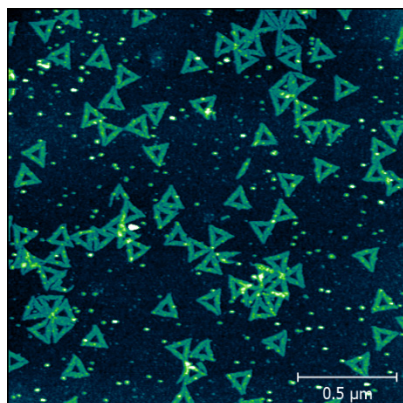


Figure 22. AFM image with DNA origami triangles on silicon.

The specially designed staple strands can be extended with a protruding DNA strand sequence representing the target sequence. Table 4 in chapter 7.1 contains all protruding DNA strand sequences used in the experiments of this work. In general, the nucleobase sequence under study is separated from the DNA origami *via* a 3' spacer of one or two T nucleobases. At the 5' end of the protruding strand, a Bt label is attached *via* two T nucleobases to the nucleotide sequence (Figure 22).

Since the DNA origami triangle has a symmetric geometry, the three trapezoids cannot be distinguished in the AFM images. On one trapezoid two protruding strands are attached. One strand is positioned in the center and one in the corner of the trapezoid, with a distance of 30 nm between both. The distance between these positions is sufficient to reliably distinguish both SAV at the end of the protruding strands in the AFM images. The asymmetric pattern is identical for all three trapezoids, as illustrated in Figure 23 with red protruding strands.

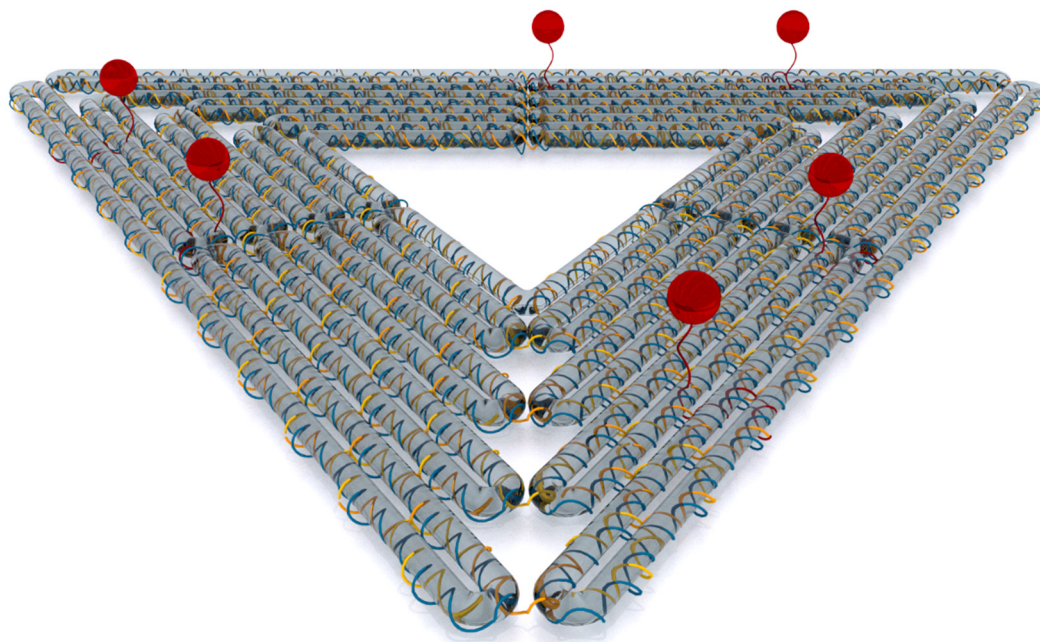


Figure 23. 3D model of the DNA origami triangle containing six protruding strands. As a guide to the eye, the glass tubes (grey) show the path of the double helices. The staple strands (yellow) fold the viral strand (blue) into the triangle pattern. The protruding strands (red) are extended staple strands with a SA<sub>v</sub> (red ball) at the 5' end.

#### 3.4.2. *AFM imaging*

As discussed in the description of the fluence calculation in chapter 3.3., it is of great importance to analyze the central (or well-defined) area of irradiation. All samples (except <sup>2</sup>F<sub>A</sub>, see chapter 4.3.5) were marked with a central cross, carefully scratched into the silicon surface. The DNA origami triangles were immobilized at the cross marker and the sample was mounted on the sample stage with the cross centrally positioned on the alignment grooves (Figure 24). Using the top-view camera of the AFM, the images were taken at  $(300 \pm 100) \mu\text{m}$  from the center of the marker (Figure 25), to coincide with the central circular area of 1 mm diameter, for which the fluence was calculated. At least one AFM image was taken in each quadrant separated by the cross marker with  $4 \times 4 \mu\text{m}$  image size, usually containing between 1000 and 2000 DNA origami structures.

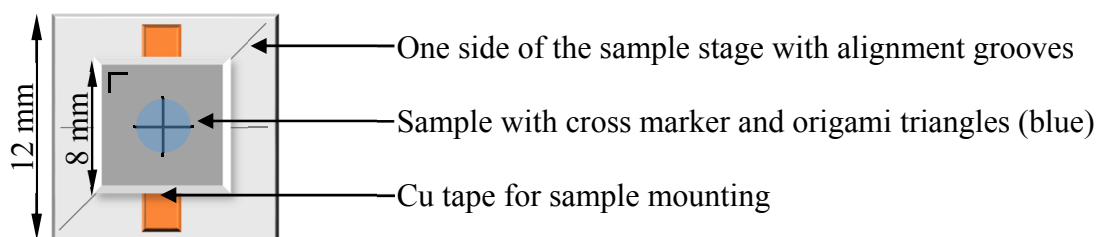


Figure 24. Schematic drawing to illustrate the mounting of the sample on the sample stage.

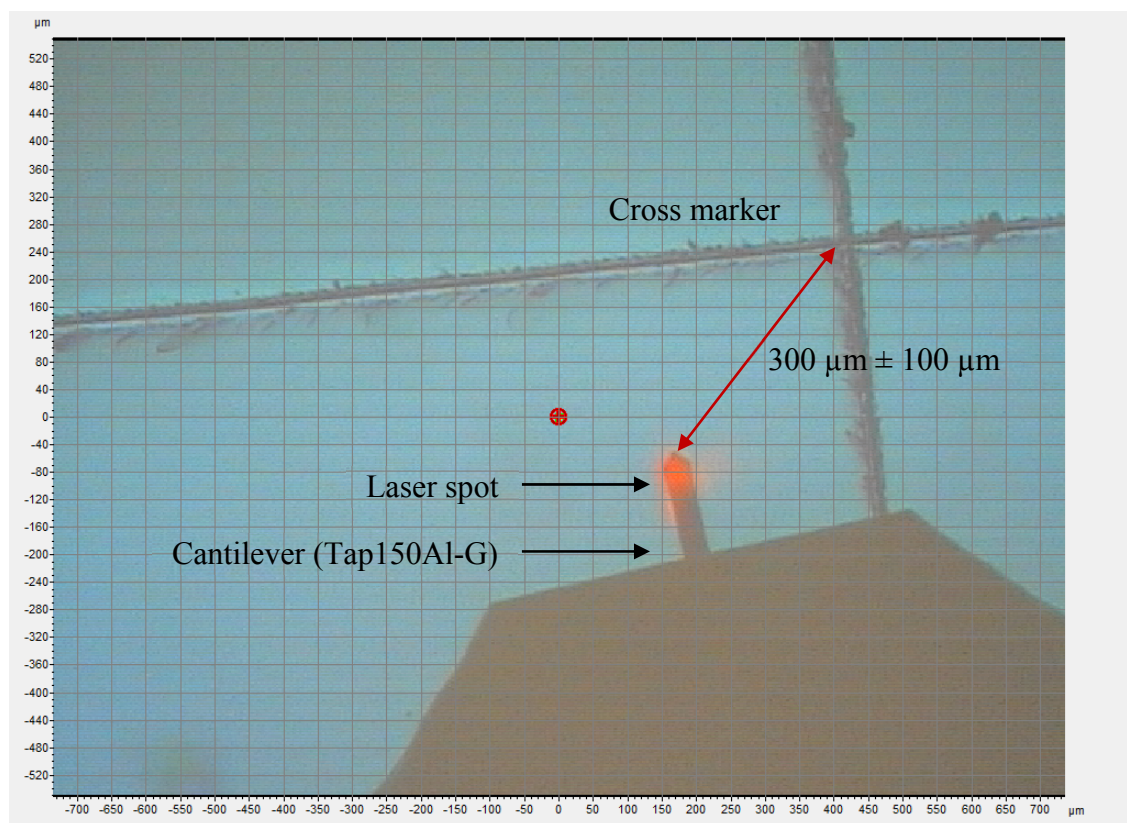


Figure 25. Microscope image showing the top-view of the sample with the AFM cantilever (Tap150Al-G). The tip of the cantilever (with the laser spot on top) is positioned ( $300 \pm 100$ )  $\mu\text{m}$  away from the center in the lower left corner of the cross marker.

### 3.4.3. *Statistical evaluation of the AFM images*

Within each AFM image, all intact DNA origami triangles (see chapter 3.5) were analyzed. The number of intact strands was counted, corresponding to their position on the DNA origami. If all protruding strands were intact, three SAV molecules at the corners of the triangle and three SAV molecules at the central positions of the DNA origami trapezoids are visible. In case that one or more single strand breaks occur, the protruding strand is no longer labelled with Bt and thus, no SAV can bind at the protruding strand. In result, the number of target strands on top of the origami will decrease. The number of strand breaks ( $N_{SB}$ ) is calculated as

$$N_{SB} = \left( 1 - \frac{\sum N_{SAv}}{3 \cdot N_{Origami}} \right) \cdot 100$$

with the number of still intact strands ( $N_{SAv}$ ) and the number of analyzed DNA origami ( $N_{Origami}$ ).  $N_{SB}$  is then plotted as a function of the fluence  $F$  (see chapter 3.6.1).

### **3.5. DNA origami preparation and stability**

#### ***3.5.1. Preparation and irradiation of DNA origami structures***

The triangular shaped DNA origami were folded using the original design of Rothmund.<sup>24</sup> The modified target strands and unmodified staple strands were combined to a mixture containing 0.15  $\mu\text{L}$  of each strand. Additionally, 5  $\mu\text{L}$  of the viral DNA strand m13mp18 (100 nM in 10 mM Tris and 1 mM EDTA), 10  $\mu\text{L}$  buffer (10 x TAE with 200 mM  $\text{MgCl}_2$ ), and 41.65  $\mu\text{L}$  deionized water were added to the solution (detailed sample preparation protocol see chapter 7.1). For annealing the prepared solution containing staples, scaffold and buffer was heated up to 80  $^\circ\text{C}$  and cooled down stepwise over 2 h to 4  $^\circ\text{C}$ . Subsequently, the annealed DNA origami triangle solution was filtered two times with 300  $\mu\text{L}$  1 x TAE buffer containing 20 mM  $\text{MgCl}_2$  with 6000 rpm for 5 minutes. The DNA origami containing filtrate was isolated and stored at 4  $^\circ\text{C}$ .

The silicon wafers were cut into 8 x 8  $\text{mm}^2$  pieces, marked with a central cross and cleaned with air plasma for 5 minutes, directly before DNA origami immobilization on the surface. From the freshly prepared origami solution one drop of 0.8  $\mu\text{L}$  was placed directly at the cross marker. To prevent drying effects, instantly afterwards 15  $\mu\text{L}$  of 10 x TAE with 200 mM  $\text{MgCl}_2$  buffer was added. The sample was incubated for 1 h at room temperature in an incubation chamber containing water to maintain high humidity to prevent drying. Subsequently, the sample was cleaned once with 1 mL of 1:1 deionized water/ethanol, and instantly placed in 10 mL ethanol for 1 h. Afterwards, the sample was dried with air and mounted on the sample stage for irradiation (detailed irradiation process see chapter 7.2). The UHV chamber was evacuated slowly down to  $10^{-3}$  mbar, before the turbomolecular pump was started. At a base pressure below  $1.0 \cdot 10^{-7}$  mbar the electron gun was switched on and warmed up for 30 minutes with 2.1 A at the filament. Subsequently, the sample stage was positioned in the electron beam and the samples were irradiated for several seconds. Afterwards, the sample stage was lifted up, and the electron gun was switched off and cooled down for 1 h. The UHV chamber was vented slowly to atmospheric pressure using the dosage valve. The irradiated samples were unmounted from the sample stage and incubated with a 50 nM solution of SAV in 1 x TAE buffer with 20 mM  $\text{MgCl}_2$ . After 2 minutes of incubation the sample was rinsed with 0.5 mL 1:1 water/ethanol and dried with air.

The stability of the triangular DNA origami on the silicon surface is strongly influenced by the preparation process, especially by the aging of the DNA material, the washing procedure, remaining water in the DNA origami, and the amount of  $\text{MgCl}_2$  in the SAV solution and its incubation time. These aspects are discussed in the following.

### 3.5.2. *Aging of the DNA staple strands*

Comparative experiments with fresh and one year old staple strands revealed a strong influence of aging on the quality of the assembled DNA origami. While fresh staple strands led to perfectly triangular shaped DNA origami structures, the preparation with aged staple strands led to deformed DNA origami fragments, mainly ruptured at the corners (Figure 26). This observation was attributed to possible contamination or the staple strand storage in water, which might have damaged the staple strands. Hence the folded DNA origami contained fragmented staple strands and was therefore more sensitive towards structural damage. The corners are the weakest point within the origami structure since they are formed by only four staple strands per corner. Furthermore, these staple strands are shorter than the usual 32 nucleotides and contain unpaired bases within the turn from one trapezoid to another (Figure 27).

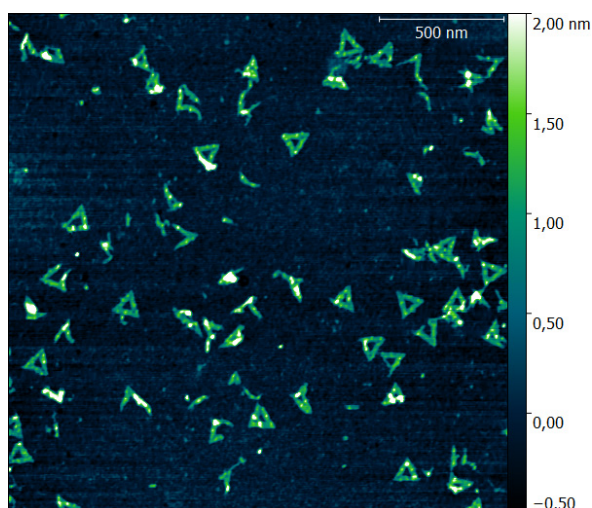


Figure 26. AFM image of an irradiated sample at 10 eV for 30 s, with prior ethanol drying and air flow control (image size  $2 \times 2 \mu\text{m}^2$ , height scale -0.5 to 2.0 nm).

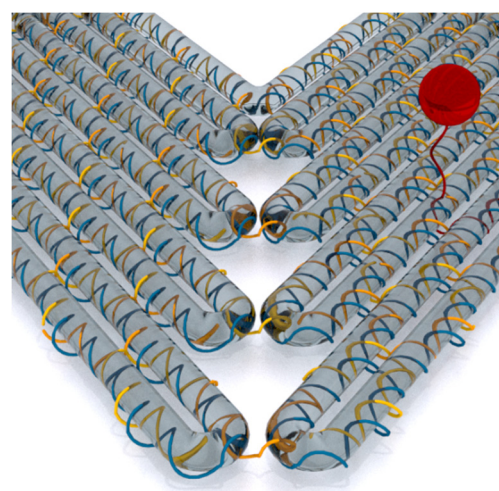


Figure 27. 3D model of the DNA origami triangle corner, with the staple strands (yellow) connecting two trapezoids.

Furthermore, the triangles with aged staple strands tend to form aggregates during the adsorption. At similar concentrations of origami and buffer, the aged DNA origami formed aggregates at the surface with many overlapping triangles, while most of the surface remained unoccupied (Figure 28). On the other hand, DNA origami prepared with fresh staple strands formed monolayers but no aggregates. Since the sensitivity of aged triangles appear only after the complete experimental process, the clustering behavior can

be used as indication for the DNA origami quality. It is directly visible with AFM after the incubation process.

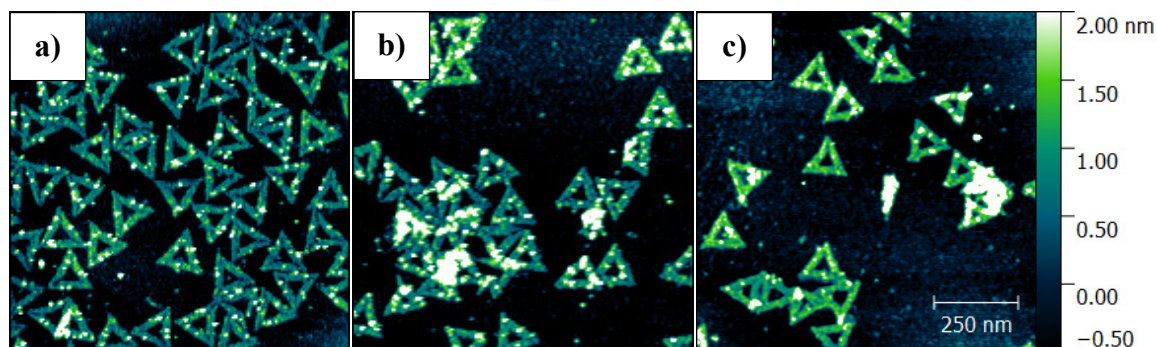


Figure 28. AFM images of a) intact DNA origami triangles after irradiation with 10 eV electrons for 20 s, b) aggregated triangles after incubation (non-irradiated) and c) aggregated triangles after irradiation with 10 eV electrons for 20 s (image size  $1 \times 1 \mu\text{m}^2$ , height scale -0.5 to 2.0 nm).

The destabilizing effect of aged staple strands can be reduced with increased concentration of  $\text{MgCl}_2$ . The DNA origami stays intact within a solution containing up to 200 mM  $\text{MgCl}_2$ . The high  $\text{MgCl}_2$  concentration stabilizes the DNA origami structure and improves the adsorption on the silicon surface. Since the DNA origami are attached stronger to the surface, they cannot be washed away as easily.

### 3.5.3. Washing procedure

The washing procedure showed a strong destructive effect on the DNA origami, even when prepared with fresh staple strands. Therefore, the effect of washing on DNA origami stability was investigated in more detail. To this end samples were subjected to different numbers of washing steps, consisting of rinsing with 2 x 1 mL ethanol/water mixture (Figure 29). The amount of damage in the DNA origami structure is clearly increasing with each additional washing step. This is due to the  $Mg^{2+}$  ions being washed away increasing the electrostatic repulsion in the DNA origami which leads to fragmentation.

All samples were rinsed fast and aligned vertically to remove the liquid quickly. In another experiment, the sample was rinsed once with the same volume over a longer time with the sample aligned in  $45^\circ$  angle. Hence, the liquid stayed longer on the surface, removing an increased amount of  $Mg^{2+}$  ions. The resulting damage is comparable to two or three washing steps when rinsed quickly (Figure 29.f).

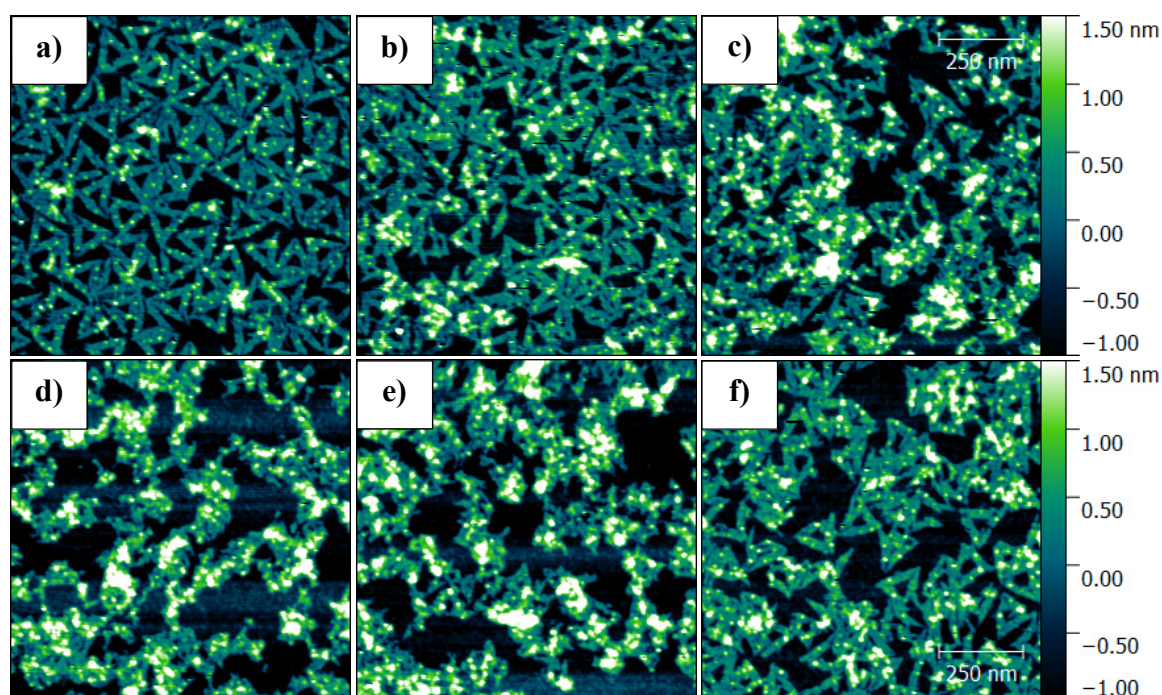


Figure 29. AFM images of DNA origami triangles after washing with 2 x 1 mL ethanol/water and drying for a) one time, b) two times, c) three times, d) four times, e) five times and f) one time slowly with a sample alignment of  $45^\circ$  angle (image size  $1 \times 1 \mu\text{m}^2$ , height scale -1.0 to 1.5 nm).

#### 3.5.4. *Water molecules in the DNA origami*

In previous publications it was assumed that remaining water inside the DNA material damages the DNA structure during the evacuation process due to rapid evaporation.<sup>133</sup> To avoid this effect, the samples are dehydrated by immersion in pure ethanol for one hour prior to introduction into the UHV chamber. Furthermore, the evacuation process from atmospheric pressure down to  $10^{-2}$  mbar was slowed down. This soft evacuation over 10 minutes allows a slow evaporation of the remaining water molecules inside the DNA origami, leaving the DNA structure intact. Additionally, the ventilation process from  $10^{-4}$  mbar to atmospheric pressure was slowed down as well. As mentioned in chapter 3.1, a precise ventilation valve was mounted with a T-flange on the chamber. Hence the air flow was precisely controlled and diffused before reaching the sample surface, thus avoiding shock waves hitting and possibly damaging the DNA origami samples.

Since evacuation and ventilation processes might damage the DNA origami structures if done too fast, each series of samples contains a non-vacuum control. If both  $N_{SB}$  are identical within the margin of the error, they are combined to the non-irradiated  $N_{SB}$ . In case both  $N_{SB}$  are significantly different, the whole sample series is not included in the statistical analysis and thus has to be repeated.

Experiments with hydrated DNA origami structures and fast evacuation and ventilation of the UHV chamber led to entirely destroyed DNA origami (Figure 30), revealing the importance of the dehydration steps.

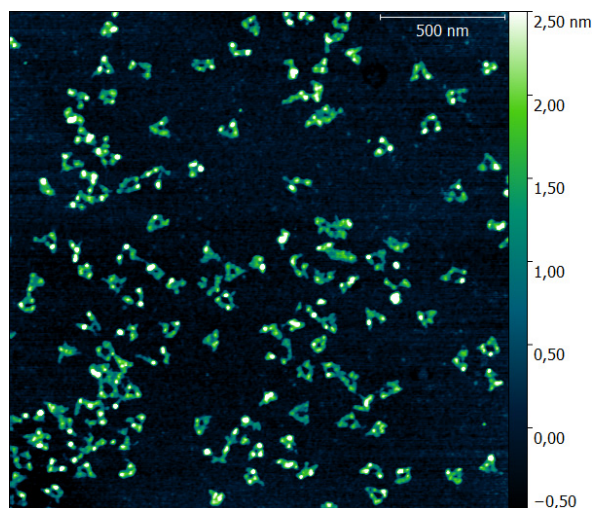


Figure 30. AFM image of a non-irradiated test sample, mounted inside the UHV chamber, without prior ethanol drying and air flow control during evacuation and ventilation. (image size  $2 \times 2 \mu\text{m}^2$ , height scale -0.5 to 2.5 nm).

### 3.5.5. *SAv incubation - concentration*

For the incubation with SAV, 1 x TAE buffer containing 20 mM MgCl<sub>2</sub> was used. Since the decreased MgCl<sub>2</sub> concentration in the SAV solution compared to the incubation buffer (200 mM MgCl<sub>2</sub>) might reduce the ion concentration in the DNA origami and the surface, the possibility to increase the concentration of MgCl<sub>2</sub> within the SAV solution was studied (Figure 31). In case SAV incubation is performed in pure water, the DNA origami triangles are extremely deformed and degraded (Figure 31.a). Due to the loss of Mg<sup>2+</sup>, the DNA structure destabilizes due to electrostatic repulsion between the negative charges of the DNA backbone. With fresh staple strands, less defects occur in the DNA origami structures. Thus, smaller amounts of MgCl<sub>2</sub> are sufficient for maintaining the triangular DNA origami shape during immobilization. Perfectly shaped DNA origami structures or misshaped triangles are directly visible in the AFM images. A slight improvement of the DNA origami stability and their immobilization is visible in the AFM images in case the ion concentration is increased from 20 mM (Figure 31.b) to 50 mM MgCl<sub>2</sub> (Figure 31.c). Further increase of the Mg<sup>2+</sup> ion concentration does not yield any further improvement of quality (Figure 31.d). When the concentration of the buffer is 10-fold increased, no quality improvement can be detected within the AFM images, while the SAV concentration on the triangles decreases (Figure 31.e-f), conceivably by denaturation or clustering of the SAV caused by the high concentration of tris acetate-EDTA.

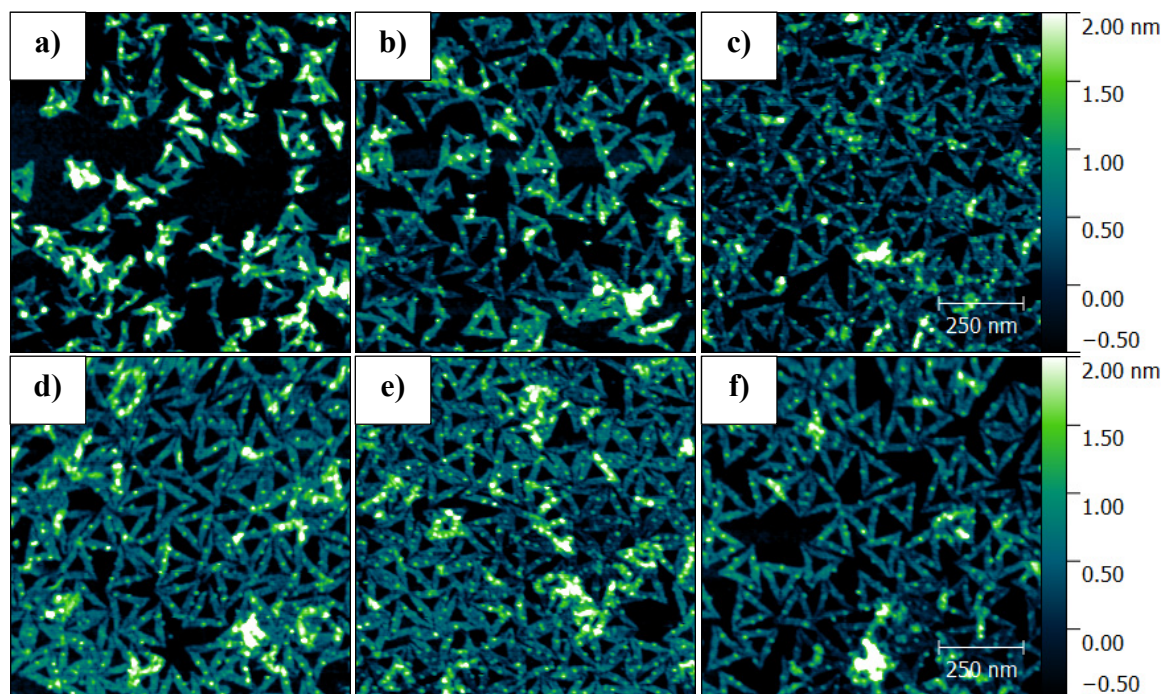


Figure 31. AFM images of DNA origami triangles after incubation with a 50 nM SAV solution in a) H<sub>2</sub>O, b) 1 x TAE + 20 mM MgCl<sub>2</sub>, c) 1 x TAE + 50 mM MgCl<sub>2</sub>, d) 1 x TAE + 100 mM MgCl<sub>2</sub>, e) 10 x TAE + 100 mM MgCl<sub>2</sub> and f) 10 x TAE + 200 mM MgCl<sub>2</sub>. (image size 1 x 1  $\mu\text{m}^2$ , height scale -0.5 to 2.0 nm).

### 3.5.6. *SAv incubation - time*

The effect of SA<sub>v</sub> incubation time on the DNA origami stability and shape was investigated for a concentration of 20 mM MgCl<sub>2</sub> in 1 x TAE buffer. Experiments with fresh staple strands did not show any influence of the SA<sub>v</sub> incubation time (Figure 32.d). Comparing samples after incubation times of 2 and 10 minutes, the DNA origami quality and amount of SA<sub>v</sub> labelled strands were identical. On the other hand, when aged staple strands were used, incubation time was found to strongly influence the quality of the DNA origami (Figure 32.a-c). Increasing the incubation time led to increasingly deformed DNA origami, while their number on the surface strongly decreased. Thus, the SA<sub>v</sub> incubation time was kept at precisely 2 minutes in all experiments, to minimize DNA origami damage.

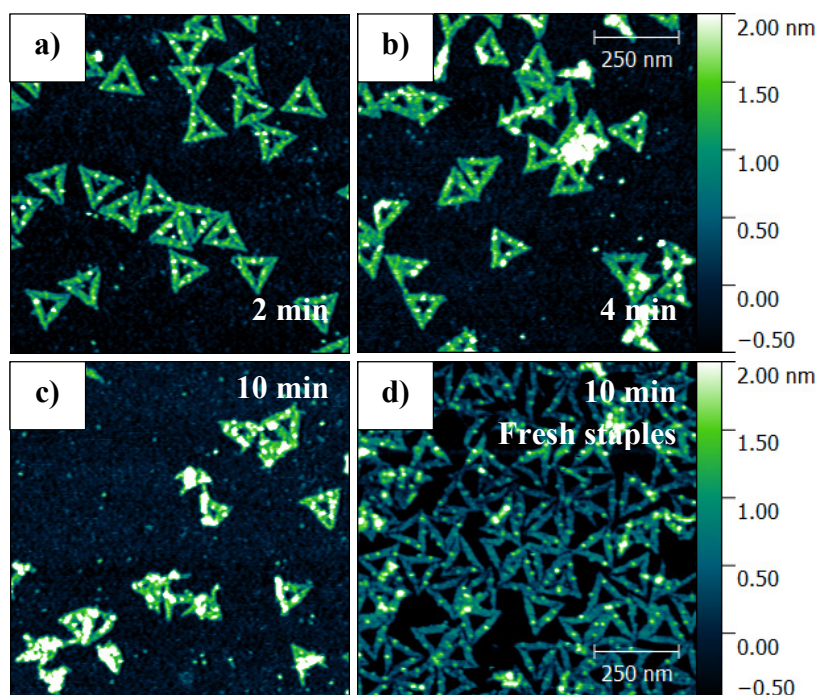


Figure 32. AFM images of DNA origami prepared with aged staple strands, incubated for a) 2 minutes, b) 4 minutes and c) 10 minutes. For comparison d) shows DNA origami prepared with fresh staple strands, incubated with SA<sub>v</sub> for 10 minutes (image size 1 x 1  $\mu\text{m}^2$ , height scale -0.5 to 2.0 nm).

The optimized protocol for sample preparation described in the beginning of this chapter leads in general to samples with reproducibly high quality. The statistical analysis is reliable with an average error of the strand break cross section below ten percent. In some cases, sample preparation of single samples failed due to contamination of the silicon, disturbing the DNA origami immobilization, or remaining salt residues. In addition, some samples had no or only few SAV on the DNA origami, possibly caused by SAV denaturation and subsequent loss by rinsing (Figure 33.a). This may happen to a complete sample series or just single samples. Although less often encountered, salt residues may remain on the surface and disturb the AFM imaging. Two different situations occurred in the experiments. In some cases, the DNA origami were still clearly visible (Figure 33.b) and could be analyzed. In other samples, the DNA origami were sometimes covered by salt, making a statistical analysis impossible (Figure 33.c). Finally, if the sample after SAV incubation was not rinsed thoroughly enough, the amount of remaining non-specifically bound protein would be too high for statistical analysis (Figure 33.d).

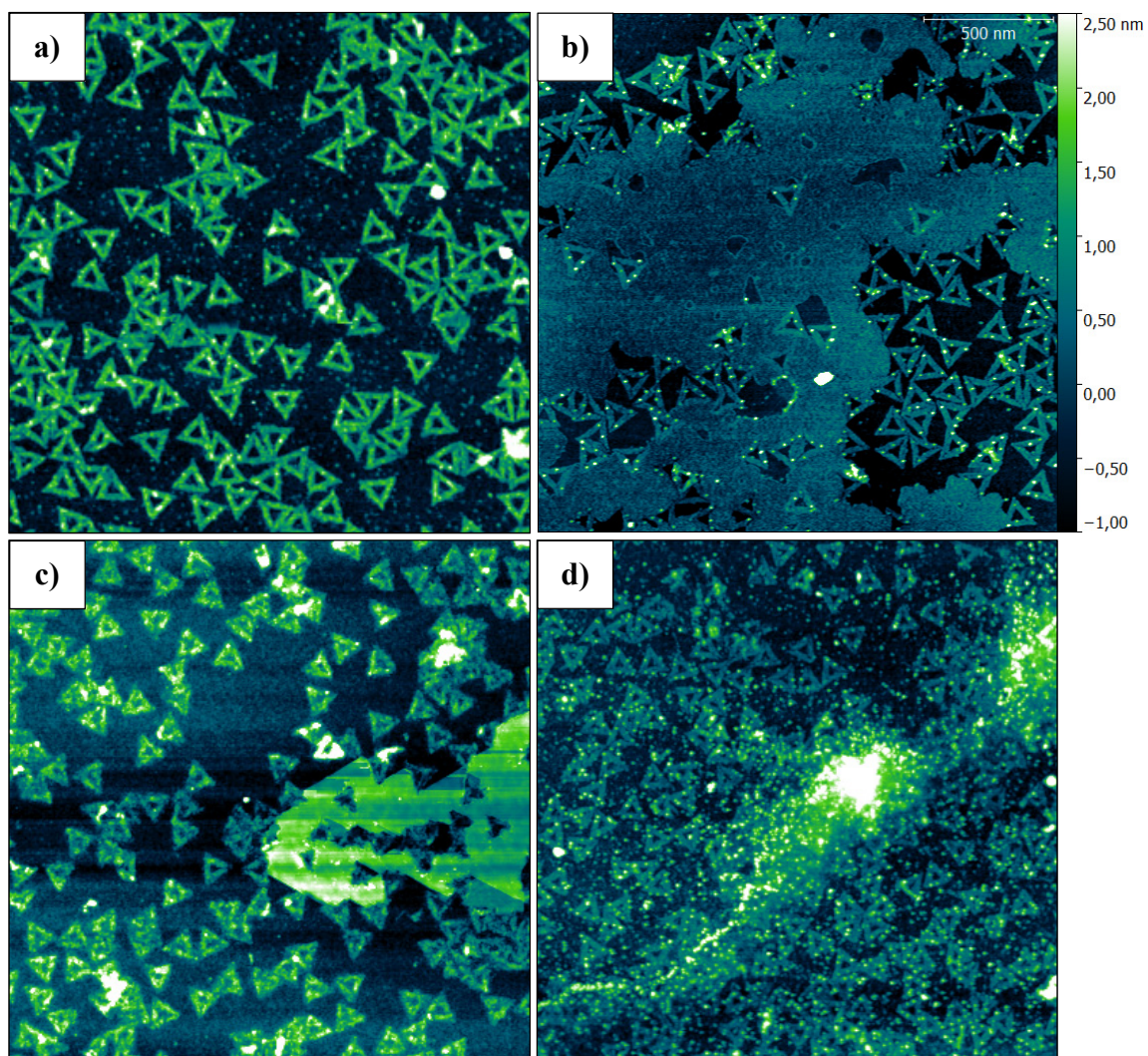


Figure 33. AFM images of samples with a) missing SA v, b) clearly visible origami between salt remaining, c) covered origami and d) SA v remaining on the surface (image size  $2 \times 2 \mu\text{m}^2$ , height scale -1.0 to 2.5 nm).

### 3.6. Two methods to determine absolute strand break cross sections

#### 3.6.1. Absolute Method

The absolute method is the typical method to determine the absolute strand break cross section for certain sequences at desired LEE energies. Two different sequences are positioned on one DNA origami design. From AFM analysis, the number of strand breaks  $N_{SB}$  is determined as a function of the fluence  $F$ .

$$N_{SB} = \sigma \cdot F + N_{SB0} \quad (03)$$

At low fluences, the dose response curve is linear.<sup>12</sup> Thus, the absolute strand break cross section can be obtained from the instrumental weighted linear fit to the data (Figure 34). The resulting strand break cross section  $\sigma$  is defined as

$$\sigma = (N_{SB} - N_{SB0})/F$$

with the number of strand breaks  $N_{SB}$ , the number of strand breaks without irradiation  $N_{SB0}$ , and the fluence  $F$ .

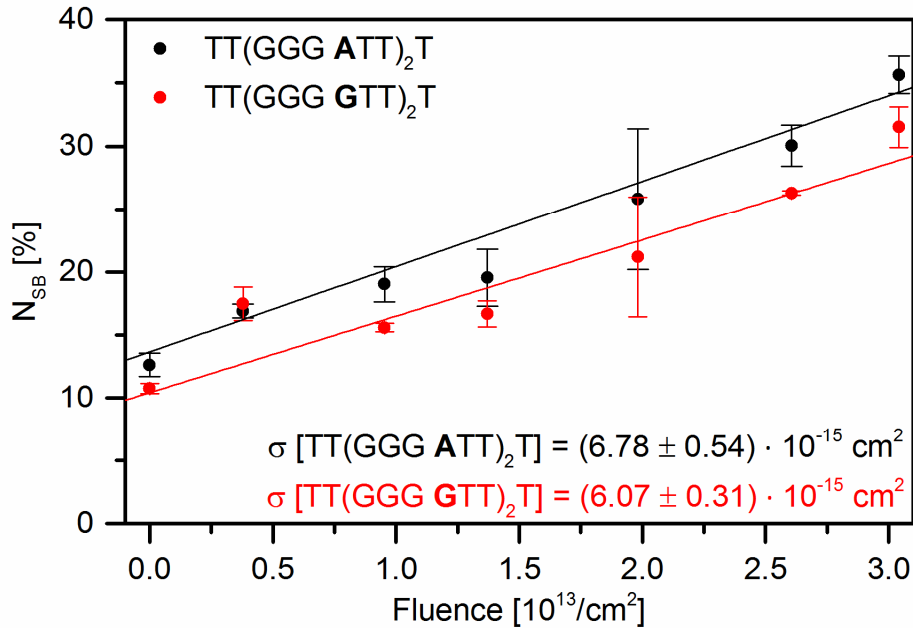


Figure 34. Number of SSB as a function of the fluence for two sequences Telo2 and Telo2G at 10 eV. The figure represents the graphical interpretation of the absolute method, with the strand break cross section obtained from the linear fits.

At higher fluences a saturation of  $N_{SB}$  is generally observed.<sup>12,46</sup> This effect probably results from slow charge accumulation within the Si/SiO<sub>2</sub> surface or the DNA origami structure, which finally leads to electron repulsion.<sup>25</sup> Therefore, all experiments were made at low fluence values to avoid saturation.

In one experiment the strand break cross sections of at least two different sequences can be obtained. A fluence dependency needs to be recorded, thus at least two different sample series need to be irradiated under identical conditions to proof repeatability. The total amount of samples irradiated with different fluence values has to be at least ten samples to improve the accuracy of the determined absolute strand break cross sections. Therefore, the additional relative method was developed.

### 3.6.2. *Relative Method*

The relative method was developed to reduce the amount of samples which need to be irradiated to determine the strand break cross section for a sequence. A sequence with known  $\sigma_{SSB}$  at a certain energy is used as an internal reference. In combination with the reference sequence, the strand break cross section for an unknown sequence is determined. Both sequences are placed on one DNA origami and thus irradiated under identical conditions. The fluence is therefore identical for both sequences.

$$(N_{SB} - N_{SB0})/\sigma = F = (N_{SB} - N_{SB0})_{ref}/\sigma_{ref}$$

The unknown strand break cross section  $\sigma$  can then be calculated based on the reference strand break cross section  $\sigma_{ref}$ .

$$\sigma = \sigma_{ref} \cdot (N_{SB} - N_{SB0})/(N_{SB} - N_{SB0})_{ref} = \sigma_{ref} \cdot E$$

with  $E = (N_{SB} - N_{SB0})/(N_{SB} - N_{SB0})_{ref}$ .

The ratio  $E$  between both strand break cross sections was obtained graphically (Figure 35). Within this plot,  $E$  is represented as the slope of the instrumentally weighted linear fit. For this method, rather few samples are needed. For repeatability, at least three samples were irradiated. This method is independent of the fluence, as long as all irradiations are performed in the linear response regime. Thus, all samples were irradiated with rather short times at low current. At very short irradiation times, the  $N_{SB}$  is very similar to  $N_{SB0}$ , resulting in stronger variations for  $E$ . Therefore it is advisable for further experiments to irradiate the samples with different fluence values. Over all experiments, the error of  $E$  is quite small. Yet this error accumulates with the error of the reference

strand break cross section  $\sigma_{ref}$ . Thus, it is advisable to use the absolute method to determine absolute strand break cross sections with an error around 10%. Then, the less time consuming relative method can be used for further strand break cross section determination for a variety of sequences.

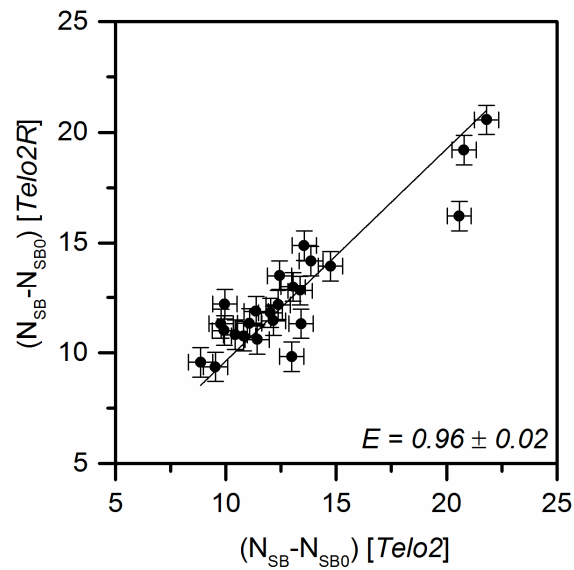


Figure 35. Graphical correlation of the LEE induced strand break damage between the known Telo2 sequence and the unknown Telo2R sequence, to determine the ratio E from the slope of the linear fit.

### 3.7. Biotin label for oligonucleotide visualization

The protruding end of each target oligonucleotide strand was labelled with a Bt molecule. Since Bt is irradiated just like the oligonucleotide sequences, its stability towards 10 eV electrons over the analyzed fluence range needs to be confirmed. Therefore only Bt was irradiated within the sequences 5'-Bt-t-1s4i-3', -t-1s14i and -t-1s24i on the DNA origami triangle (together with Telo3 at corner positions, see chapter 5, table 3). Two series, each containing six irradiated and two non-irradiated samples have been exposed to electrons at currents between 3.5 - 7.5 nA. The AFM images were taken in the central area with beam profile 2. Samples which were exposed to the same fluence have been combined to one point in the graph. With a damage cross section of  $(0.26 \pm 0.92) \cdot 10^{-15} \text{ cm}^2$  Bt remains stable; within the margin of error no detectable fragmentation at 10 eV up to a fluence of at least  $10^{13} \text{ cm}^{-2}$  (Figure 36).

Previous DEA experiments revealed the formation of a series of fragment anions from Bt at energies below 10 eV.<sup>129</sup> Additionally to the DEA experiments, the authors presented an absolute damage cross section of  $(1.1 \pm 0.2) \cdot 10^{-14} \text{ cm}^2$  for Bt when irradiated with 18 eV.<sup>129</sup> Comparing those previous results and the results obtained during this work, the Bt damage needs to be considered in dependence of the electron energy. While at 10 eV Bt is hardly influenced at all, at higher energies where ionization takes place, the fragmentation needs to be considered.

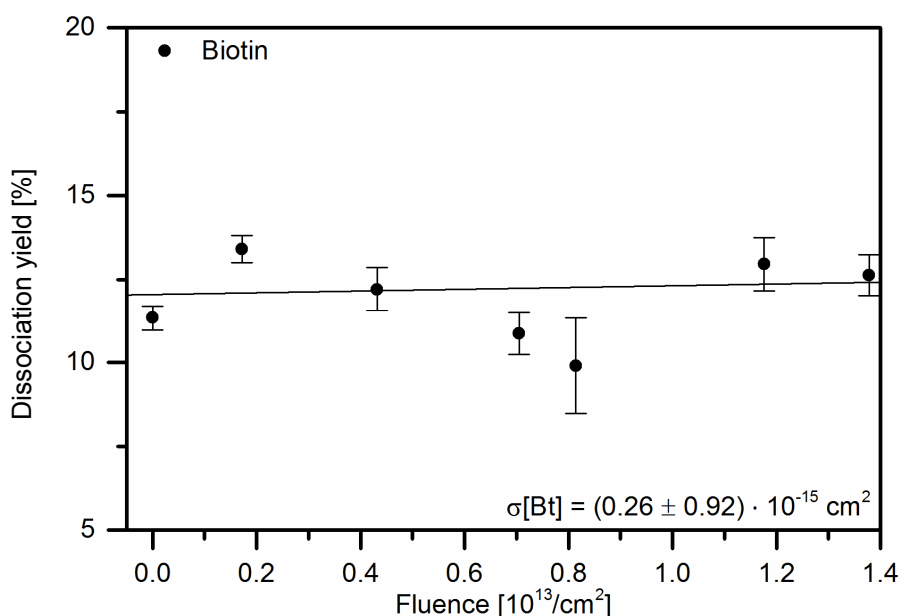


Figure 36. Fluence dependence of  $N_{SB}$  for Bt at 10 eV.

## 4. Radiosensitizers – nucleobases modified with fluorine

### 4.1. 2-Fluoroadenine ( $^{2F}A$ )

#### 4.1.1. Fragmentation behavior

The fluor modified subunit of the radiosensitizer *Fludarabine* is  $^{2F}A$ . To investigate the fragmentation behavior of the modified nucleobase (purchased from *Sigma Aldrich*, 96 % purity) in comparison to the natural nucleobase A (Figure 37), a classical gas phase DEA experiment was carried out for the fluorinated nucleobase (see chapter 2.6.1) at the University of Siedlce together with Dr. Janina Kopyra. In a ultra-high vacuum chamber with a base pressure of  $10^{-9}$  mbar a crossed electron/molecular beam generates TNIs at certain resonance energies, which then create fragment anions (Figure 38). The quasi-monoenergetic electron beam is generated by a trochoidal electron monochromator with a resolution of  $242.8 \pm 2.8$  meV FWHM and an electron current of  $\sim 10$  nA. The electron energy scale was calibrated with the electron scavenger  $SF_6$ , which generates  $SF_6^-$  anions near 0 eV. The calibration was done after each series of measurements.  $^{2F}A$  was thermally evaporated at 190 - 200 °C without decomposition. An ionization gauge detected a pressure of the molecules in the gas phase of  $3 - 5 \cdot 10^{-7}$  mbar. The anions created by collisions with electrons are mass analyzed with a QMS. The amount of anion fragments at certain masses were recorded as a function of the electron energy within a range of 0 – 12 eV.

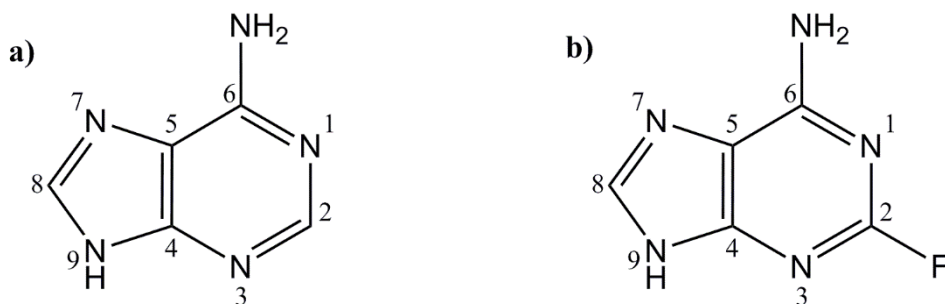


Figure 37. Chemical structures of **a)** adenine and **b)** 2-fluoroadenine.

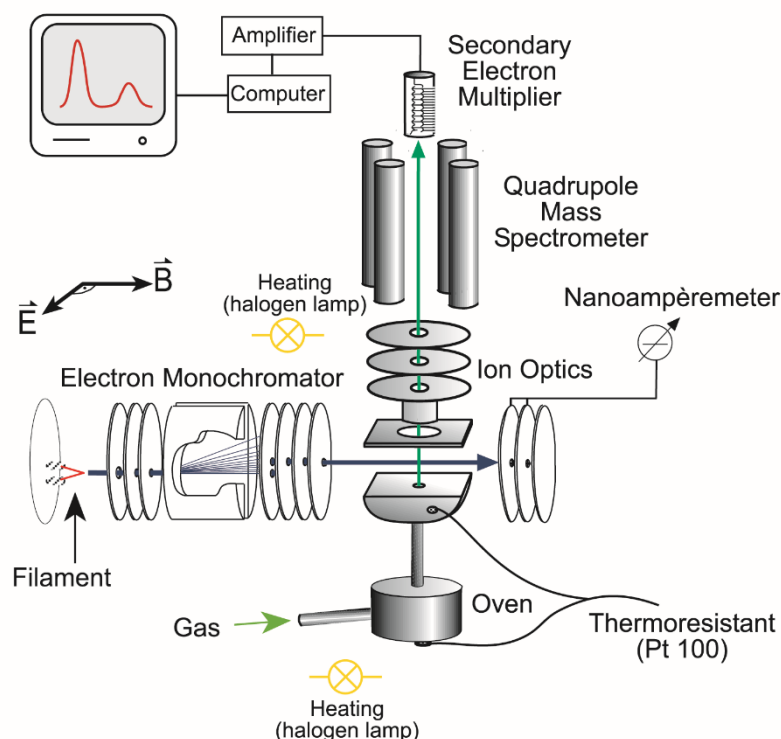
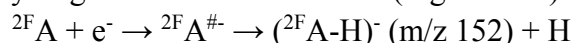


Figure 38. Schematic drawing of the experimental setup for the DEA experiments in the gas phase, with crossed electron and molecule beam.

The most intense signal was obtained for a fragment of  $m/z$  152, which corresponds to the dehydrogenated molecular anion (Figure 39.a):



The broad signal from 0.3 eV to 3.5 eV is a combination of at least three DEA resonances at 0.8 eV, 1.3 eV, and 2.0 eV. Up to an electron energy of 4 eV the extra electron typically occupies a formerly unoccupied MO. The initial electron configuration is not altered by this attachment. The potential energy curves of those MOs are usually repulsive. Therefore the electron must be captured in a metastable state by a centrifugal energy barrier ( ${}^2\text{F}\text{A}^{\#-}$ ). Those resonances are referred to as single particle shape resonances.<sup>49,50</sup> For A the same resonances could be obtained at 0.72 eV and 0.84 eV with weak, narrow signals, and at 1.07 eV, 1.4 eV and 2.2 eV with weak, broad signals.<sup>18,134</sup> Former studies with different methylated adenine derivatives assigned the signal below 1.5 eV to the loss of H at 9-N, with 0.72 eV, 0.84 eV and 1.07 eV as vibrational Feshbach resonances

(VFRs), and 1.4 eV as  $\pi^*$  resonances.<sup>135</sup> For 2-chloroadenine a dehydrogenated parent anion ( $^{2\text{Cl}}\text{A-H}^-$ ) could be detected with signals at 0.8 eV, 1.1 eV and 1.8 eV.<sup>136</sup> Here, the signals above 1 eV were assigned to  $\pi^*$  resonances, while the signal at 0.8 eV was suggested to be a contribution from VFR and  $\pi^*/\sigma_{\text{NH}^*}$ . Taking those results from A,  $^{\text{xMe}}\text{A}$  and  $^{2\text{Cl}}\text{A}$  into account, the ( $^{2\text{F}}\text{A-H}^-$ ) signal at 0.8 eV is assigned to a VFR, while the signals at 1.29 eV and 2.0 eV are assigned to  $\pi^*$  resonances. In comparison with the natural nucleobase the signals from  $^{2\text{F}}\text{A}$  are slightly shifted towards lower energies due to the presence of the fluorine atom. This shift occurs in  $^{2\text{Cl}}\text{A}$  as well, yet even stronger.<sup>136</sup> The dehydrogenation in  $^{2\text{F}}\text{A}$  can occur at 9-N or the  $\text{NH}_2$  group at 6-C (Figure 37.b). Based on earlier studies with methylated A<sup>135</sup> and recent *ab initio* calculations the signals below 2.0 eV are assigned to the 9-N-H bond.<sup>137</sup>

At  $m/z$  133 and 132 two fragments were detected, both with a broad resonance at 5.5 eV (Figure 39.b, c). Additionally the fragment at  $m/z$  132 appeared with lower intensity also at 10 eV. Those fragment anions are assigned to ( $^{2\text{F}}\text{A-H-F}^-$ ) and ( $^{2\text{F}}\text{A-2H-F}^-$ ), formed by the loss of the F atom and one or two H atoms. The very same fragments could be obtained for A at 7.0 eV and 10.5 eV for the loss of 2 H, and 6.5 eV and 10.9 eV for the loss of 3 H atoms.

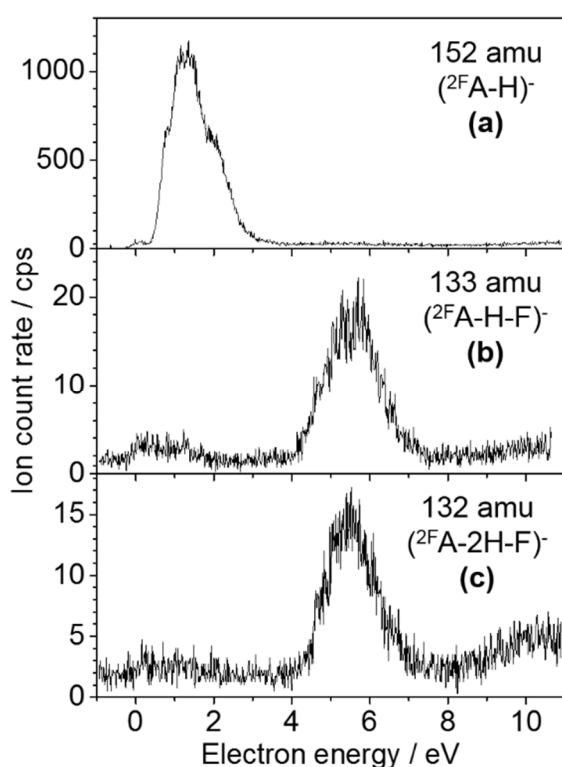


Figure 39. Ion count rate for fragment anions detected at  $m/z$  152, 133 and 132 resulting from DEA to  $^{2\text{F}}\text{A}$ .

Like in the ( $^{2\text{F}}\text{A-H}^-$ ) fragment, the presence of the F atom shifts the resonance energies towards lower energies compared to A.<sup>18,134</sup> The ratio between the two signals for the  $m/z$  132 anion fragment is inverted for  $^{2\text{F}}\text{A}$  compared to A, from a high intensity at 10.9 eV to 5.5 eV in the fluorinated nucleobase. In any case the signals are assigned to core excited resonances.

The formation of the  $m/z$  133 and 132 fragment can be accompanied by HF formation. The bond dissociation energy of the HF bond is quite high, therefore it can thermodynamically drive the reaction. In previous studies

the formation of neutral halogen acids was already observed to trigger the formation of certain anion fragments in halo-nucleobases, especially reported for the modified nucleobases 2-chloroadenine, 5-chlorouracil and 6-chlorouracil.<sup>136,138</sup> On the other hand, modified nucleobases with bromine are not known to create HBr, since the bond dissociation energy is strongly decreased, from 5.9 eV (HF) to 4.5 eV (HCl) to 3.8 eV (HBr). This is documented for 5-bromouracil (<sup>5</sup>BrU) and its anion fragment (<sup>5</sup>BrU-Br)<sup>-</sup>, generated after losing bromine.<sup>78</sup>

For <sup>2</sup>F A the loss of 2 H and 3 H atoms without losing the F atom could not be detected. This indicates, that the H atom loss in A at 2-C is involved in the formation of its anion fragments m/z 133 and 132.

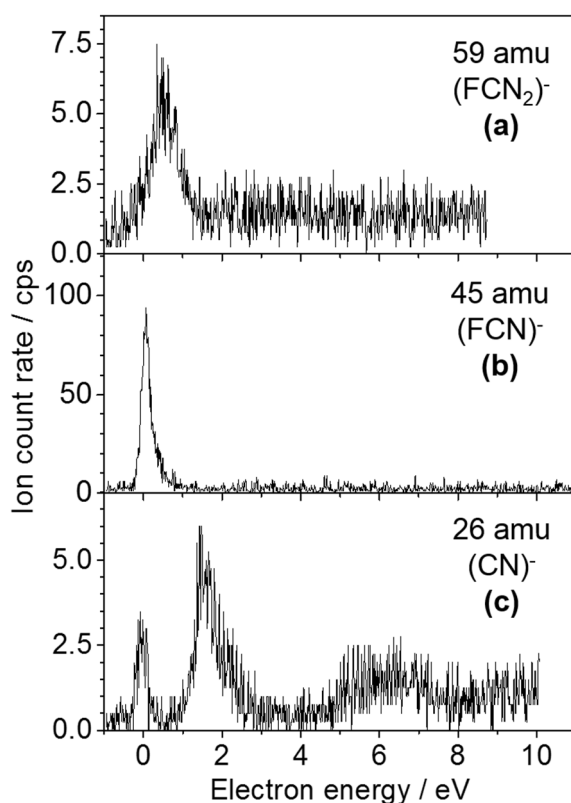


Figure 40. Ion count rate for fragment anions detected at m/z 59, 45 and 26 resulting from DEA to <sup>2</sup>F A.

In addition to the reduced parent fragments, anions with lower mass were formed by cleavage of the aromatic ring system in <sup>2</sup>F A. The heaviest of those fragments is FCN<sub>2</sub><sup>-</sup> with m/z 59 and a weak resonance peaking at 0.55 eV (Figure 40.a). On a competitive channel the smaller fragment FCN<sup>-</sup> with m/z 45 is generated with a rather intense resonance signal at 0.07 eV (Figure 40.b). Since both signals appear close to 0 eV the electron affinity of the respective neutrals is high enough to compensate the cleavage of the aromatic ring system. These fragmentation reactions might be thermodynamically possible due to bond formations within the neutral fragments. Such low-energy multiple bond breaking reactions triggered by electron attachment are well-known for other molecules, such as monosaccharides,<sup>139</sup> nucleotide surrogates,<sup>16</sup> and others.<sup>47</sup> In <sup>2</sup>F A these rather complex ring cleavages are observed at low energies, which are associated with VFRs.

The smallest of all detectable anion fragments was the  $\text{CN}^-$  ion with a clear maximum at 1.61 eV formed by a  $\pi^*$  resonance, and a broad yet weak signal around 6.3 eV (Figure 40.c). The signal close to 0 eV is assigned to hot band transitions, occurring through vibrational excited  ${}^2\text{F}_A$  molecules. In previous experiments with A performed with the same experimental setup the formation of the  $\text{CN}^-$  fragment was reported with signals at 6 eV and 1.8 eV with inverted relative intensities between both signals.<sup>134</sup> The Innsbruck group observed exclusively the two core excited resonance at 6 eV and additionally another signal above 10 eV.<sup>18</sup>

#### 4.1.2. Strand breaks in modified oligonucleotides

${}^2\text{F}_A$  was implemented into the oligonucleotide sequences 5'-Bt-d(TT( ${}^2\text{F}_A\text{T}{}^2\text{F}_A$ )<sub>3</sub>TT)-3' and attached to the DNA origami triangle at central positions 5'-t1s8i, 5'-t1s18i, and 5'-t1s28i. To compare the sensitivity of the fluorinated oligonucleotide towards LEEs to the unmodified natural oligonucleotide, the sequence 5'-Bt-d(TT(ATA)<sub>3</sub>TT)-3' was attached to the same DNA origami design at corner positions 5'-t7s8g, 5'-t7s18g, and 5'-t7s28g. Three series of samples, each consisting of six irradiated and two non-irradiated samples, one on the sample stage and one outside the vacuum chamber, were irradiated and analyzed. The current during the irradiation process varied from 4 – 6 nA over all three series. Samples with similar fluence were combined for graphical analysis (Figure 41).

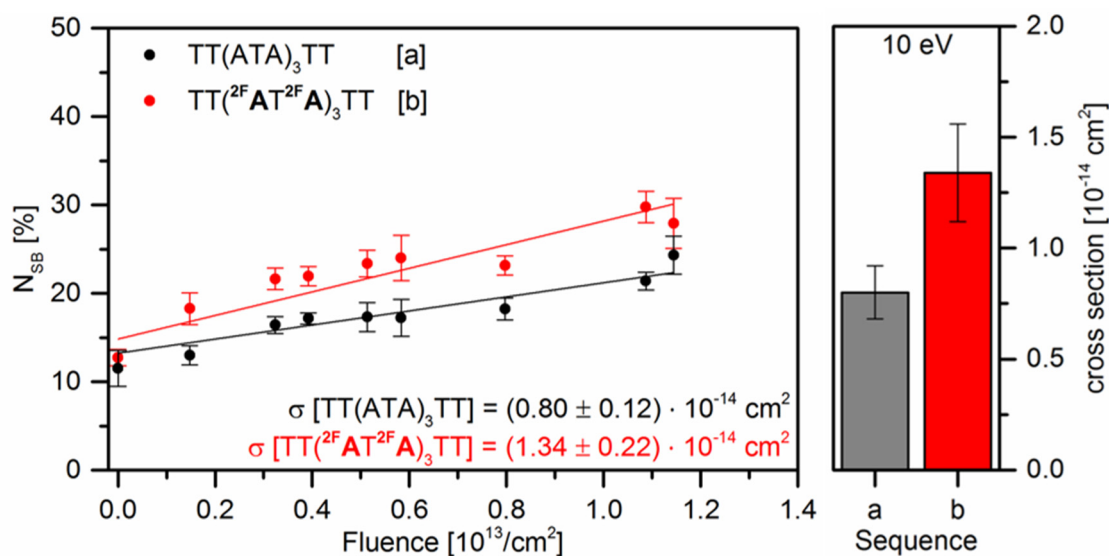


Figure 41. Fluence dependence of A (black, a) and  ${}^2\text{F}_A$  (red, b) containing oligonucleotides at 10 eV (left) and resulting absolute strand break cross sections (right).

The markers on the sample surface differed from the ones later used. Here, diagonal lines from the corner with endings at 1.0 mm from the center were scratched into the surface, instead of the crosshairs in the center. Therefore, the fluence calculation was made for area B (see chapter 3.3, table 1) from the beam profile 1. This area was irradiated with 4.16 % of the total measured current.

From the slope of the linear fit of the fluence dependence the absolute strand break cross section for 5'-Bt-d(TT(ATA)<sub>3</sub>TT)-3' was obtained as  $(0.80 \pm 0.12) \cdot 10^{-14} \text{ cm}^2$  (Figure 41). The modified nucleobase <sup>2</sup>F A increased the sensitivity of the oligonucleotide towards 10 eV electrons to  $(1.34 \pm 0.22) \cdot 10^{-14} \text{ cm}^2$ , corresponding to an enhancement factor *EF* of  $1.7 \pm 0.5$ .

Although the condensed phase experiment showed the enhancing effect of <sup>2</sup>F A, only a weak resonance of the molecule was observed in the gas phase at 10 eV. Therefore the condensed phase experiment has been repeated at an energy at which a strong resonance in the molecule was detected. With the current experimental setup a reliable beam with 5 eV electrons can be generated without strong beam scattering. Thus, the resonances generating the (<sup>2</sup>F A-F-H)<sup>-</sup> and (<sup>2</sup>F A-F-2H)<sup>-</sup> fragments at 5.5 eV have been chosen. The same DNA origami design with 5'-Bt-d(TT(ATA)<sub>3</sub>TT)-3' and 5'-Bt-d(TT(<sup>2</sup>F AT<sup>2</sup>F A)<sub>3</sub>TT)-3' was used and irradiated with currents of 2.6 - 2.8 nA in one series of six irradiated and two non-irradiated samples (beam profile 3).

At 5.5 eV, both absolute strand break cross sections containing A and <sup>2</sup>F A are enhanced (Figure 42). For 5'-Bt-d(TT(ATA)<sub>3</sub>TT)-3' and 5'-Bt-d(TT(<sup>2</sup>F AT<sup>2</sup>F A)<sub>3</sub>TT)-3' a strand break cross section of  $(1.36 \pm 0.02)$  and  $(2.12 \pm 0.09) \cdot 10^{-14} \text{ cm}^2$  was obtained, respectively. The *EF* of [b] compared to [a] is  $(1.6 \pm 0.1)$ . The smaller error in these experiments is due to an optimized sample preparation. Compared to the results for 10 eV, both oligonucleotides are equally more sensitive towards LEEs with 5.5 eV and <sup>2</sup>F A enhances the sensitivity by a constant *EF* at both energies (Figure 42.right).

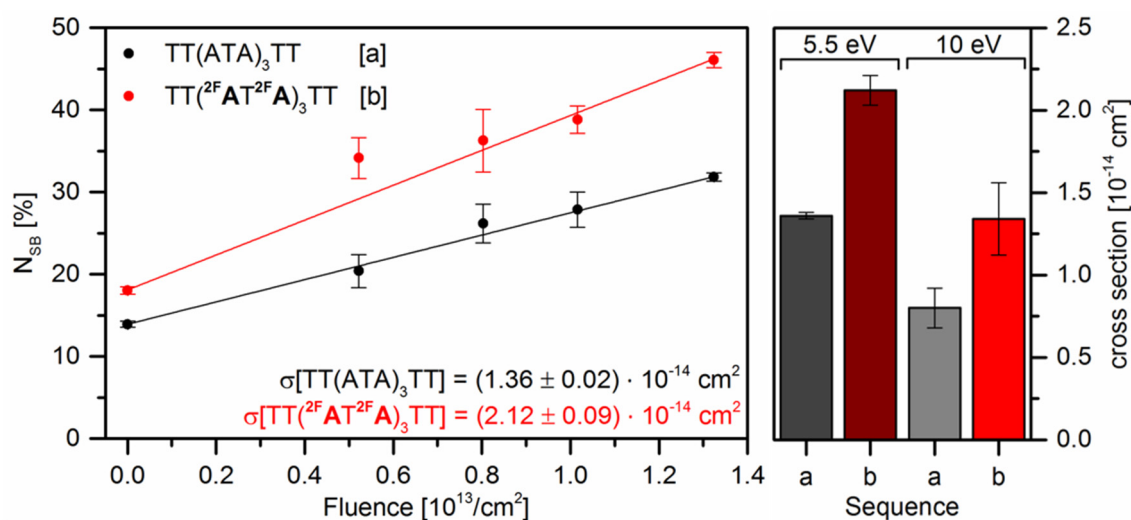


Figure 42. Fluence dependence of A (black, a) and  $^{2F}$ A (red, b) containing oligonucleotides at 5.5 eV (left) and comparison of the absolute strand break cross sections of both sequences at 5.5 eV and 10 eV (right).

## 4.2. 5-Fluoruracil

### 4.2.1. Fragmentation behavior

The radiosensitizer  $^5\text{F}\text{U}$  is a fluorinated derivative of U and T (Figure 43).

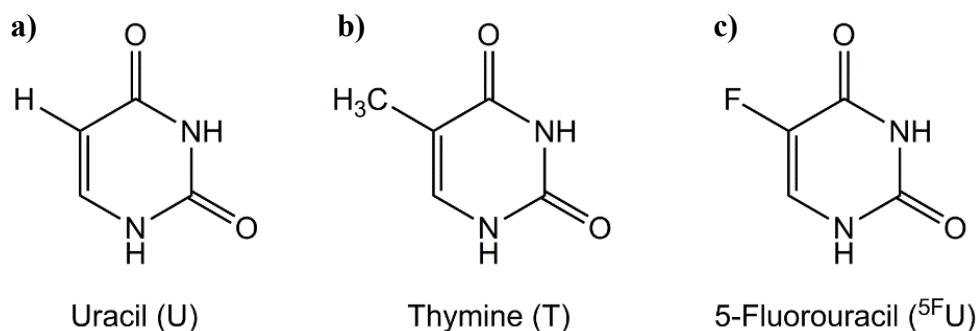
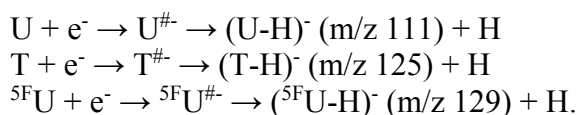


Figure 43. Chemical structures of **a)** the RNA nucleobase uracil, **b)** the DNA nucleobase thymine and **c)** the radiosensitizer 5-fluorouracil ( $^5\text{F}\text{U}$ ).

For the pyrimidine nucleobases U and T, as well as for different halo-uracils, detailed DEA studies in the energy range of 0 – 3 eV revealed several significant peaks for all substances.<sup>138,140,141</sup> Below 3 eV, the most abundant fragment for all mentioned nucleobases is the parent anion after hydrogen loss, formed through a VFR:



For U, the fragment  $(\text{U-H})^-$  is formed at 0.64 eV for the 1-N hydrogen loss, and at 0.95 eV for the 3-N site. Two broad signals appear at 1.4 eV and 1.7 eV, formed by additional  $\pi^*$  resonances. The  $(\text{T-H})^-$  resonances are very similar to  $(\text{U-H})^-$ , only with an additional small peak at 0.82 eV.<sup>141</sup>

The influence of the fluorine substitute changes the resonances of the  $(^5\text{F}\text{U-H})^-$  fragment, which appear only above 0.5 eV (0.56, 0.85, 1.28 and 1.5 eV), while the non-fluorinated derivatives show peaks below 0.5 eV. On the other hand, for  $^5\text{F}\text{U}$  an additional fragment  $(^5\text{F}\text{U-HF})^-$  was observed with three peaks below 0.6 eV (0.07, 0.24, 0.41 and 0.58 eV).<sup>141</sup> Furthermore, the nucleobases U and T were studied at energies above 3 eV with the focus on site selective hydrogen loss.<sup>142</sup> Bond and site selective resonances between 5 eV and 12 eV were observed within broad signals.<sup>143</sup>

In DEA to  ${}^5\text{F}^{\text{U}}$  neither the  $\text{F}^-$  nor the  $(\text{U-F})^-$  fragment could be observed.<sup>79</sup> This result correlates with the fragmentation behavior of  ${}^2\text{F}^{\text{A}}$ . The fragments  $\text{FCN}^-$  and  $\text{FCN}_2^-$  occurring in  ${}^2\text{F}^{\text{A}}$  were not observed in  ${}^5\text{F}^{\text{U}}$  by the authors.<sup>79</sup> The  $\text{CN}^-$  fragment on the other hand, was generated from  ${}^5\text{F}^{\text{U}}$  with an intense signal at 7.0 eV and additional weak resonances at 4.3 eV and 11.0 eV. Furthermore, the fragments  $\text{OCN}^-$ ,  $\text{CN}_2\text{OH}^-$  and  $\text{H}_2\text{C}_3\text{NO}^-$  were generated from  ${}^5\text{F}^{\text{U}}$  at around 5 eV.<sup>79</sup> As in  ${}^2\text{F}^{\text{A}}$ , no intense resonance appears around 10 eV.

#### 4.2.2. Strand breaks in modified oligonucleotides

${}^5\text{F}^{\text{U}}$  was analyzed with the relative method (see chapter 3.6) at 10 eV. Since it is a fluorinated derivative of the nucleobase T, the sequence 5'-Bt-d(TT(A ${}^5\text{F}^{\text{U}}$ UA)<sub>3</sub>TT)-3' was measured together with the T containing 5'-Bt-d(TT(ATA)<sub>3</sub>TT)-3' sequence. The DNA origami design was similar to the  ${}^2\text{F}^{\text{A}}$ /A experiment, with the F-modified oligonucleotide being attached to the DNA origami triangle at the central positions and the T containing sequence at the corner positions. Six samples were irradiated for 20 seconds with a current of 3 – 8 nA each. Two non-irradiated samples, one in the vacuum, one outside, were analyzed and averaged to yield a mean value of  $N_{\text{SB0}} \pm$  standard error. Three out of six irradiated samples could be analyzed and eight AFM images of each sample have been recorded. For each image the  $\Delta N_{\text{SB}}$  values of both sequences have been determined. The ratio  $E$  between the sequence containing  ${}^5\text{F}^{\text{U}}$  and the known reference sequence was obtained from all  $\Delta N_{\text{SB}}$  values as  $E = 1.50 \pm 0.07$  (Figure 44.a). This ratio was then multiplied with the absolute strand break cross section of the 5'-Bt-d(TT(ATA)<sub>3</sub>TT)-3' sequence of  $(0.80 \pm 0.12) \cdot 10^{-14} \text{ cm}^2$ , resulting in a strand break cross section of  $(1.20 \pm 0.20) \cdot 10^{-14} \text{ cm}^2$  for the 5'-Bt-d(TT(A ${}^5\text{F}^{\text{U}}$ UA)<sub>3</sub>TT)-3' sequence.

To compare the radiosensitizing effect of both  ${}^5\text{F}^{\text{U}}$  and  ${}^2\text{F}^{\text{A}}$ , the nucleotide sequence of 5'-Bt-d(TT( ${}^2\text{F}^{\text{A}}$ T ${}^2\text{F}^{\text{A}}$ )<sub>3</sub>TT)-3' at the center positions of the DNA origami triangle was combined with the  ${}^5\text{F}^{\text{U}}$  containing sequence 5'-Bt-d(TT( ${}^5\text{F}^{\text{U}}$ UT ${}^5\text{F}^{\text{U}}$ )<sub>3</sub>TT)-3' at the corner positions. In both sequences the amount of F containing nucleobases is identical with each modified nucleobase being flanked by T. Six samples were irradiated for 20 seconds with a current of 4 – 9 nA each. Two samples could be analyzed and eight images of each sample have been taken. Another series of six samples was irradiated for 60 seconds each, of which four samples could be analyzed. The combined data of both experiments yield a ratio  $E = 0.98 \pm 0.03$ , resulting in an absolute strand break cross section of

$(1.31 \pm 0.25) \cdot 10^{-14} \text{ cm}^2$  for 5'-Bt-d(TT( $^{5F}$ UT $^{5F}$ U) $_3$ TT)-3', based on the strand break cross section of 5'-Bt-d(TT( $^{2F}$ AT $^{2F}$ A) $_3$ TT)-3' of  $(1.34 \pm 0.22) \cdot 10^{-14} \text{ cm}^2$  (Figure 44.c).

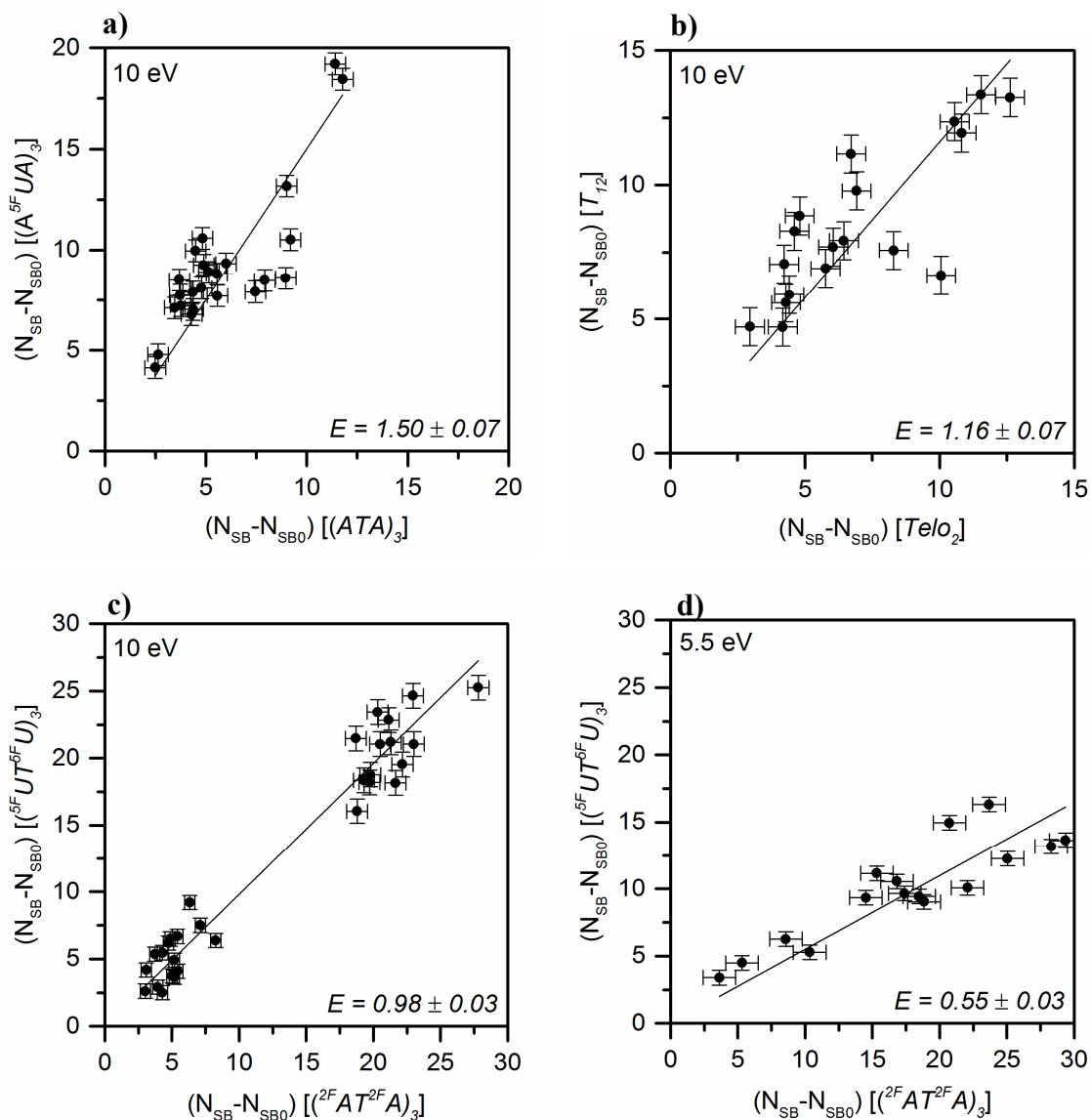


Figure 44. Correlation between  $\Delta N_{SB}$  values of the sequences 5'-Bt-d(TT $X$ TT)-3', with  $X =$  **a)**  $(A^{5F}UA)_3$  and  $(ATA)_3$ , **b)**  $T_8^*$  and **c)**  $(^{5F}UT^{5F}U)_3$  and  $(^{2F}AT^{2F}A)_3$  at 10 eV. **d)** Correlation between  $\Delta N_{SB}$  values of  $X = (^{5F}UT^{5F}U)_3$  and  $X = (^{2F}AT^{2F}A)_3$  at 5.5 eV. The x-axis corresponds to the reference sequences. The ratios  $E$  have been obtained from the slopes of the linear fits. \* $T_8$  is measured relative to Telo2 (see chapter 5).

Since  ${}^5\text{F}\text{U}$  is a thymine derivative, the homooligonucleotide  $5'\text{-Bt-d(T)}_{12}\text{-}3'$  was analyzed as well at 10 eV with the relative method. A series of six samples was irradiated for 20 seconds with a current of 2 – 4 nA each. The ratio  $E = (1.16 \pm 0.07)$  was obtained from the slope of the linear fit to the data (Figure 44.b). Based on the strand break cross section  $\sigma = (0.68 \pm 0.05) \cdot 10^{-14} \text{ cm}^2$  for Telo2 (see chapter 5), the strand break cross section for  $5'\text{-Bt-d(T)}_{12}\text{-}3'$  was determined to be  $(0.79 \pm 0.07) \cdot 10^{-14} \text{ cm}^2$ .

The same DNA origami design with oligonucleotides containing  ${}^5\text{F}\text{U}$  and  ${}^2\text{F}\text{A}$  was also irradiated with 5.5 eV energy, and analyzed with the relative method. Six samples were irradiated for 20 seconds with a current of 2 – 3 nA each. Four samples could be analyzed and four AFM images of each sample have been recorded. Based on the strand break cross section of  $5'\text{-Bt-d(TT}({}^2\text{FAT}{}^2\text{FA})_3\text{TT})\text{-}3'$  of  $(2.12 \pm 0.09) \cdot 10^{-14} \text{ cm}^2$  and a ratio  $E = 0.55 \pm 0.03$  the absolute strand break cross section of  $5'\text{-Bt-d(TT}({}^5\text{FUT}{}^5\text{FU})_3\text{TT})\text{-}3'$  was determined to be  $(1.17 \pm 0.11) \cdot 10^{-14} \text{ cm}^2$  (Figure 44.d).

At 10 eV the absolute strand break cross section of  $5'\text{-Bt-d(TT}(\text{A}{}^5\text{FUA})_3\text{TT})\text{-}3'$  is  $(1.20 \pm 0.20) \cdot 10^{-14} \text{ cm}^2$  and thus only slightly below the strand break cross section of  $5'\text{-Bt-d(TT}({}^5\text{FUT}{}^5\text{FU})_3\text{TT})\text{-}3'$ , which is  $(1.31 \pm 0.25) \cdot 10^{-14} \text{ cm}^2$ . Both strand break cross sections are identical within the margin of error. Thus, the sensitivity towards electrons of 10 eV energy is independent of the amount of  ${}^5\text{F}\text{U}$  in the oligonucleotide and the neighboring nucleobases A or T in the oligonucleotide sequence. The latter observation is also supported by the comparison of  $5'\text{-Bt-d(TT}(\text{ATA})_3\text{TT})\text{-}3'$  and  $5'\text{-Bt-d(T)}_{12}\text{-}3'$ . Within the margin of error, both sequences have identical strand break cross sections of  $(0.80 \pm 0.12)$  and  $(0.79 \pm 0.07) \cdot 10^{-14} \text{ cm}^2$ , respectively. However, both aspects, the neighboring nucleobase A or T and the amount of  ${}^5\text{F}\text{U}$  in the sequence (either 3 or 6 times), can have an opposite influence on the sensitivity of the sequence, resulting in an identical strand break cross section for both sequences  $5'\text{-Bt-d(TT}(\text{A}{}^5\text{FUA})_3\text{TT})\text{-}3'$  and  $5'\text{-Bt-d(TT}({}^5\text{FUT}{}^5\text{FU})_3\text{TT})\text{-}3'$ . Although it is rather unlikely that these two very different aspects influence the strand break cross section with similar intensity in opposite directions, it is not utterly out of question.

Comparing energies of 5.5 eV and 10 eV, no change in the strand break cross section of  $5'\text{-Bt-d(TT}({}^5\text{FUT}{}^5\text{FU})_3\text{TT})\text{-}3'$  was observed. The ratio of the respective strand break cross sections was calculated to be  $0.9 \pm 0.2$ . Thus, although significant resonances were observed for gas phase  ${}^5\text{F}\text{U}$  around 5 eV and none at 10 eV, these fragmentations do not lead to an increase in strand breaks.

### 4.3. Discussion

In the following the F modified nucleobases and their natural nucleobase derivatives will be compared. Within the 5'-Bt-d(TTXTT)-3' sequence, these molecules were irradiated at 10 eV and in some additional cases at 5.5 eV. The determined absolute strand break cross sections are listed below in table 2.

Table 2. Overview of the absolute strand break (SB) cross sections of the  $^{2F}A$  and  $^{5F}U$  containing oligonucleotides at 10 eV and 5.5 eV.

5'-Bt-d(TTXTT)-3'	SB cross section (at 10 eV)	SB cross section (at 5.5 eV)
X = (ATA) <sub>3</sub>	$(0.80 \pm 0.12) \cdot 10^{-14} \text{ cm}^2$	$(1.36 \pm 0.02) \cdot 10^{-14} \text{ cm}^2$
X = ( $^{2F}AT^{2F}A$ ) <sub>3</sub>	$(1.34 \pm 0.22) \cdot 10^{-14} \text{ cm}^2$	$(2.12 \pm 0.09) \cdot 10^{-14} \text{ cm}^2$
X = ( $^{5F}UT^{5F}U$ ) <sub>3</sub>	$(1.31 \pm 0.25) \cdot 10^{-14} \text{ cm}^2$	$(1.17 \pm 0.11) \cdot 10^{-14} \text{ cm}^2$
X = (A $^{5F}UA$ ) <sub>3</sub>	$(1.20 \pm 0.20) \cdot 10^{-14} \text{ cm}^2$	
X = T <sub>8</sub>	$(0.79 \pm 0.07) \cdot 10^{-14} \text{ cm}^2$	

#### 4.3.1. Comparison of A and $^{2F}A$ at 10 eV

Boudaiffa *et al.* reported a local maximum in SSB sensitivity of the plasmid pGEM 3Zf(-) with 3199 nucleobase pairs towards 10 eV electrons with an effective strand break cross section for SSBs of  $2.6 \cdot 10^{-15} \text{ cm}^2$ .<sup>12,144</sup> Based on this finding the initial irradiation experiments in this work have been conducted with 10 eV as well. For the short 13mer oligonucleotide single strand 5'-Bt-d(TT(ATA)<sub>3</sub>TT)-3' an absolute strand break cross section of  $(0.80 \pm 0.12) \cdot 10^{-14} \text{ cm}^2$  was obtained in the experiments. The same sequence, but with the fluorinated nucleobase  $^{2F}A$  exhibits an *EF* of  $(1.7 \pm 0.5)$  at 10 eV compared to the A containing sequence. The increased strand break cross section of  $(1.34 \pm 0.22) \cdot 10^{-14} \text{ cm}^2$  indicates that  $^{2F}A$  is an efficient radiosensitizer, since LEEs with 10 eV energy are generated with a maximum probability during irradiation of cells with high energy irradiation.<sup>47</sup> Interestingly, a similar enhancement factor *EF* of 1.7 was obtained in previous experiments, as a maximum value in  $^{5Bf}U$  modified oligonucleotides at 18 eV.<sup>105</sup>

#### 4.3.2. Comparison of the energy dependencies of A and $^{2F}A$

For the oligonucleotide 5'-Bt-d(TT(ATA)<sub>3</sub>TT)-3' an absolute strand break cross section of  $(1.36 \pm 0.02) \cdot 10^{-14} \text{ cm}^2$  was obtained when irradiated with 5.5 eV electrons. Compared to the strand break cross section at 10 eV, the sensitivity of this sequence at 5.5 eV is 1.7 fold increased. The same sequence was studied before at 18 eV, yielding a strand break cross section of  $(6.00 \pm 0.86) \cdot 10^{-14} \text{ cm}^2$ .<sup>105</sup> Thus, at higher energy the SSB rate is 7.5 fold increased. The local SSB maximum for plasmids at 10 eV energy<sup>12</sup> was thus not confirmed in this well-defined single stranded oligonucleotide (Figure 45).

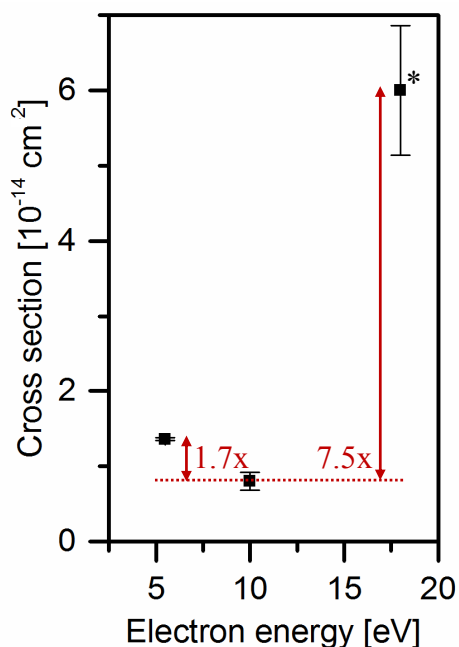


Figure 45. Energy dependence of the absolute strand break cross section of the 5'-Bt-d(TT(ATA)<sub>3</sub>TT)-3' sequence.

\*This value was obtained from Ref. 106.

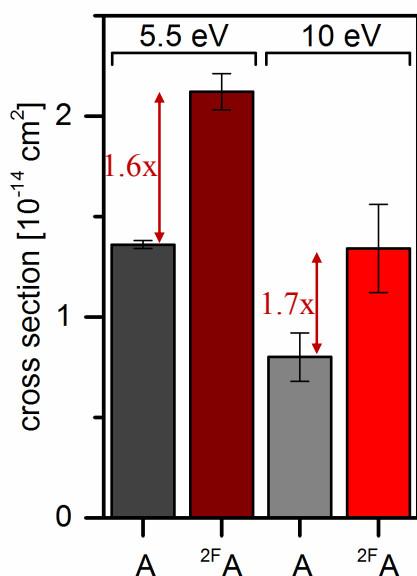


Figure 46. Comparison of the energy dependent cross sections of the two oligonucleotide sequences 5'-Bt-d(TT(XTX)<sub>3</sub>TT)-3' with X = A,  $^{2F}A$  at 5.5 eV and 10 eV.

With a determined absolute strand break cross section of  $(2.12 \pm 0.09) \cdot 10^{-14} \text{ cm}^2$ , the sensitivity of the oligonucleotide containing the fluorinated nucleobase  $^{2F}A$  is increased by a factor of  $1.6 \pm 0.3$  at 5.5 eV compared to 10 eV. Both the A and the  $^{2F}A$  containing sequence thus show an identical increase in sensitivity at the lower energy. Therefore, also the enhancement in strand breaks due to the fluorinated nucleobase  $^{2F}A$  remains constant at 5.5 eV, with an EF of  $1.6 \pm 0.1$  compared to the native nucleobase A containing sequence 5'-Bt-d(TT(ATA)<sub>3</sub>TT)-3' (Figure 46).

In gas phase experiments, A has shown a broad resonance with a maximum at 6.5 eV for the anion fragment (A-3H)<sup>-</sup>, and further signals around 5.5 eV from some smaller anion fragments.<sup>18,134</sup> At the same energy, <sup>2</sup>F A has a broad resonance forming the (<sup>2</sup>F A-H-F)<sup>-</sup> and (<sup>2</sup>F A-2H-F)<sup>-</sup> anion fragment. From the increased sensitivity of both sequences towards 5.5 eV electrons, it can be concluded, that the formation of these fragments can lead to single strand breaks in the oligonucleotide backbone.

#### 4.3.3. Comparison of A, T and <sup>5</sup>FU at 10 eV

To reliably compare both fluorinated nucleobases <sup>2</sup>F A and <sup>5</sup>FU, the homooligonucleotide 5'-Bt-d(T)<sub>12</sub>-3' was analyzed at 10 eV in addition to 5'-Bt-d(TT(ATA)<sub>3</sub>TT)-3'. For both sequences identical strand break cross sections were obtained, with  $(0.80 \pm 0.12)$  and  $(0.79 \pm 0.07) \cdot 10^{-14} \text{ cm}^2$ . Thus, no differences in SSB formation in both sequences were observed (Figure 47).

The sequences 5'-Bt-d(TT(A<sup>5</sup>FUA)<sub>3</sub>TT)-3' and 5'-Bt-d(TT(<sup>5</sup>FUT<sup>5</sup>FU)<sub>3</sub>TT)-3' were irradiated at 10 eV. For the oligonucleotide containing the fluorouracil three times, an absolute strand break cross section of  $(1.20 \pm 0.20) \cdot 10^{-14} \text{ cm}^2$  was obtained. This sequence is only slight less sensitive towards 10 eV LEEs than the sequence containing <sup>5</sup>FU six times with a strand break cross section of  $(1.31 \pm 0.25) \cdot 10^{-14} \text{ cm}^2$ . Thus, the amount of <sup>5</sup>FU contained in the nucleotide sequence does not influence the sensitivity towards LEEs at 10 eV significantly. Furthermore, the sensitivity is independent of the neighboring nucleobase A or T (Figure 47). As discussed above, an opposite influence on the strand break cross section of both, the neighboring nucleobase and the amount of <sup>5</sup>FU cannot entirely be excluded.

At 10 eV, both sequences containing <sup>5</sup>FU showed an enhancement factor of  $1.5 \pm 0.1$  and  $1.6 \pm 0.5$ , compared to 5'-Bt-d(TT(ATA)<sub>3</sub>TT)-3'. Thus, both have similar sensitivities

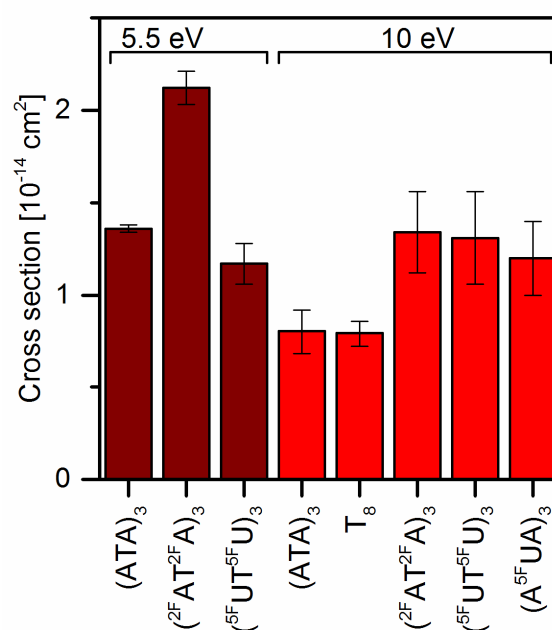


Figure 47. Comparison of all obtained absolute strand break cross sections for the oligonucleotides 5'-Bt-d(TT<sub>X</sub>TT)-3', with X = (ATA)<sub>3</sub>, T<sub>8</sub>, (<sup>2</sup>F AT<sup>2</sup>F A)<sub>3</sub>, (<sup>5</sup>F UT<sup>5</sup>F U)<sub>3</sub> and (A<sup>5</sup>FUA)<sub>3</sub> at 5.5 eV and 10 eV.

towards 10 eV electrons as the  $^{2F}A$  containing nucleotide. Therefore, it can be concluded, that the fluorination at the nucleobase is more important to the sensitivity than the type of the nucleobase itself. This is rather surprising since the fragmentation of the pyrimidine base  $^{2F}A$  in DEA gas phase experiments is quite different from that of the purine base  $^{5F}U$ .<sup>79,141</sup> In addition, none of them show relevant resonances around 10 eV. Yet both F containing nucleobases showed significant SSB enhancement in oligonucleotides. The higher electronegativity of F compared to H might draw electron density from the nucleobase, improving the antenna effect for the electrons and leading to DNA backbone decomposition by electron delocalization. With an additional experiment with F at the sugar this might be confirmed.

#### **4.3.4. Comparison the energy dependence of $^{5F}U$ and $^{2F}A$**

The 5'-Bt-d(TT( $^{5F}UT^{5F}U$ )<sub>3</sub>TT)-3' oligonucleotide was irradiated at 5.5 eV as well, resulting in an absolute strand break cross section of  $(1.17 \pm 0.11) \cdot 10^{-14} \text{ cm}^2$ . Thus, the sensitivity of the  $^{5F}U$  containing sequence is slightly decreased by a factor of  $0.9 \pm 0.2$  at this energy. Within the margin of error, however, the sensitivity of the sequence is identical at both energies, although DEA resonances have been obtained in the gas phase around 5.5 eV.<sup>79</sup> This is in contrast to the  $^{2F}A$  containing nucleotide, where an increase of  $1.6 \pm 0.3$  was obtained at 5.5 eV (Figure 47). Since for the 5'-Bt-d(TT( $^{5F}UT^{5F}U$ )<sub>3</sub>TT)-3' oligonucleotide no increase in sensitivity at 5.5 eV could be obtained, the enhancing nucleotide unit is the  $^{2F}A$ . Because all sequences have the same sugar phosphate backbone and amount of T, the energy dependent enhancing effect appear through  $^{2F}A$  and lead to SSB in the sugar-phosphate backbone.

#### **4.3.5. Margin of error and efficiency of the methods**

The error of the strand break cross section for  $^{2F}A$  and A containing oligonucleotides at 10 eV is rather high due to the different methods for determining the AFM image positions (Figure 48). During the initial procedure, two diagonal scratches have been used. Between them the DNA origami triangles have been immobilized. The AFM images have been taken close to the end of the scratches (red circles in Figure 48). In result, only

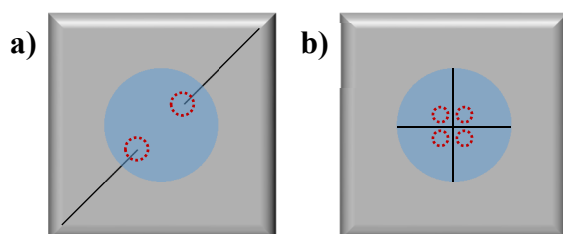


Figure 48. Schematic drawing of the marker scratches on the silicon sample for **a)** 5'-Bt-d(TT(ATA)<sub>3</sub>TT)-3' and 5'-Bt-d(TT(<sup>2F</sup>AT<sup>2F</sup>A)<sub>3</sub>TT)-3' at 10 eV, and **b)** the optimized marker for the other experiments.

two areas could be localized, with varying distances from the center. This leads to an increased variation of fluence within the analyzed AFM images, combined to the calculated fluence for the area B (profile 1). The optimized procedure (Figure 48.b) on the other hand, uses a central marker scratch, defining precisely the center of irradiation. Furthermore, with the top-view AFM camera, the distance of each AFM image from the center can be

determined and correlated to the calculated fluence of this area. In result, the average error of the determined strand break cross section could be decreased significantly compared to the initial method used for 5'-Bt-d(TT(ATA)<sub>3</sub>TT)-3' and 5'-Bt-d(TT(<sup>2F</sup>AT<sup>2F</sup>A)<sub>3</sub>TT)-3' at 10 eV.

The margin of error of the absolute strand break cross section is higher when the relative method is used for determination, since the error of the reference sequence is taken into account as well. Comparing the margins of error of all sequences analyzed in this chapter, this increasing effect becomes visible (Figure 49). Yet compared to the error of the strand break cross sections obtained with the absolute method, the additional error through the relative method is rather small. This indicates that the error of the strand break cross section using the absolute method arises from fluence variations. These variations can occur through an off-center irradiation position and AFM images taken at different distances from the center of irradiation, since the fluence at the analyzed position might vary from the calculated fluence for the central area. In case the relative method is used, the analyzed data is fluence independent. Thus, the additional error in the relative method is rather small. For future studies it is advisable to analyze a reference sequence with as many samples as needed to obtain an error of the strand break cross section below 10 %, and then using the relative method to study further sequences with similar structure as the reference at the same energy.

Choosing the right time for irradiation in the relative method is rather simple. Comparing both experiments of 5'-Bt-d(TT(<sup>5F</sup>UT<sup>5F</sup>U)<sub>3</sub>TT)-3' with 20 s and 60 s (Figure 50), the independence from the fluence for the relative method could be proofed, since the calculated strand break cross sections for both experiments are identical within the margin

of error. Therefore the irradiation time is negligible as long as the saturation of  $N_{SB}$  is not reached. Very small irradiation times can increase the error, since the  $N_{SB}$  value will be rather small and, therefore, the variations over all images might increase. Long irradiation times on the other hand can easily reach the saturation regime and thus result in wrong ratios between both sequences.

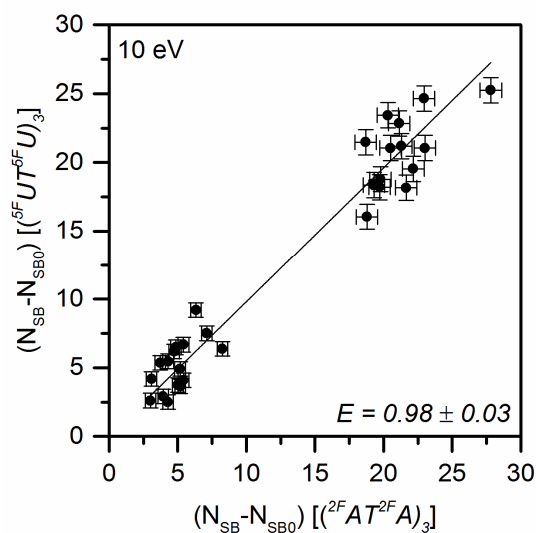


Figure 50. Correlation between  $\Delta N_{SB}$  values of two sequences 5'-Bt-d(TTXTT)-3', with  $X = (^{5F}UT^{5F}U)_3$  and  $(^{2F}AT^{2F}A)_3$  at 10 eV with two irradiation times of 20 s and 60 s. The x-axis corresponds to the reference sequence. The ratio  $E$  have been obtained from the slope of the linear fit.

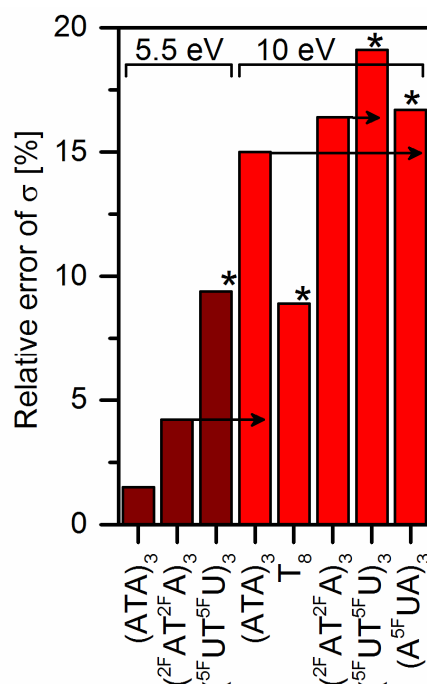


Figure 49. Comparison of the relative error of the absolute strand break cross sections from all sequences 5'-Bt-d(TTXTT)-3' studied in this chapter. \* Value obtained with the relative method, from reference sequences indicated by  $\rightarrow$ .  $T_{12}$  was analyzed relative to Telo2 (not mentioned in this graph).

## 5. Secondary structures - Telomere derived sequences

This chapter will present a variation of telomere sequences and their sensitivity towards 10 eV electrons. All samples were prepared with the standard preparation procedure (supplement 7.1). Table 3 below contains the oligonucleotide sequences and their position on the DNA origami triangle, the method used for analysis, the current during irradiation, the beam profile used for calculation, the resulting absolute strand break cross section, and the relative error of the calculated strand break cross section.

The resulting strand break cross sections at 10 eV will be used to compare the sensitivity of different telomere sequences towards LEEs. Especially the influence of oligonucleotide length, minor variations of the nucleobase sequence down to single-nucleotide polymorphism (SNP), and the direction and order of the nucleobases in the sequence will be investigated. Further, the influence of the cations  $Mg^{2+}$  and  $K^+$ , which are known to fold telomere sequences, will be analyzed.<sup>70</sup>

In this work, the natural, human telomere sequence **Telo2N** will be compared with the reversed sequence **Telo2**. Additional to the oligonucleotide polarity, the G stacking interactions will be investigated, comparing the intermixed sequence **Telo2M** with the **Telo2** sequence, where three G can interact. Both aspects, direction and order, will be studied with an oligonucleotide single strand containing the telomere derived sequence twice. The extension of the nucleotide with additional telomere units will be investigated as well, to study the length dependency from **Telo2** with two and **Telo3** with three to **Telo4** with four repeating units of the reversed telomere sequence. The length dependence investigation will be followed by the special SNP in the telomere sequence, changing the A to a fourth G. In result, the human telomere sequences **Telo2** and **Telo4** will be compared with the reversed sequences of the ciliate *Tetrahymena* telomere **Telo2G** and **Telo4G**. Finally, the presence of  $K^+$  will be studied with various telomere derived sequences and compared with the absolute strand break cross sections without  $K^+$ . Especially the various folding patterns and their influence on the determined absolute strand break cross section will be discussed, from short to long telomere nucleotides, with SNP and in the presence of  $K^+$ .

Table 3. Overview of all telomere derived sequences studied in this chapter.

Name	Oligo sequence X (5'-Bt-d(TTXX)-3')	Method*	Position on the origami <sup>#</sup>	Current [nA]	Beam profile <sup>°</sup>	SB Cross section [10 <sup>-15</sup> cm <sup>2</sup> ]	Relative error [%]
<i>Telo2</i>	(GGG ATT) <sub>2</sub>	A (with Telo2G)	a	3.0 - 6.0	1	6.78 ± 0.54	8.0
<i>Telo2G</i>	(GGG GTT) <sub>2</sub>	A	c	3.0 - 6.0	1	6.02 ± 0.31	5.1
<i>Telo3</i>	(GGG ATT) <sub>3</sub>	A (with Bt)	c	3.5 - 7.5	2	8.02 ± 0.76	9.5
<i>Telo4</i>	(GGG ATT) <sub>4</sub>	A (with Telo4G)	b	2.5 - 4.0	1	8.67 ± 1.35	15.6
<i>Telo4G</i>	(GGG GTT) <sub>4</sub>	A	a	2.5 - 4.0	1	10.30 ± 1.29	12.5
<i>Telo2N</i>	(TTA GGG) <sub>2</sub>	R (to Telo2)	b	5.0 - 7.5	2	6.74 ± 0.56	12.0
<i>Telo2M</i>	(TG TG TG A) <sub>2</sub>	R (to Telo2G)	a	4.0 - 7.0	2	4.51 ± 0.27	6.0
<i>Experiments in the presents of 100 mM KCl:</i>							
<i>Telo4</i>	(GGG ATT) <sub>4</sub>	A (with Telo4G)	b	2.0 - 5.0	1	8.05 ± 0.53	6.6
<i>Telo4G</i>	(GGG GTT) <sub>4</sub>	A	a	2.0 - 5.0	1	8.26 ± 0.50	6.1
<i>Telo3</i>	(GGG ATT) <sub>3</sub>	A (with Telo2M)	c	1.5 - 3.5	2	7.66 ± 1.57	20.5
<i>Telo2M</i>	(TG TG TG A) <sub>2</sub>	A	a	1.5 - 3.5	2	4.35 ± 0.38	8.7

\**Method:*

A – Absolute; complete fluence dependence, containing two series with six irradiated samples and two non-irradiated control samples each.

R – Relative; averaged over six identically irradiated samples with two non-irradiated control samples.

<sup>#</sup>*Position on the origami:*

a – t1s8i, t1s18i, t1s28i;                      b – t-5s8g, t-5s18g, t-5s28g;                      c – t7s8g, t7s18g, t7s28g.

<sup>°</sup>*Beam profile:* (percentage of the total electron current, which irradiates the central 1 mm diameter area of the sample, see chapter 3.3, table 2)

1 – 7.04 %

2 – 5.96 %.

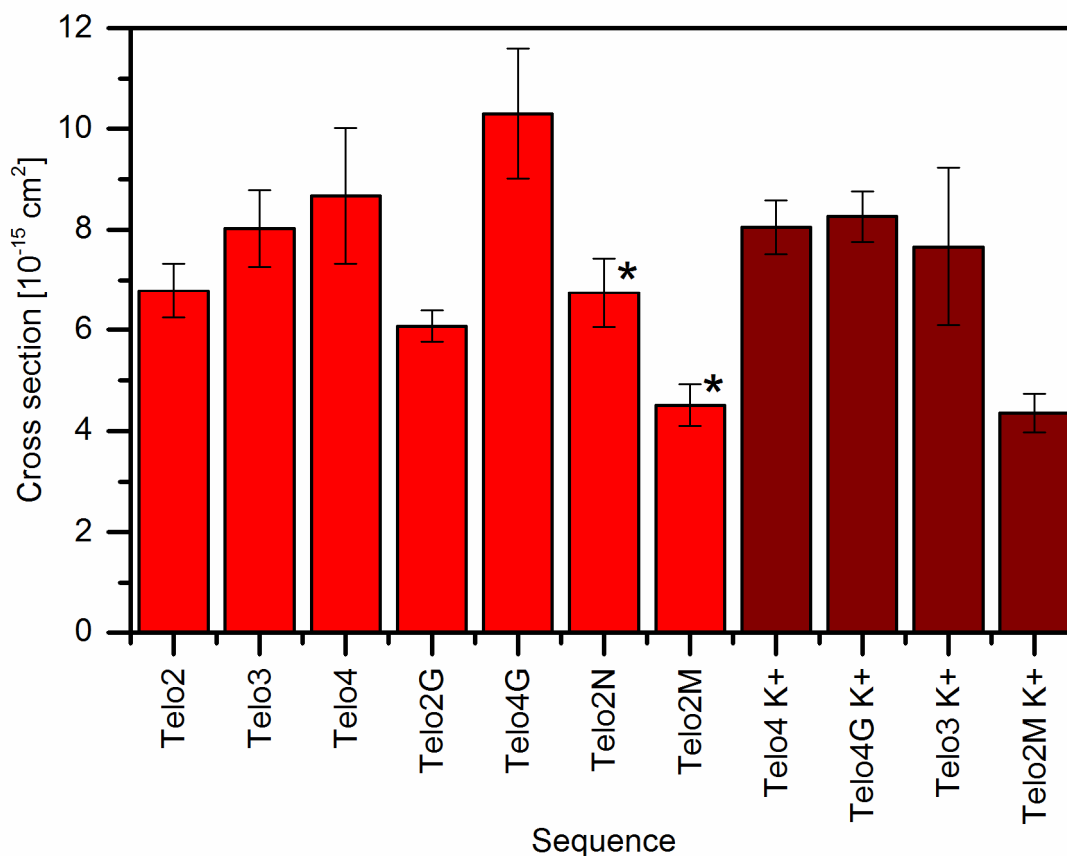


Figure 51. Absolute strand break cross sections of all analyzed telomere derived sequences. \* identifies the relative measurements.

As can be seen in Figure 51, the dynamic range of the telomere sequences strand break cross sections at 10 eV is rather small, but significant with 4 to  $10 \cdot 10^{-15} \text{ cm}^2$ . The obtained strand break cross sections can be still compared as long as their difference is statistically significant. The minor differences in the determined strand break cross sections thus reflect the various nucleobase combinations and topological effects. Furthermore, the changes in strand break cross sections of different sequences can be compared to understand nucleotide sensitivity towards LEEs. Those aspects will be discussed in the following.

### 5.1. Order of the nucleotides

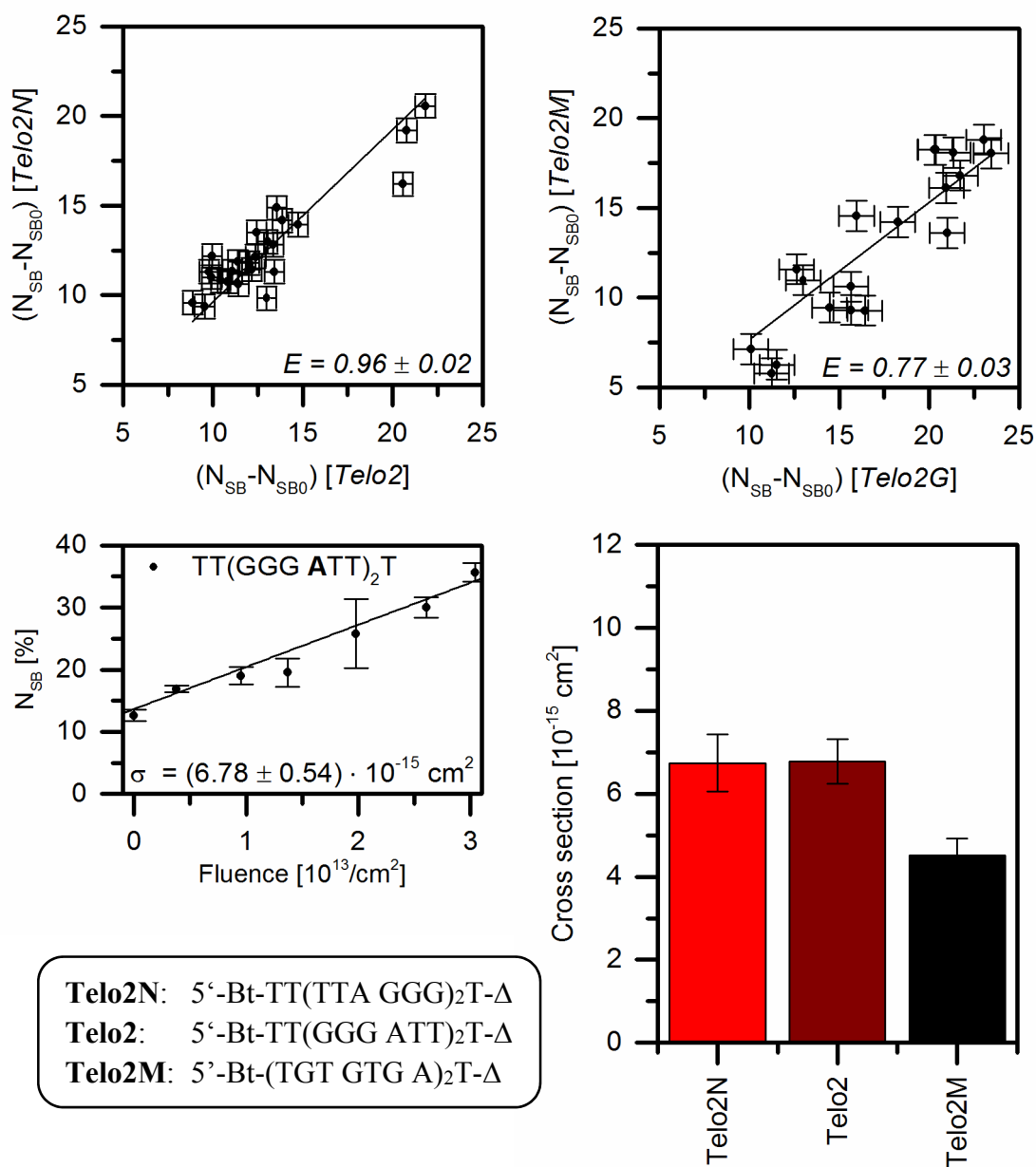


Figure 52. Illustration of the absolute strand break cross sections of Telo2N, Telo2 and Telo2M. Telo2N was analyzed relative to Telo2, Telo2M relative to Telo2G (not mentioned here).

The natural human telomere sequence is orientated 5'-(TTA GGG)<sub>n</sub>-3' (Telo2N, with  $n = 2$ ).<sup>58</sup> The reversed oligonucleotide Telo2 contains the same type and number of nucleobases as Telo2N (Figure 52). For the most reliable, comparable results, both sequences were analyzed together and the strand break cross section of Telo2N was determined relative to Telo2. As shown in the table 3 above, both sequences have identical strand break cross sections within the margin of error. Thus, the polarity of the sequence is of negligible importance. Therefore, in the remainder of this work, all other sequences are derived from the reversed sequence Telo2.

The sequence Telo2 contains seven T, six G and two A (TT(GGG ATT)<sub>2</sub>T). Previous experiments have revealed an influence of G stacking on the electronic properties of the telomere sequence,<sup>72</sup> which was later supported by simulations.<sup>145</sup> Both, experiment and simulation, propose a charge transfer from a G stack to A, resulting in a slightly positively charged G, which can then act as an electron “antenna”. To study this influence in Telo2, the sequence was intermixed into (TG TG TG A)<sub>2</sub>T, referred to Telo2M (Figure 52). In the results of the irradiation experiments with 10 eV electrons, the influence of neighboring nucleobases is clearly visible. The strand break cross section from Telo2 with  $(6.78 \pm 0.54) \cdot 10^{-15} \text{ cm}^2$  is decreased by a factor of  $(0.7 \pm 0.1)$  to  $(4.51 \pm 0.27) \cdot 10^{-15} \text{ cm}^2$ . Thus, the scrambled oligonucleotide sequence is less sensitive towards 10 eV electrons. Hence the stacking interactions with neighboring nucleobases in Telo2 increase the strand break cross section, improving the “antenna” effect to capture LEEs. Therefore, the obtained results confirm, that the natural telomere sequence has a special affinity towards LEEs, making strands breaks in this region of the chromosome more likely.

## 5.2. Length dependency

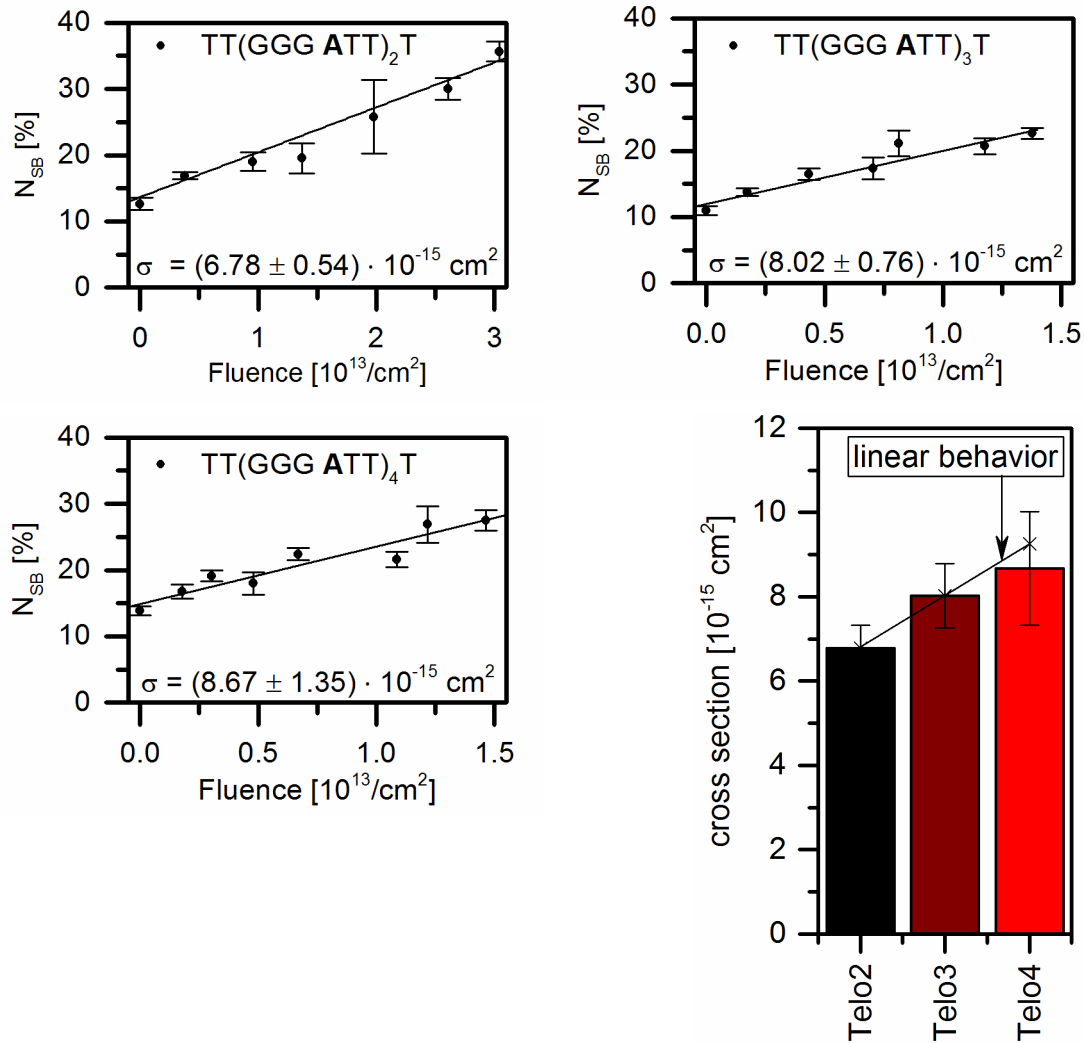


Figure 53. Illustrations of the absolute strand break cross sections of Telo2, Telo3 and Telo4 with extrapolation of the length dependency.

The results for the absolute strand break cross sections of the extended periodic telomere sequences Telo2, Telo3 and Telo4 indicate a length dependency of the strand break cross section with increased sensitivity towards 10 eV electrons for longer oligonucleotides (Figure 53). This effect can either result from the increased overall amount of nucleobases or the increased amount of G within the strand in particular. The latter was already studied in previous experiments, where the authors describe an increasing sensitivity towards 1 eV electrons of sequences with increasing amount of G in strands of identical length.<sup>108</sup> The increased sensitivity from Telo2 to Telo3 defines the value for extension by one telomere repeat (GGG ATT). Extrapolating from this, Telo4 should have an absolute strand break cross section of  $(9.26 \pm 1.3) \cdot 10^{-15} \text{ cm}^2$ . The obtained value of  $(8.67 \pm 1.35) \cdot 10^{-15} \text{ cm}^2$  agrees fairly well with the expected value within the experimental error.

In general, G-quadruplexes are formed in the presence of monovalent cations, i.e.  $\text{Na}^+$  and  $\text{K}^+$ .<sup>64,117</sup> A detailed study of quadruplex folding by Rajendran *et al.* has shown, however, that also  $\text{Mg}^{2+}$  influences quadruplex folding especially by forming intermediate G-hairpins (two strands) and G-triplexes (three strands).<sup>70</sup> Based on the rather large amount of detectable intermediates, the authors conclude, that these intermediates have a rather long lifetime and, therefore, stability. Thus, it can be expected, that for short sequences, such as Telo2 and Telo3, these intermediates will be formed up to a certain degree (Figure 54.b). The longer the oligonucleotide, the higher the probability of folded structures with various topologies will be. Thus, in Telo4, the probability of folded structures is higher than in Telo2. This effect is reflected in the considerably larger error of the absolute strand break cross section (Figure 54.a). Due to the high variation of topology in one Telo4 sample, various structures with different strand break cross sections have been probed at the same time in our experiment, resulting in a larger error.

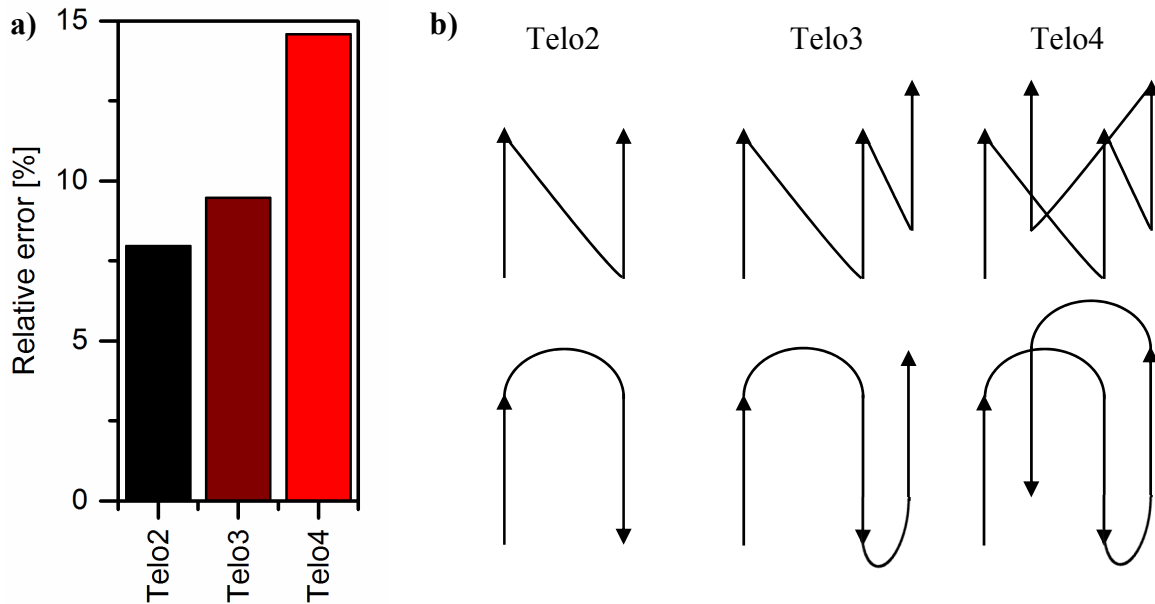


Figure 54. a) Plot of the relative error of the absolute strand break cross sections of Telo2, Telo3 and Telo4. b) Schematic drawing of some possible folding patterns of Telo2, Telo3 and Telo4. Parallel folded strands are illustrated in the first row, while anti-parallel folded strands are in the second row. Each mentioned oligonucleotide can fold into the pattern with the number of repeats of the telomere sequence or a structure with less repeat units involved. Thus, Telo4 can fold into the highest number of different topologies, with hairpin (two strands), triplex (three strands) and quadruplex (four strands).

### 5.3. Influence of loop base replacement

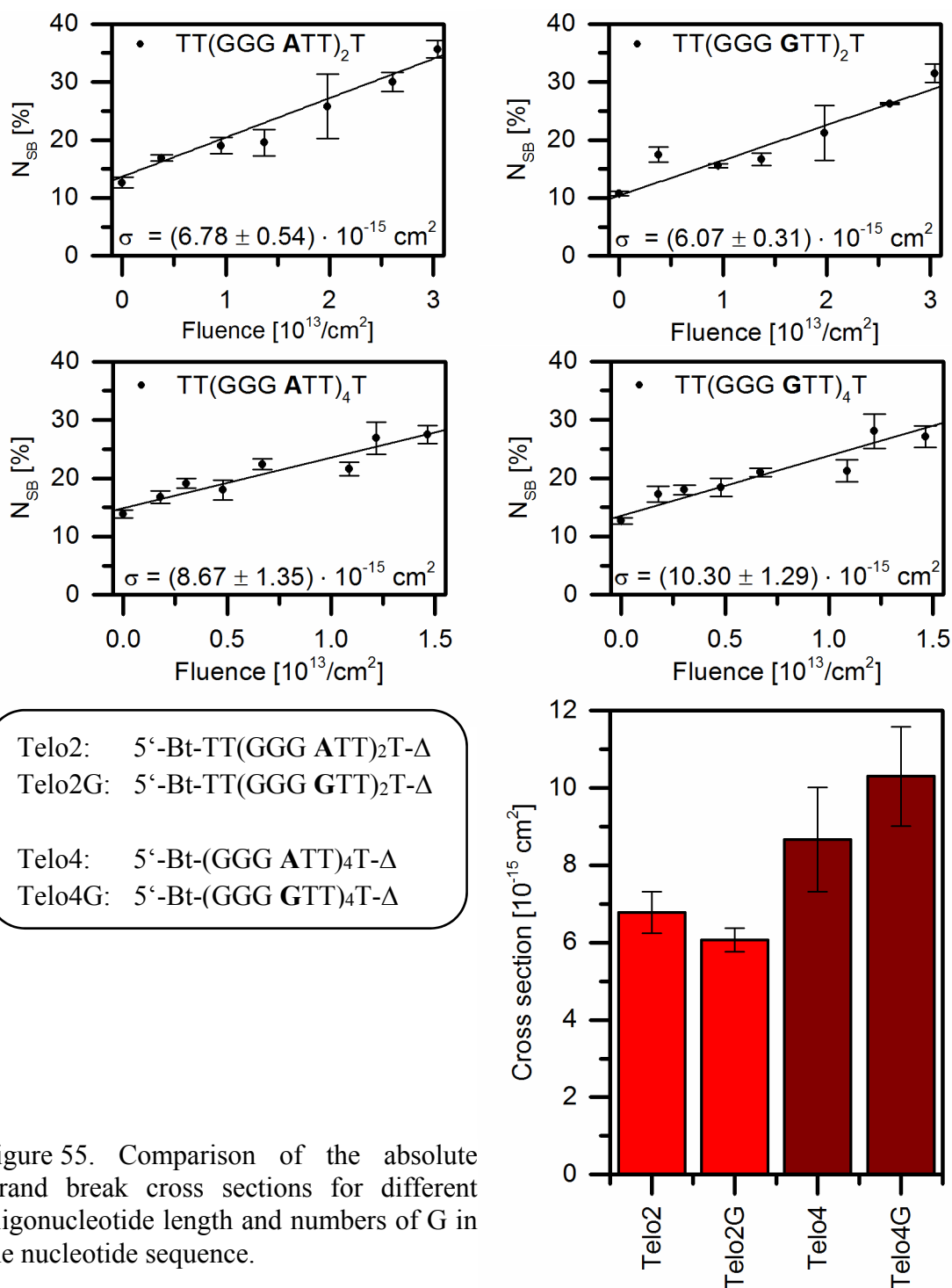


Figure 55. Comparison of the absolute strand break cross sections for different oligonucleotide length and numbers of G in the nucleotide sequence.

Theoretical studies have shown that an increasing amount of G in general reduces the ionization potential of telomere derived sequences.<sup>145</sup> However, an A adjacent to three G significantly decreases the ionization potential compared to four G without A. It was demonstrated that the human telomere sequence has a higher capturing probability of electrons.<sup>72,145</sup> Since the capturing probability of A is lower than that of G, this effect does not simply arise from the A-G substitution. Therefore it was suggested that this is a result of the G-A interaction, with charge transfer from G to A. The now slightly positively charged G can act as an antenna. This effect was already obtained in this work for Telo2 compared with Telo2M (see chapter 5.1). To study the influence of A in more detail, the human telomere sequence Telo2 was modified to Telo2G, containing four G and no A. The TeloG sequence (T<sub>2</sub>G<sub>4</sub>) occurs naturally as well, in the ciliate *Tetrahymena*. Comparing both sequences, Telo2 and Telo2G, the oligonucleotide sequence with a fourth G instead of A is slightly less sensitive by a factor of  $0.9 \pm 0.1$  towards 10 eV electrons (Figure 55), which correlates with previously published theoretical<sup>145</sup> and experimental results.<sup>72</sup>

However, Telo4 and Telo4G have shown a contrasting behavior with the increased amount of G, resulting in an increased absolute strand break cross section by a factor of  $1.2 \pm 0.3$ .

In the presence of Na<sup>+</sup>, Telo2G is known to fold into two different intermolecular asymmetric G-quadruplexes, consisting of two forms of hairpins but no intramolecular G-quadruplexes due to the short length of the sequence.<sup>146</sup> Based on NMR studies, Phan *et al.* suggest, that in the presence of K<sup>+</sup>, different G-quadruplexes are formed by Telo2G than by Telo4G.<sup>146</sup> The intramolecular quadruplex of Telo4G is formed by three tetrads connected by two edgewise loops and one double-chain reversal loop. The intermolecular Telo2G quadruplex folds either in parallel or anti-parallel configuration. Since both are separated by the same GTT loop, the origin of this difference is still unknown.<sup>146</sup> During the experiments in this work, neither K<sup>+</sup> nor Na<sup>+</sup> were present. The dominant cation during the experiment was Mg<sup>2+</sup>, thus the possible folding pattern and topology is unclear. Based on Rajendran *et al.*,<sup>70</sup> it can be expected, that Mg<sup>2+</sup> folds G-quadruplex intermediates in Telo2G and Telo4G as well as in Telo2 and Telo4. The possible formed G-hairpins and G-triplexes then stabilize some of the sequences, creating a variation in the absolute strand break cross section. Since the margin of error is not increased for Telo2G and Telo4G compared to Telo2 and Telo4, this intermediate folding by Mg<sup>2+</sup> seems, however, unlikely for the sequences featuring four G per repeat. Telo4G and Telo4 were analyzed within one experiment, thus experimental variations would have influenced the margin of error of both sequences in the same way. This indicates that

Telo4G is mainly unfolded in the presence of  $Mg^{2+}$ , while a significant part of Telo4 is folded into a quadruplex or its intermediates. To exclude the possibility that all Telo4G sequences are already folded in the presence of  $Mg^{2+}$ , further experiments were performed with  $K^+$  (see chapter 5.4), since the capability of  $K^+$  to form G quadruplexes for both sequences, Telo4 and Telo4G, is well documented.

In previous theoretical<sup>145</sup> and experimental studies of ionization and electron capture by telomeres,<sup>72</sup> the effect of possible G-quadruplex folding has not been considered. Assuming a changed topology in Telo4 and Telo4G, the reduced absolute strand break cross section may be attributed to topologically stabilized structures. Furthermore, the surrounding cations might influence the electron capturing probability of G.

In chapter 5.2 the length dependency of the absolute strand break cross section of the telomere sequence was already discussed. Comparing Telo2G and Telo4G, this dependency is confirmed, with an even higher increase by a factor of  $1.7 \pm 0.3$  from Telo2G to Telo4G. This factor is higher than the one observed for Telo2 to Telo4 ( $1.3 \pm 0.3$ ), since Telo4 is assumed to be folded to some extent, as already discussed.

#### 5.4. Influence of potassium ions on the topology

$Mg^{2+}$  and  $K^+$  are the most abundant di- and monovalent cations in cell plasma. Both have a strong influence on the topology of the folded quadruplex.<sup>69,70</sup> Rajendran *et al.* have shown that already small concentrations of  $Mg^{2+}$  can fold the G-quadruplex and its intermediates.<sup>70</sup> In the present work, the  $Mg^{2+}$  concentration needed to be rather high to immobilize the DNA origami on the silicon surface. Although the presented results suggest that all telomere sequences are folded to a certain degree, only the margins of error of Telo4 seem to be directly influenced. Besides this, the degree of folding cannot be determined from the experiments. To study this issue in greater detail, however, the sequences can be forced to fold by using cations which are known to fold G-quadruplexes. In previous experiments, telomeres attached to DNA origami were folded in the presence of  $K^+$ .<sup>131</sup> Since the experiments of the present work require the samples to be washed and dried, the cation concentration for quadruplex folding was chosen to be rather high, *i.e.* 100 mM KCl, in order to preserve the quadruplex structure also in the dry state. After immobilization of the DNA origami on the silicon, the sample was incubated with 10 x TAE buffer with 200 mM  $MgCl_2$  and 100 mM KCl. As a result, the percentage of  $Mg^{2+}$  folded G-quadruplexes is supposed to be small compared to  $K^+$  folded G-quadruplexes. According to Rajendran *et al.*,<sup>70</sup> it can be expected, that  $Mg^{2+}$  will fold the intermediates, while  $K^+$  will stabilize the G-quadruplexes, since the G-hairpin is preferably folded with  $Mg^{2+}$  over  $K^+$ , while the G-triplex is folded by both ions competitively, and the G-quadruplex is folded more likely with  $K^+$ .<sup>70</sup>

The intermixed sequence Telo2M with 5'-(TGT GTG A)<sub>2</sub>T-3' was assumed to be non-foldable into any secondary structure. Thus, the absolute strand break cross section was expected to be constant for both experiments, with and without  $K^+$ . This expectation was confirmed by the results, both strand break cross sections are identical within the margin of error (Figure 56). Therefore, it can be concluded that the presence of  $K^+$  bound to the DNA does not influence the sensitivity towards 10 eV electrons. Any further observations in variations of the strand break cross section with  $K^+$  in certain sequences thus do not result from the  $K^+$  ion itself.

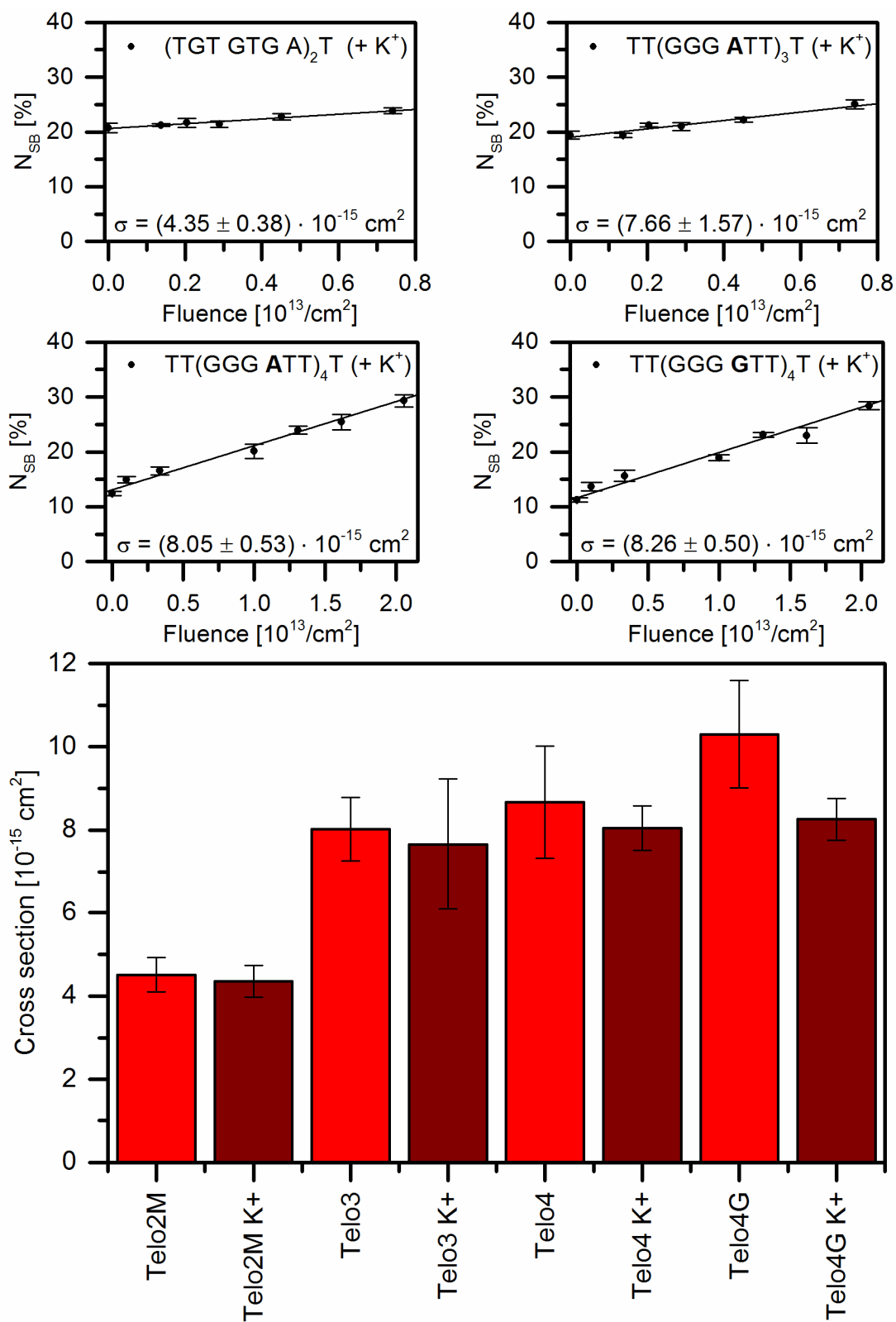


Figure 56. Absolute strand break cross sections of the sequences Telo2M, Telo3, Telo4 and Telo4G incubated with (dark red) and without 100 mM KCl (red).

The Telo3 sequence 5'-TT(GGG ATT)<sub>3</sub>T-3' cannot fold a quadruplex, yet a G-triplex is possible as a temporary stable intermediate. Rajendran *et al.* observed a similar distribution of G-triplex structures formed by Mg<sup>2+</sup> and K<sup>+</sup>.<sup>70</sup> Thus, it can be expected that the G-triplex on the DNA origami is folded with the same probability by both cations, resulting in similar strand break cross sections. This is confirmed by the obtained results. Yet the margin of error for Telo3 with K<sup>+</sup> is rather high, compared to the error of TeloM with K<sup>+</sup>. Since both sequences were analyzed together, experimental variations can be excluded. Thus, the increased error of Telo3 with K<sup>+</sup> might have the same origin as in Telo4, i.e. a broad distribution of the topologies of the Telo3 structures induced by K<sup>+</sup>. Therefore, it appears possible that Mg<sup>2+</sup> folds G-hairpins in Telo3, while in the presence of K<sup>+</sup> the number of G-triplex structures is increased. This is in contrast to the data published by Rajendran *et al.*,<sup>70</sup> which probably occur through the difference of intra- and intermolecular folding. In the present experiments, the Telo3 can fold only intramolecular.

Within the margins of error, the absolute strand break cross section of Telo4 is independent of the additional presence of K<sup>+</sup>. Only the error is reduced from 15.6 % to 6.6 %, confirming the hypothesis of topology variations of Telo4 without K<sup>+</sup>. This indicates that in Telo4 most of the strands are folded into some variation of secondary structure, while with K<sup>+</sup> those variations are transformed into a high percentage of folded G-quadruplexes. Alternatively, the decreased margin of error with K<sup>+</sup> might result from a different folding pattern of the G-quadruplex and its intermediates. For Na<sup>+</sup> and K<sup>+</sup>, variations of the folding pattern are well established.<sup>64,69,146</sup> So far, no NMR data or crystal structures were published for Mg<sup>2+</sup> quadruplexes, leading to the assumption that Mg<sup>2+</sup> preferably stabilizes the intermediate G-hairpins and G-triplexes. Their structure mainly depends on the strand orientations and loop direction, since the folding can happen only intramolecular. As intermediates to the more stable G-quadruplex, they might be resolved during the SA<sub>v</sub> incubation after irradiation. The G-quadruplex on the other hand might stay intact during the incubation time of 2 minutes, since the unfolding process is rather slow.<sup>147</sup> Figure 57 illustrates the possible pathways of folding and unfolding, and resulting detected signal.

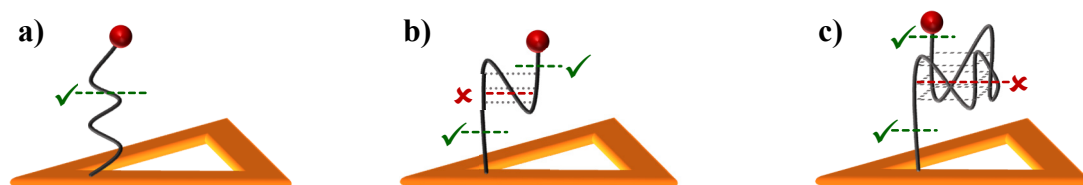


Figure 57. Schematic drawing of **a)** a stretched, **b)** a folded G-hairpin, and **c)** a propeller shaped G-quadruplex formed by a telomere nucleotide  $(GGG\ ATT)_n$ . The drawing illustrates potential strand breaks which are visible in AFM images through loss of the strand fragment attached to SA<sub>v</sub> (green ✓) and strand breaks which might not lead directly to a loss of the fragment (red ✖). The latter strand breaks can be stabilized by the G-G interaction between two or more strands. Especially the quadruplex in **c)** is held together by stacked tetrads which might compensate possible strand breaks in the folding region.

A single strand break in the stretched nucleotide will be detected in any case, since the fragment will be washed away, leaving no Bt at the end of the strand. In result, this strand will be counted as broken (Figure 57.a). Even the short Telo2 can fold a G-hairpin, which might slightly stabilize the structure. In this case, fragmentations close to the Bt and the DNA origami lead to a loss of the SA<sub>v</sub> signal in the AFM, while SSBs inside the hairpin region might be bridged by hydrogen bonds of paired nucleobases and the cation (Figure 57.b). This effect increases significantly with the folding of Telo4 into a G-quadruplex. Here, the Hoogsteen base pairing and the stabilizing cation form a stable complex with many loops exposed to LEEs, while the G is shielded inside the complex, holding the possible fragments together. Depending on the length of the fragment and the folding pattern induced by the cation, the incubation time may or may not be sufficient to remove the fragments and the Bt label to attach SA<sub>v</sub> on the DNA origami. In conclusion, with increased amount of G-quadruplexes and their ion dependent folding pattern, many SSBs may remain undetected, since SA<sub>v</sub> can attach to the Bt label on a cleaved strand, which is held together by tetrad stacking. A strand break in the folding region only changes the intramolecular folded into an intermolecular G-quadruplex.

The influence of  $K^+$  is the strongest for the Telo4G structure. Telo4G is less sensitive towards 10 eV electrons by a factor of  $0.8 \pm 0.1$  after 5 minutes exposure to 100 mM  $K^+$ . Based on the already discussed aspects of cation depending folding patterns and G-quadruplex stabilization, it can be assumed that most of the Telo4G strands are folded

into stable G-quadruplexes, which in result are either less sensitive towards 10 eV electrons or more stable when already fragmented (Figure 57.c).

## 5.5. Conclusion

Although the dynamic range of the absolute strand break cross sections is rather small, clear effects within the telomere derivatives could be obtained. While the polarity of the telomere sequence on the DNA origami does not influence the sensitivity towards 10 eV, the stacking of G with a neighboring A influences the strand break cross section quite severely by a factor of  $(1.5 \pm 0.2)$  when comparing the human telomere sequence Telo2 to the scrambled Telo2M. In addition to this effect of the neighboring nucleobase, a clear length dependency was obtained for Telo2 to Telo4 and Telo2G to Telo4G, with an increased sensitivity of the extended oligonucleotides. In Telo4, a population distribution of unfolded and folded strands increases the margin of error. This effect was reduced by adding  $K^+$ , resulting in similar strand break cross sections with reduced error from a more homogenous population of folded G-quadruplexes. From the obtained data it is assumed that Telo4 and Telo4G fold into similar G-quadruplex structures in the presence of  $K^+$ , while with  $Mg^{2+}$  Telo4G stays mainly unfolded. The  $Mg^{2+}/K^+$  influence on the intermediates and the stable G-quadruplex as published by Rajendran *et al.* was confirmed by these results.<sup>70</sup> Furthermore, the increased population distribution occurring in Telo3 with  $K^+$  indicates an increased percentage of intermediates with more stable G-triplex structures.

Thus, in addition to G stacking and strand length, the topology of the nucleotide influences the absolute strand break cross section of the telomere sequence quite strongly. Since the folding cannot be totally suppressed, the absolute strand break cross section for unfolded telomeres are still unknown. Furthermore, the removal of all SSB fragments cannot be guaranteed so far. This problem may be overcome in future experiments, for instance by using crown ethers for  $K^+$  or  $Mg^{2+}$ , increased temperatures, or decreased cation concentrations to unfold the G-quadruplex and remove the fragments. However, each of these processes will need a rather long period of exposure to a different solvent or reduced cation concentration, and might thereby degrade the DNA origami.

## 6. Summary

In this work the energy and sequence dependent dissociation of oligonucleotide DNA backbones by LEE-irradiation is studied. The entire experimental setup was constructed from scratch. Both, the irradiation process and the sample preparation procedure were optimized to minimize the error of the strand break cross sections. The fluence calculation was modified to improve the correlation between the local fluence and the area of AFM imaging. In result, absolute strand break cross sections with an average margin of error around 10 % could be obtained. Two methods to determine sequence dependent strand break cross sections are presented, the basic absolute method, which can be used for determination of at least two different sequences in one experiment at various energies, and the relative method, which can be used for comparison of one unknown sequence (and its strand break cross section) with a known reference. The latter method has the advantage that it requires fewer experimentally obtained data. Furthermore, the additional error is rather small compared to the one from the absolute method, since the relative method is fluence independent. Therefore it is an ideal tool for direct comparison of two different sequences at a certain energy. Energy dependencies, on the other hand, can be studied only with the absolute method.

Comparing all determined strand break cross sections in this work, the dynamic range of the obtained values is rather small for similar sequences. The obtained strand break cross sections of all sequences range from  $4.35 \pm 0.38 \cdot 10^{-15} \text{ cm}^2$  (TeloM + K<sup>+</sup> at 10 eV) up to  $2.12 \pm 0.09 \cdot 10^{-14} \text{ cm}^2$  (5'-Bt-d(TT(<sup>2F</sup>AT<sup>2F</sup>A)<sub>3</sub>TT)-3' at 5.5 eV) exemplifying the high sensitivity of this method. Furthermore, when this method was used for similar experiments with photon irradiation, strand break cross sections of the order of  $10^{-16} \text{ cm}^2$  could be obtained.<sup>122</sup>

The influence of radiosensitizing modifications of the DNA nucleobases was investigated. A clear increase in DNA backbone cleavage was obtained for both F containing nucleobases <sup>2F</sup>A and <sup>5F</sup>U at 10 eV compared to their natural derivatives A and T. Both fluorinated oligonucleotides have identical cross sections at this energy. While no pronounced fragmentations occur in gas phase DEA experiments for those nucleobases, the F modification was found to increase the strand break cross sections in oligonucleotides. The special electronic properties of F may increase the probability of electron attachment with subsequent electron transfer to the DNA backbone, generating a DNA strand break without initial nucleobase fragmentation. This hypothesis is supported by the observation that neither the neighboring nucleobase (either A or T) nor the number of F modified nucleobases significantly influence the strand break cross

section. At 5.5 eV on the other hand, the strand break cross sections of  $^{2F}A$  containing oligonucleotide is almost twice as high as that of the  $^{5F}U$  containing sequence. While  $^{5F}U$  shows the same sensitivity towards 5.5 eV electrons as towards 10 eV, a clearly increased sensitivity was found for  $^{2F}A$  and its natural derivative A. Since all four nucleobases showed DEA resonances at 5.5 eV in gas phase experiments, the origin of the increased sensitivity in A and  $^{2F}A$  is still not entirely clear. It might result from the nature of the generated fragments itself, since the fragmentation of the nucleobase does not necessarily lead to DNA backbone cleavage. The unique fragments  $(^{2F}A-H-F)^-$  and  $(^{2F}A-2H-F)^-$  that are dominant at 5.5 eV for  $^{2F}A$  seem to induce oligonucleotide strand breaks, while the small fragments for A and  $^{5F}U$  at 5.5 eV seem to induce DNA backbone cleavage only in A, but not in  $^{5F}U$ . Thus, the special electronic properties of F are not dominant at 5.5 eV, in contrast to the case of 10 eV, which is the dominant electron energy of secondary electrons during tissue radiation with high energy radiation.

The strand break cross sections for the telomere derived sequences reveal a clear length dependency, with increasing sensitivity for longer sequences. Furthermore, the increased sensitivity caused by G-stacking interactions could be confirmed, while the direction of the oligonucleotide proved to have no influence on the strand break cross section. With longer oligonucleotide sequences the probability of G-hairpin, G-triplex, and G-quadruplex folding increases, both in the presence of  $Mg^{2+}$  and additional  $K^+$ . With increasing probability of folded oligonucleotides, the strand breaks cross section decreases, suggesting either an increased stability of the sequence or a change in its electrical properties, leaving the strand less sensitive towards 10 eV electrons. While the latter aspect can be explained by the protected G-tetrads in the G-quadruplex, the first one results from the stability of the G-quadruplex itself and the unknown unfolding efficiency during the SA $\nu$  incubation. The results presented in this work indicate a slight influence of the folding pattern in the G-quadruplex, which might also influence the stability against unfolding, since intra- and intermolecular folded G-quadruplexes might vary in their stability as well. While these effects are rather small, the folding itself seems to have a rather strong influence. The strand break cross sections of the Telo4 sequence is similar with and without the presence of  $K^+$ . This can be attributed to an already folded sequence without  $K^+$  ions. For the Telo4G sequence on the other hand, a difference in the strand break cross sections caused by the presence of  $K^+$  was observed. Consequently, the telomere derived sequences show a clear change of sensitivity towards 10 eV LEEs in their folded compared to their unfolded state. The telomere sequences at the chromosome ends are folded and unfolded during different states of the cell reproductive

cycle. The obtained results obtained in this work may therefore suggest an optimum time for irradiation depending on the cell state.

In the present work the F modification is located only at the nucleobase. Since radiosensitizers such as Gemcitabine are very effective toward certain tumors, F modified sugars might influence the strand break cross sections as well, which could further confirm the hypothesis of the “F antenna” inducing DNA backbone cleavage without previous nucleobase fragmentation. In addition, different halo-modifications would be interesting to study in future experiments, since the electronic properties change drastically from F to Br. Furthermore, since first experiments presented in this work clearly indicate energy dependent strand break cross sections in oligonucleotides, this aspect should be studied further at various energies. Finally, additional experiments with dsDNA and higher-order topology forming sequences, such as the C rich i-motif, might be performed in the future, since the results obtained from the telomere derived sequences indicate a strong influence of the DNA topology.





Table 4. List of all modified sequences used during the experiments.

Biotin	Bt-	t-1s4/14/24i
ATA	Bt-TT(ATA) <sub>3</sub> TT-	t7s8/18/28g
<sup>2F</sup> AT <sup>2F</sup> A	Bt-TT( <sup>2F</sup> AT <sup>2F</sup> A) <sub>3</sub> TT-	t1s8/18/28i
<sup>5F</sup> UT <sup>5F</sup> U	Bt-TT( <sup>5F</sup> UT <sup>5F</sup> U) <sub>3</sub> TT-	t-5s8/18/28g
A <sup>5F</sup> UA	Bt-TT(A <sup>5F</sup> UA) <sub>3</sub> TT-	t1s8/18/28i
Telo2	Bt-TT(GGG ATT) <sub>2</sub> T-	t1s8/18/28i
Telo3	Bt-TT(GGG ATT) <sub>3</sub> T-	t7s8/18/28g
Telo4	Bt-TT(GGG ATT) <sub>4</sub> T-	t-5s8/18/28g
Telo2G	Bt-TT(GGG GTT) <sub>2</sub> T-	t7s8/18/28g
Telo4G	Bt-TT(GGG GTT) <sub>4</sub> T-	t1s8/18/28i
Telo2R	Bt-TT(TTA GGG) <sub>2</sub> T-	t-5s8/18/28g
Telo2M	Bt-(TGT GTG A) <sub>2</sub> T-	t1s8/18/28i
T <sub>12</sub>	Bt-T <sub>12</sub> -	t5s8/18/28g

Table 5. List of all staples used for target sequence positioning on the DNA origami.

t-5s8g	ACA AGA AAG CAA GCA AAT CAG ATA ACA GCC ATA TTA TTT A
t-5s18g	CCA AGC GCA GGC GCA TAG GCT GGC AGA ACT GGC TCA TTA T
t-5s28g	TTA ATG AAG TTT GAT GGT GGT TCC GAG GTG CCG TAA AGC A
t-1s4i	TTT AAC CTA TCA TAG GTC TGA GAG TTC CAG TA
t-1s14i	CAA CAG TTT ATG GGA TTT TGC TAA TCA AAA GG
t-1s24i	AGG AAG ATG GGG ACG ACG ACA GTA ATC ATA TT
t1s8i	ATG GTT TAT GTC ACA ATC AAT AGA TAT TAA AC
t1s18i	TTC GAG CTA AGA CTT CAA ATA TCG GGA ACG AG
t1s28i	CGA CCA GTA CAT TGG CAG ATT CAC CTG ATT GC
t5s8g	TTG ACG GAA ATA CAT ACA TAA AGG GCG CTA ATA TCA GAG A
t5s18g	TAA TTG CTT TAC CCT GAC TAT TAT GAG GCA TAG TAA GAG C
t5s28g	GAA TAC GTA ACA GGA AAA ACG CTC CTA AAC AGG AGG CCG A
t7s8g	CAC CGT CAC CTT ATT ACG CAG TAT TGA GTT AAG CCC AAT A
t7s18g	CGG ATG GCA CGA GAA TGA CCA TAA TCG TTT ACC AGA CGA C
t7s28g	CTA TTA GTA TAT CCA GAA CAA TAT CAG GAA CGG TAC GCC A

The staple strands were purchased from *IDT*. A stock solution containing 199 staple strands (all positions except t1s8/18/28i, t-5s8/18/28g, t7s8/18/28g) was prepared with 3  $\mu\text{L}$  each. For one preparation of DNA origami 29.85  $\mu\text{L}$  of this staple solution (199 x 0.15  $\mu\text{L}$ ) was added to 41.65  $\mu\text{L}$  deionized water (purified with a *MilliQ*). A buffer solution was prepared, containing 10 x TAE and 200 mM  $\text{MgCl}_2 \cdot 6 \text{H}_2\text{O}$ , both purchased from *Sigma Aldrich*. For one origami preparation 10  $\mu\text{L}$  of the buffer solution was added. Thus the concentration of buffer in the tube is 1 x TAE with 20 mM  $\text{MgCl}_2$ . Additionally, 5  $\mu\text{L}$  of m13mp18 (100 nM in 10 mM Tris and 1 mM EDTA), purchased from *NEB*, was added to the solution without further purification.

Finally the modified strands were added to the solution with 0.15  $\mu\text{L}$  each. Since each design contains only 3 x 2 modifications, the unmodified free positions were added with 0.15  $\mu\text{L}$  each as well (example: t1s8/18/28i, t-5s8/18/28g modified with Telo2 and Telo4, t7s8/18/28g unmodified original staple strands). For reducing pipetting errors due to the very small amounts of strand solutions, a mixture containing 1.5  $\mu\text{L}$  of each staple strand was prepared, diluted 10 times with deionized water, and used for 10 DNA origami preparations, adding always 13.5  $\mu\text{L}$  (9 x 1.5  $\mu\text{L}$ ) to the tube for DNA origami preparation.

For Bt and T<sub>12</sub> the design already contained the unmodified staple strands. Thus, the design was completed with all 208 unmodified staple strands and the three strands carrying Bt or T<sub>12</sub>, were added in 100 x excess (each 1.5  $\mu\text{L}$  pure modified strand solution). Since integration into the origami pattern is competitive, the modified strand is integrated with nearly 100 % probability.

For annealing the prepared solution containing staples, scaffold and buffer was heated up to 80 °C and cooled down stepwise over 2 h to 4 °C with a thermocycler from *PeqLab*. Subsequently, the annealed DNA origami triangle solution was transferred into a 0.5 mL Ultracel-100K centrifugal filter, purchased from *Amicon*. With the 5804 centrifuge from *eppendorf*, the filtration was done two times with 300  $\mu\text{L}$  1 x TAE buffer containing 20 mM  $\text{MgCl}_2$  with 6000 rpm for 5 minutes. The filtrate was isolated afterwards in a new tube with 7000 rpm over 2 minutes.

The silicon wafers, purchased from *CrysTec*, p-type, boron doped, (100) orientation, were cut into 8 x 8 mm<sup>2</sup> pieces, marked with a central cross (see chapter 7.2.1.2) and cleaned with air plasma from *diener scientific* for 5 minutes, directly before the DNA origami were adsorbed on the surface. From the freshly prepared origami solution one drop of 0.8  $\mu\text{L}$  was placed directly at the cross marker. To prevent drying effects, instantly afterwards 15  $\mu\text{L}$  of 10 x TAE with 200 mM  $\text{MgCl}_2$  buffer were added on top of the drop of DNA origami solution. The sample was incubated for 1 h at room temperature in an

incubation chamber containing water to maintain high humidity to prevent drying. Subsequently, the sample was cleaned once with 1 mL of 1:1 deionized water/ethanol (99 %, purchased from *Sigma Aldrich*), and instantly placed in 10 mL ethanol for 1 h. Afterwards, the sample was dried with air and mounted on the sample stage for irradiation. (Irradiation process see chapter 7.2).

The irradiated samples were unmounted from the sample stage and incubated with a 50 nM solution of streptavidin for 2 minutes. 0.1 g of SAV was purchased dry and diluted with 183  $\mu\text{L}$  of deionized water to a 10  $\mu\text{M}$  stock solution, which then was split into 10  $\mu\text{L}$  aliquots. One aliquot was diluted with 1990  $\mu\text{L}$  1 x TAE and 20 mM  $\text{MgCl}_2$  buffer down to 50 nM. The mixture was split into 200  $\mu\text{L}$  aliquots to prevent aging through repeated freezing and thawing. After 2 minutes of incubation the sample was rinsed with 0.5 mL 1:1 water/ethanol and dried with air. The origami analysis was done with an *Agilent 5500* AFM. At least one picture at each of the four marked cross segments was taken with 4 x 4  $\mu\text{m}^2$  size (1024 px/line, 1.0 second/line, tapping mode).

Overview: 10  $\mu\text{L}$  (10 x TAE + 200 mM  $\text{MgCl}_2$ ) buffer  
5  $\mu\text{L}$  m13mp18 (100 nM in 10 mM tris + 1 mM EDTA)  
29.85  $\mu\text{L}$  staple strand solution (199 x 0.15  $\mu\text{L}$ )  
41.65  $\mu\text{L}$   $\text{H}_2\text{O}$   
13.5  $\mu\text{L}$  modified staple solution (9 x 0.15  $\mu\text{L}$ , 10 x diluted)

Annealing 2 h with Thermocycler “Origami.cyc”  
Filtering 2 x with 300  $\mu\text{L}$  (1 x TAE + 20 mM  $\text{MgCl}_2$ ) buffer  
Adsorbing 1 h with (10 x TAE + 200 mM  $\text{MgCl}_2$ ) buffer  
Drying 1 h in ethanol  
Irradiation  
Labelling with SAV  
AFM

## 7.2. Chamber manual

### 1. Preparation

- 1.1. Start rough pump, blue valve closed (90° to tube)
- 1.2. Glue samples with Cu tape
  - 1.2.1. small vertical pieces
  - 1.2.2. precise sample alignment with markers
  - 1.2.3. check connection (Cu cable flexible)
- 1.3. Mount sample stage in vacuum chamber on upper DN100 flange
- 1.4. Close chamber
  - 1.4.1. Check Cu seal, change if position changed or notch to big
  - 1.4.2. Drive sample stage to highest position
- 1.5. Open blue valve slowly!
  - 1.5.1. From “Pressure over” to  $10^{-1}$  mbar very slow decrease in pressure
  - 1.5.2. Afterwards open valve completely
  - 1.5.3. If pressure detection is not shown on the controller, push “Measure” up to 3x
- 1.6. Start turbomolecular pump (at controller)
  - 1.6.1. Pressure [mbar], power [W] and speed [Hz] visible at the controller
  - 1.6.2. Final speed: 1010 Hz  
Target:  $10^{-6}$  mbar and 5-8 W  
If not: gas leak (check flanges) or chamber contaminated (clean)
- 1.7. Wait until  $10^{-8}$  mbar is reached (min. 3-4 hours, ideal: overnight)

### 2. Start Electronics

- 2.1. Start computer, check electron gun cables & connections
- 2.2. Switch on picoammperemeter “**PIA**” [Keithley 6485E]
  - 2.2.1. Start, push “ZCHK” when boot finished
- 2.3. Switch on power supply “**Shutter & ENG**” [VSP2653, Out A: Shutter, Out B: “ENG” voltage for electron energy]
  - 2.3.1. Shutter open: switch green pos.  
Shutter closed: red pos. (& green light)
  - 2.3.2. Avoid pos. in between both (shutter will charge)
  - 2.3.3. **Shutter**: 14 V c.v.; **ENG**: 12 V c.v. (for 10 eV irradiation, otherwise  $x$  eV + 2V [for Si charging])
- 2.4. Switch on power supply “**EXT**” [EA-PS 5200-02A, extractor lens]
  - 2.4.1. Set 65.0 V c.v., push “On”
- 2.5. Switch on digital multimeter “**EMS**” [Voltcraft VC175 in  $\mu$ A mode, current of filament emission]
- 2.6. Switch on power supply “**ANO & FIL**” [GPD-2303S: CH1: “**FIL**” filament current, CH2: “**ANO**” defocusing electrostatic lens voltage]

- 2.6.1. “**FIL**” current at 0.0A!, “**ANO**”: 1.5V c.v. (for 10 eV)
- 2.6.2. Push “Output” (lights blue)
- 2.6.3. Increase “**FIL**” current +0.1A/30s up to 1.5A c.c.
- 2.6.4. Increase “**FIL**” current up to 2.1A c.c. while avoiding pressures above (max.  $1 \times 10^{-7}$  mbar) (slower than 2.6.3.)
- 2.6.5. Warm up filament for 30min sharp with 2.1A c.c.
- 2.7. Computer/Desktop/Messdaten/”create new folder”
  - 2.7.1. Folder name: YearMonthDay (e.g. 150603)
  - 2.7.2. Copy program from desktop to folder
    - 2.7.2.1. *PIA single*: one measurement of irradiation current
    - 2.7.2.2. *PIA single F*: one measurement with fluence calculation
    - 2.7.2.3. *PIA all*: 8 measurements of irradiation in one file
    - 2.7.2.4. *PIA all F*: 8 measurements with fluence calculation
    - 2.7.2.5. *PIA Beam*: program for beam profile measurement
    - 2.7.2.6. *PIA Calc*: calculator for irradiation times
  - 2.7.3. Run program from folder (double click)
  - 2.7.4. Follow program instructions
  - 2.7.5. When “Go?” appears, “enter” will start measurement

### 3. Irradiation

- 3.1. Close shutter (switch to red side)
- 3.2. Lower sample stage to height  $h = 31.6$  mm with free position oriented to electron gun
- 3.3. Open shutter (switch to green side) & start measurement in parallel
  - 3.3.1. For *PIA single*: run each irradiation separately with closed shutter in-between
  - 3.3.2. For *PIA all*: run all irradiations without closing the shutter in-between, 2 s time to change position
- 3.4. As soon as “Done” appears in program, close shutter

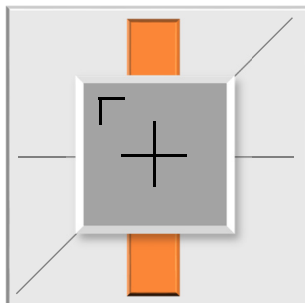
### 4. Post irradiation

- 4.1. Move sample stage to highest position
- 4.2. Reduce “**FIL**” to 0, switch off “Output”
- 4.3. Switch off “**ANO & FIL**”
- 4.4. Push “Off” at “**EXT**”, switch off when  $< 5$  V
- 4.5. Open “**Shutter**” (green)
- 4.6. Switch off “**Shutter & ENG**”
- 4.7. Switch off “**PIA**”
- 4.8. Copy files, switch off computer
- 4.9. Wait 1 hour (filament cool down time)
- 4.10. Stop turbopump (push “stop”), close blue valve

- 4.11. Wait until "... Hz" is reached (speed to 0)
- 4.12. Open gas valve carefully
  - 4.12.1. +1/2 turn in 30 minutes (2 turns total)
  - 4.12.2. Wait until controller shows "Pressure Over" and no air flow at gas valve is detectable
- 4.13. Close gas valve to original position (not beyond! otherwise the sapphire sealings will be destroyed)
- 4.14. Open chamber at upper DN100 flange with sample stage
- 4.15. Remove sample stage
- 4.16. Remove samples (and Cu-tape, if necessary)
- 4.17. Remount sample stage on flange and close chamber
- 4.18. Evacuate chamber (even without samples, to keep the system clean)
- 4.19. Go on with sample preparation (SAv incubation)



Rack with electronic devices.



Step 1.2. One side of the sample stage with sample on Cu-tape.



Step 1.6. Turbomolecular pump and pressure gauge controller.

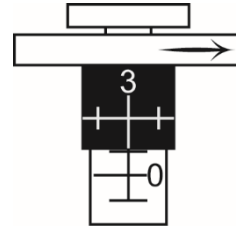


Step 2.1. Computer.

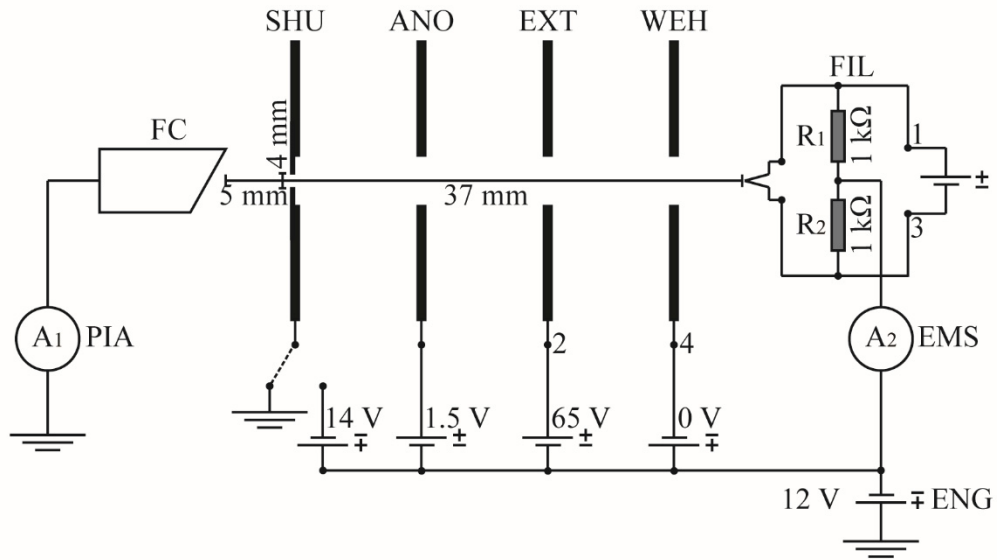
Step 2.2. Picoamperemeter **PIA**.Step 2.3. Power supply **Shutter and ENG.**Step 2.4. Power supply **EXT.**Step 2.5. Digital multimeter **EMS.**Step 2.6. Power supply **ANO and FIL.**



Tungsten hairpin filament inside the electron gun.



Gas valve in the closed position.



Schematic drawing of the circuit of the electron gun.

### 7.3. Software

Keithley's Picoamperemeter 6485E measures the current at the sample stage and sends the data to the computer with win XP. A small program in different versions written in Python 2.7 lists the data in a text file.

This manual will explain the program in its different versions. Based on the simplest option "PIA Single" the program steps will be discussed, with additional explanations for the extended versions.

#### "PIA Single.py"

The least complex version of the program is collecting the data of one measurement. First, the program imports the necessary libraries to communicate in SCPI with the picoamperemeter (PIA) (line 04) and different small programs for time and mathematics (line 05-07). Then a first request for communication (line 09-11) checks the connection. "ASRL9" defines the USB port and needs to be changed if the USB port is changed. Subsequently, the picoamperemeter is calibrated and set to measure one point per second (line 13-24). The first input from the user is then needed (line 27), where the file name needs to be defined, followed by an input request of the measurement time (line 31). The measurement is independent of the shutter and thus, the irradiation of the sample. Therefore, the software needs to be started in parallel with switching the shutter. If this process is done properly, the measurement time is identical with the irradiation time.

The file is then created with date, name and time of measurement (line 34-38). Only then the real measurement starts with a loop, repeating every second (line 40-49). Here, the input of measurement time defines the number of cycles the program will run. In each run, the picoamperemeter will measure and save one current value. Then, this value is sent to the computer and saved in the text file by the program. Additionally, the value is displayed in the window of cmd.exe (which runs "PIA Single.py"). A faster loop repetition is not advisable, since the communication between the PIA and the computer is rather slow and can create data accumulation, which leads to an error in the PIA data cache and thus, interrupt the measurement). After finishing the loop, the user will be informed by the message "Done" (line 51), the text file will be closed (line 54) and the window of cmd.exe will stay open until the user presses "enter", when "Close?" appears (line 56).

```
1 # 2015/03/03, Jenny
2 # * PIA *
3
4 import visa
5 import time
6 import datetime
7 import math
8
9 # identify picoamp, ASRL depends on USBport
10 keithley = visa.instrument("ASRL9")
11 print keithley.ask ("*IDN?")
12
13 # Calibrate Pico AMP
14 keithley.write("*RST")
15 keithley.write("SYST:ZCH ON")
16 keithley.write("CURR:RANG 2E-9")
17 keithley.write("INIT")
18 keithley.write("SYST:ZCOR ON")
19 keithley.write("CURR:RANG:AUTO ON")
20 keithley.write("SYST:ZCH OFF")
21 keithley.write("FORM:ELEM READ")
22 keithley.write("TRIG:COUN 1")
23 keithley.write("TRAC:POIN 1")
24 keithley.write("TRAC:FEED SENS")
25
26 #define File name
27 var=raw_input("File name: ")
28
29 #define n (measurement time in s)
30 int=input("measurement time in s: ")
31 n=(int)
32
33 # Open a file
34 d = datetime.date.fromtimestamp(time.time())
35 timestamp = "" + str(d.year) + "-" + str(d.month)
36 + "-" + str(d.day)
37 fo = open("data_" + timestamp + "_" + str(var)
38 + ".txt", "wt")
39 fo.write(timestamp + "\n")
40 fo.write("t=" + str(n) + "s" + "\n" + "\n"
41 + "Current[A]" + "\n")
```

```
40     # Measure current every second
41     for x in range(0,n):
42         keithley.write("TRAC:FEED:CONT NEXT")
43         time.sleep(0.3)
44         keithley.write("INIT")
45         time.sleep(0.2)
46         result = keithley.ask("TRAC:DATA?")
47         print result
48         fo.write(result + "\n")
49         time.sleep(0.3)
50
51     print "Done!"
52
53     # Close opened file
54     fo.close()
55
56     raw_input "Close?"
```

The text file containing the date, the measurement time (t), and the detected current in ampere (Current [A]) will look like this.

```
2015-10-14
t=10s

Current [A]
-3.152511E-09
-3.161357E-09
-3.130007E-09
-3.110713E-09
-3.114914E-09
-3.083125E-09
-3.071394E-09
-3.058464E-09
-3.044301E-09
-3.040817E-09
```

### “PIA Single F.py”

A modified version of “PIA Single.py” directly calculates the fluence in the central area, based on the percentage of the absolute current in this area. The central area is defined as a circle with 0.5 mm radius (line 39b), which corresponds to the size of the aperture for beam profile characterization (see chapter 3.3). The percentage depends on the beam profile, and may thus change during filament aging. At present, 6 % of the total current illuminate the sample at the central area (line 39c). For each current value, the fluence in this area is calculated for one second intervals (line 48b) and saved in the text file after the corresponding current. Finally, the sum over all fluence values (line 48d) is saved in the text file (line 52a) and displayed in the window of cmd.exe (line 52c).

```

38     fo.write("t=" + str(n) + "s" + "\n")

39a     #define beam radius in cm and central area in %/100
39b     r=0.05
39c     A=0.06
39d     fo.write("central radius:" + str(r) + "cm" + "\n"
+ "central part of the current:" + str(A) + "\n" + "\n")
39e     fo.write("Current[A]" + "\t" + "Fluence [1/cm^2 *e13]"
+ "\n")
39f
39g     #create sum for fluence
39h     sum=0

48         fo.write(result + "\t")
48a         a=float(result)
48b         F=abs(a)*A*(6.24*10**18/math.pi)*(1/r**2)*(10**-13)
48c         fo.write(str(F) + "\n")
48d         sum=sum + F

52a     fo.write("\n" + "total Fluence" + "\t" + str(sum)
+ "\t" + "1/cm^2 *e13")
52b     print "total Fluence in e13/cm^2:"
52c     print (sum)

```

The resulting text file will contain the values for the radius and the percentage of the current, which are used for the fluence calculation. The two columns with current and fluence for each one second interval is listed, followed by the total fluence in the central area.

```
2015-10-14
t=10s
central radius:0.05cm
central part of the current:0.06

Current[A]          Fluence [1/cm^2 *e13]
-2.902922E-09       0.0138382548808
-2.893579E-09       0.0137937167171
-2.888189E-09       0.0137680225393
-2.888804E-09       0.0137709542498
-2.890306E-09       0.0137781142971
-2.902386E-09       0.0138356997640
-2.881092E-09       0.0137341910775
-2.893545E-09       0.0137935546388
-2.889921E-09       0.0137762789987
-2.888643E-09       0.0137701867613

total Fluence       0.137858973924    1/cm^2 *e13
```

### “PIA All.py”

In case all samples shall be irradiated without closing the shutter, “PIA All.py” can be used. The software asks for eight irradiation times (line 35-52). The ideal setup will be first the empty position in the beginning, six irradiations afterwards, then one sample non-irradiated, which will be skipped, and finally the empty position again. The measurement starts as soon as the user presses “Enter” after “Go?” appears in the window of cmd.exe (line 54). The script works like the one for the single measurement “PIA singly.py”, only instead of one loop, eight separate loops will run after each other with a two second pause to change position. (line 72-85).

```

1      # 2015/03/03, Jenny
2      # * PIA *
3
4      import visa
5      import time
6      import datetime
7      import math
8
9      # identify picoamp, ASRL depends on USBport
10     keithley = visa.instrument("ASRL9")
11     print keithley.ask ("*IDN?")
12
13     # Calibrate Pico AMP
14     keithley.write("*RST")
15     keithley.write("SYST:ZCH ON")
16     keithley.write("CURR:RANG 2E-9")
17     keithley.write("INIT")
18     keithley.write("SYST:ZCOR ON")
19     keithley.write("CURR:RANG:AUTO ON")
20     keithley.write("SYST:ZCH OFF")
21     keithley.write("FORM:ELEM READ")
22     keithley.write("TRIG:COUN 1")
23     keithley.write("TRAC:POIN 1")
24     keithley.write("TRAC:FEED SENS")
25
26     #define File name
27     var=raw_input("File name: ")
28     print ""
29     print "I'm taking care of your measurement,"
30     print "you have 2 seconds for changing positions
31     between your samples!"
32     print "Be Quick! Good Luck!"
33     print ""
34     time.sleep(1)
35
36     #define n (measurement time in s)
37     print "Enter time [s] for positions 1-8"
38     int=input("1: ")
39     m = (int)
40     int=input("2: ")
41     n = (int)
42     int=input("3: ")
43     o = (int)

```

```
43     int=input("4: ")
44     p = (int)
45     int=input("5: ")
46     q = (int)
47     int=input("6: ")
48     r = (int)
49     int=input("7: ")
50     s = (int)
51     int=input("8: ")
52     t = (int)
53
54     raw_input("Go?")
55
56     # Open a file
57     d = datetime.date.fromtimestamp(time.time())
58     timestamp = "" + str(d.year) + "-" + str(d.month) + "-"
59     + str(d.day)
60     fo = open("data_" + timestamp + "_" + str(var) + ".txt",
61             "wt")
62     fo.write(timestamp + "\n")
63     fo.write("Position times [s]" + "\n")
64     fo.write("1: " + str(m) + "\n")
65     fo.write("2: " + str(n) + "\n")
66     fo.write("3: " + str(o) + "\n")
67     fo.write("4: " + str(p) + "\n")
68     fo.write("5: " + str(q) + "\n")
69     fo.write("6: " + str(r) + "\n")
70     fo.write("7: " + str(s) + "\n")
71     fo.write("8: " + str(t) + "\n")
72     fo.write("\n" + "Current[A]" + "\n")
73
74     for x in range(0,m):
75         keithley.write("TRAC:FEED:CONT NEXT")
76         time.sleep(0.3)
77         keithley.write("INIT")
78         time.sleep(0.2)
79         result = keithley.ask("TRAC:DATA?")
80         print result
81         fo.write(result + "\n")
82         time.sleep(0.3)
83
84     fo.write(".....next....." + "\n")
85     print "Pause"
```

```

84     time.sleep(2)
85
...repeated Line 72-85 from m to t (8 times) with modified
variable in Line 72...
174     print "Done!"
175
176     # Close opened file
177     fo.close()
178
179     raw_input("Close?")

```

All data will be saved in the same text file, separated by one line “.....next.....”.

```

2015-10-14
Position times [s]
1: 2
2: 2
3: 2
4: 2
5: 2
6: 2
7: 2
8: 2

Current[A]
-2.890219E-09
-2.889718E-09
.....next.....
[repeated for all 8 measurements]

```

### “PIA All F.py”

There is, as well as for “PIA Single.py”, an alternative, which directly calculates the fluence for each irradiation. As in “PIA All.py” eight separate measurement cycles will be done. The fluence calculation for each measurement is based on “PIA Single F.py”. Again, the calculation uses 0.5 mm radius and 6 % of the total current to determine the fluence in the central area (line 34e-f, 79b).

```

34a  #check central beam radius R and central beam current I
34b  print "Fluence calculation based on:"
34c  print "2015/08/06: r=0.05cm & I=0.06"
34d  print ""
34e  R=0.05
34f  I=0.06
34g  time.sleep(1)

61a  fo.write("central beam radius: " + str(R) + "cm" + "\n")
61b  fo.write("central part of the current: " + str(A) + "\n"
+ "\n")
61c  fo.write("Position times [s]" + "\n")

70   fo.write("\n" + "Current[A]" + "\t" + "Fluence [1/cm^2
*e13]" + "\n")

72a  #create sum for fluence nrl
72b  sum=0
72c  for x in range(0,m):

79      fo.write(result + "\t")
79a     a=float(result)
79b     F=abs(a)*A*(6.24*10**18/math.pi)*(1/r**2)*(10**-13)
79c     fo.write(str(F) + "\n")
79d     sum=sum + F

82a  fo.write("\n" + "total fluence" + "\t" + str(sum)
+ "\t" + "1/cm^2 *e13")
82b  fo.write(".....next....." + "\n")

...repeated Line 72-85 from m to t (8 times) with modified
variable in Line 72...

```

The corresponding text file contains the parameters for fluence calculation, followed by the measurement time for each position and in two columns the current and the resulting fluence for each one second interval. The total fluence for one measurement is displayed below. Afterwards, one blank line and “.....next.....” separates the different measurements.

```

2015-10-14
central beam radius: 0.05cm
central part of the current: 0.06

Position times [s]
1: 3
2: 3
[...]
7: 3
8: 3

Current[A]          Fluence [1/cm^2 *e13]
-3.243223E-09      0.0154604727613
-3.210751E-09      0.0153056784498
-3.204607E-09      0.0152763899474

total fluence      0.0460425411585      1/cm^2 *e13

.....next.....
-3.194412E-09      0.0152277902921
-3.195518E-09      0.0152330626039
-3.191951E-09      0.0152160586833

total fluence      0.0456769115793      1/cm^2 *e13

[...]

.....next.....
-3.192248E-09      0.0152174744849
-3.181229E-09      0.0151649468143
-3.178439E-09      0.0151516468596

total fluence      0.0455340681588      1/cm^2 *e13

.....next.....
-3.170359E-09      0.0151131294281
-3.170529E-09      0.0151139398196
-3.168250E-09      0.0151030758064

total fluence      0.0453301450541      1/cm^2 *e13

```

**“PIA Beam.py”**

This program is used for beam profile characterization (see chapter 3.2). The program starts with the same identification and calibration as “PIA Single.py” and all modifications. Instead of asking for the measurement time, this program has a fixed time of 15 seconds. Here, the user has to define the number of points. This value defines how often the measurement of 15 seconds is repeated (line 30-33). Each point is one height position of the faraday cup sample stage. Thus, the user has to define the height variation between two steps and the total height to analyze, to calculate the total amount of points to measure. Between each height value and measurement period, a pause of 15 seconds is implemented (line 61), to move the sample stage by one height increment. Additionally, this pause is necessary to stabilize the current measurement after sample stage movement. The text file will list all current values, each set of values for one point separated by one line with “.....next.....” (line 59).

```

...Begin is identically with "PIA Single"...

30     #define m (points)
31     int=input("points:")
32     m=(int)
33     n=15
34
35     print ""
36     print "Each point contains 15 seconds measurement,"
37     print "followed by 15 seconds pause to change position"
38     print ""
39     time.sleep(1)
40     raw_input("Go?")

..."Open a file" is identically with "PIA Single"...

48     #repeat loop for m points (loop: 15 points/15 seconds)
49     for y in range (0,m):
50         for x in range(0,n):
51             keithley.write("TRAC:FEED:CONT NEXT")
52             time.sleep(0.3)
53             keithley.write("INIT")
54             time.sleep(0.2)
55             result = keithley.ask("TRAC:DATA?")
56             print result
57             fo.write(result + "\n")

```

```

58         time.sleep(0.3)
59         fo.write(".....next....." + "\n")
60         print "Pause"
61         time.sleep(15)

```

*...End is identically with "PIA Single"...*

### “PIA Calc.py”

In case a sample has to be irradiated with a certain fluence, the calculator “PIA Calc.py” can be used. Based on the desired fluence at the central area (line 15) and the total current (line 11) the irradiation time is calculated. Therefore, the radius of the central area is defined as 0.5 mm (line 9). Further, the percentage of the current of the central area has to be defined by the user (line 13). The resulting irradiation time is displayed in the window of cmd.exe (which runs “PIA Calc.py”) (line 21).

```

1     # -*- coding: cp1252 -*-
2     # 2015/10/13, Jenny
3     # * Ircal V2 *
4     import math
5
6     #Fluence calculator for central beam diameter 1mm
7
8     # define fluence, current & beam radius [cm]
9     r=0.05
10    int=input("PIA current [nA]:" + "\n")
11    I=(int)
12    int=input("Central part [%]:" + "\n")
13    A=(int)
14    int=input("Fluence [e13/cm^2]:" + "\n")
15    F=(int)
16
17    # calculate irradiation time
18    a=(F*10**13*math.pi*r**2)/(6.24*10**9*I*A*10**(-2))
19    t=round(float(a), 2)
20    print "Irradiation time in s:"
21    print (t)
22    print ""
23    raw_input("Close?")

```

When executed, the window of cmd.exe will show the following lines.

```
PIA current [nA]:  
3  
Central part [%]:  
6  
Fluence [e13/cm^2]:  
2  
Irradiation Time in s:  
139.85  
  
Close?
```

#### 7.4. Ratios between the natural and F modified oligonucleotide sequences in chapter 4

Table 6. Ratios of the strand break cross sections of the fluorinated oligonucleotide sequences studied in chapter 4.

5'-Bt- d(TT <sub>X</sub> TT)-3'	10 eV (ATA) <sub>3</sub>	10 eV ( <sup>2</sup> FAT <sup>2</sup> FA) <sub>3</sub>	10 eV ( <sup>5</sup> FUT <sup>5</sup> FU) <sub>3</sub>	10 eV (A <sup>5</sup> FUA) <sub>3</sub>	10 eV T <sub>8</sub>	5.5 eV (ATA) <sub>3</sub>	5.5 eV ( <sup>2</sup> FAT <sup>2</sup> FA) <sub>3</sub>	5.5 eV ( <sup>5</sup> FUT <sup>5</sup> FU) <sub>3</sub>
10 eV (ATA) <sub>3</sub>	-	0.6 ± 0.2	0.6 ± 0.2	0.6 ± 0.2	1.0 ± 0.2	0.6 ± 0.1	0.4 ± 0.1	0.7 ± 0.2
10 eV ( <sup>2</sup> FAT <sup>2</sup> FA) <sub>3</sub>	1.7 ± 0.5	-	1.0 ± 0.4	1.1 ± 0.4	1.7 ± 0.4	1.0 ± 0.2	0.6 ± 0.1	1.2 ± 0.3
10 eV ( <sup>5</sup> FUT <sup>5</sup> FU) <sub>3</sub>	1.6 ± 0.5	1.0 ± 0.3	-	1.1 ± 0.4	1.7 ± 0.5	1.0 ± 0.2	0.6 ± 0.1	1.1 ± 0.3
10 eV (A <sup>5</sup> FUA) <sub>3</sub>	1.5 ± 0.5	0.9 ± 0.3	0.9 ± 0.3	-	1.5 ± 0.4	0.9 ± 0.2	0.6 ± 0.1	1.0 ± 0.3
10 eV T <sub>8</sub>	1.0 ± 0.2	0.6 ± 0.2	0.6 ± 0.2	0.7 ± 0.2	-	0.6 ± 0.1	0.4 ± 0.1	0.7 ± 0.1
5.5 eV (ATA) <sub>3</sub>	1.7 ± 0.3	1.0 ± 0.2	1.0 ± 0.2	1.1 ± 0.2	1.7 ± 0.2	-	0.6 ± 0.0	1.2 ± 0.1
5.5 eV ( <sup>2</sup> FAT <sup>2</sup> FA) <sub>3</sub>	2.6 ± 0.5	1.6 ± 0.3	1.6 ± 0.4	1.8 ± 0.4	2.7 ± 0.4	1.6 ± 0.1	-	1.8 ± 0.3
5.5 eV ( <sup>5</sup> FUT <sup>5</sup> FU) <sub>3</sub>	1.5 ± 0.4	0.9 ± 0.2	0.9 ± 0.2	1.0 ± 0.3	1.5 ± 0.3	0.9 ± 0.1	0.6 ± 0.1	-



## References

1. American Cancer Society. *Cancer Facts & Figures 2015* (Atlanta, GA, 2015).
2. World Health Organization. Fact Sheets by Cancer 2012. Available at [http://globocan.iarc.fr/Pages/fact\\_sheets\\_cancer.aspx](http://globocan.iarc.fr/Pages/fact_sheets_cancer.aspx).
3. National Cancer Institute. What is Cancer? Available at <http://www.cancer.gov/about-cancer/what-is-cancer>.
4. National Cancer Institute. Cancer Risks. Available at <http://www.cancer.gov/about-cancer/causes-prevention/risk>.
5. Hajdu, S. I., Vadmal, M. & Tang, P. A note from history: Landmarks in history of cancer, part 7. *Cancer* **121**, 2480–2513 (2015).
6. Grodstein, F., Newcomb, P. A. & Stampfer, M. J. Postmenopausal hormone therapy and the risk of colorectal cancer. A review and meta-analysis. *Am. J. Med.* **106**, 574–582 (1999).
7. American Cancer Society. Cancer Immunotherapy. Available at <http://www.cancer.org/acs/groups/cid/documents/webcontent/003013-pdf.pdf>.
8. Dudley, M. E., Wunderlich, J. R., Robbins, P. F., Yang, J. C., Hwu, P., Schwartzentruber, D. J., Topalian, S. L., Sherry, R., Restifo, N. P., Hubicki, A. M., Robinson, M. R., Raffeld, M., Duray, P., Seipp, C. A., Rogers-Freezer, L., Morton, K. E., Mavroukakis, S. A., White, D. E. & Rosenberg, S. A. Cancer regression and autoimmunity in patients after clonal repopulation with antitumor lymphocytes. *Science* **298**, 850–854 (2002).
9. Morgan, R. A., Dudley, M. E., Wunderlich, J. R., Hughes, M. S., Yang, J. C., Sherry, R. M., Royal, R. E., Topalian, S. L., Kammula, U. S., Restifo, N. P., Zheng, Z., Nahvi, A., Vries, C. R. de, Rogers-Freezer, L. J., Mavroukakis, S. A. & Rosenberg, S. A. Cancer regression in patients after transfer of genetically engineered lymphocytes. *Science* **314**, 126–129 (2006).
10. Hajdu, S. I. & Vadmal, M. A note from history: Landmarks in history of cancer, Part 6. *Cancer* **119**, 4058–4082 (2013).

11. Arumainayagam, C. R., Lee, H.-L., Nelson, R. B., Haines, D. R. & Gunawardane, R. P. Low-energy electron-induced reactions in condensed matter. *Surf. Sci. Rep.* **65**, 1–44 (2010).
12. Boudaiffa, B., Cloutier, P., Hunting, D., Huels, M. A. & Sanche, L. Resonant formation of DNA strand breaks by low-energy (3 to 20 eV) electrons. *Science* **287**, 1658–1660 (2000).
13. Sancar, A., Lindsey-Boltz, L. A., Ünsal-Kaçmaz, K. & Linn, S. Molecular mechanisms of mammalian DNA repair and the DNA damage checkpoints. *Annu. Rev. Biochem.* **73**, 39–85 (2004).
14. Seiwert, T. Y., Salama, J. K. & Vokes, E. E. The concurrent chemoradiation paradigm-general principles. *Nat. Clin. Pract. Onc.* **4**, 86–100 (2007).
15. Gregoire, V., Beauduin, M., Bruniaux, M., Coster, B. de, Octave Prignot, M. & Scalliet, P. Radiosensitization of mouse sarcoma cells by Fludarabine (F-ara-A) or gemcitabine (dFdC), two nucleoside analogues, is not mediated by an increased induction or a repair inhibition of DNA doublestrand breaks as measured by pulsed-field gel electrophoresis. *Int. J. Radiat. Biol.* **73**, 511–520 (1998).
16. Bald, I., Kopyra, J., König, C., Flosadottir, H. D., Ingolfsson, O. & Illenberger, E. Low energy (0–12 eV) electron interaction with gas phase building blocks of DNA/RNA. *J. Phys.: Conf. Ser.* **115**, 012008-1–012008-9 (2008).
17. Abdoul-Carime, H., Langer, J., Huels, M. A. & Illenberger, E. Decomposition of purine nucleobases by very low energy electrons. *Eur. Phys. J. D* **35**, 399–404 (2005).
18. Huber, D., Beikircher, M., Denifl, S., Zappa, F., Matejcik, S., Bacher, A., Grill, V., Märk, T. D. & Scheier, P. High resolution dissociative electron attachment to gas phase adenine. *J. Chem. Phys.* **125**, 084304-1–084304-7 (2006).
19. Denifl, S., Ptasíńska, S., Probst, M., Hrušák, J., Scheier, P. & Märk, T. D. Electron Attachment to the Gas-Phase DNA Bases Cytosine and Thymine. *J. Phys. Chem. A* **108**, 6562–6569 (2004).
20. Minaev, B. F., Shafranyosh, M. I., Svida, Y. Y., Sukhoviya, M. I., Shafranyosh, I. I., Baryshnikov, G. V. & Minaeva, V. A. Fragmentation of the adenine and guanine molecules induced by electron collisions. *J. Chem. Phys.* **140**, 175101-1–175101-15 (2014).

21. Kopyra, J., Keller, A. & Bald, I. On the role of fluoro-substituted nucleosides in DNA radiosensitization for tumor radiation therapy. *RSC Adv.* **4**, 6825–6829 (2014).
22. Zheng, Y., Cloutier, P., Hunting, D. J., Wagner, J. R. & Sanche, L. Glycosidic Bond Cleavage of Thymidine by Low-Energy Electrons. *J. Am. Chem. Soc.* **126**, 1002–1003 (2004).
23. Li, Z., Cloutier, P., Sanche, L. & Wagner, J. R. Low-Energy Electron-Induced DNA Damage. Effect of Base Sequence in Oligonucleotide Trimers. *J. Am. Chem. Soc.* **132**, 5422–5427 (2010).
24. Rothemund, P. W. K. Folding DNA to create nanoscale shapes and patterns. *Nature* **440**, 297–302 (2006).
25. Keller, A., Bald, I., Rotaru, A., Cauët, E., Gothelf, K. V. & Besenbacher, F. Probing Electron-Induced Bond Cleavage at the Single-Molecule Level Using DNA Origami Templates. *ACS Nano* **6**, 4392–4399 (2012).
26. Neidle, S. & Parkinson, G. N. The structure of telomeric DNA. *Curr. Opin. Struct. Biol.* **13**, 275–283 (2003).
27. Neidle, S. & Parkinson, G. Telomere maintenance as a target for anticancer drug discovery. *Nat. Rev. Drug. Discov.* **1**, 383–393 (2002).
28. Dahm, R. Friedrich Miescher and the discovery of DNA. *Dev. Biol.* **278**, 274–288 (2005).
29. Watson, J. D. & Crick, F. H. C. Molecular Structure of Nucleic Acids. A Structure for Deoxyribose Nucleic Acid. *Nature* **171**, 737–738 (1953).
30. Pearson, H. Genetics: what is a gene? *Nature* **441**, 398–401 (2006).
31. Saenger, W. *Principles of nucleic acid structure*. 4th ed. (Springer, New York, Berlin, Heidelberg, London, Paris, Tokyo, Hong Kong, Barcelona, Budapest, 1995).
32. Shui, X., McFail-Isom, L., Hu, G. G. & Williams, L. D. The B-DNA Dodecamer at High Resolution Reveals a Spine of Water on Sodium. *Biochemistry* **37**, 8341–8355 (1998).
33. Thota, N., Li, X. H., Bingman, C. & Sundaralingam, M. High resolution refinement of the hexagonal A-DNA octamer D(GTGTACAC) at 1.4 Angstroms resolution. *Acta Crystallogr., Sect. D* **49**, 282–291 (1993).

34. Leslie, A., Arnott, S., Chandrasekaran, R. & Ratliff, R. L. Polymorphism of DNA double helices. *J. Mol. Biol.* **143**, 49–72 (1980).
35. Griffiths, A. J. F. *An introduction to genetic analysis*. 7th ed. (Freeman, New York, 2002).
36. Slack, J. *Genes: A Very Short Introduction* (Oxford University Press, Oxford, 2014).
37. Blackburn, E. H. Telomeres: No end in sight. *Cell* **77**, 621–623 (1994).
38. Rhodes, D. & Giraldo, R. Telomere structure and function. *Curr. Opin. Struct. Biol.* **5**, 311–322 (1995).
39. Orr, D. C., Figueiredo, H. T., Mo, C. L., Penn, C. R. & Cameron, J. M. DNA chain termination activity and inhibition of human immunodeficiency virus reverse transcriptase by carbocyclic 2',3'-didehydro-2',3'-dideoxyguanosine triphosphate. *J. Biol. Chem.* **267**, 4177–4182 (1992).
40. Turner, M. A., Yang, X., Yin, D., Kuczera, K., Borchardt, R. T. & Howell, P. L. Structure and function of S-adenosylhomocysteine hydrolase. *Cell Biochem. Biophys.* **33**, 101–125 (2000).
41. Kitade, Y., Kozaki, A., Miwa, T. & Nakanishi, M. Synthesis of base-modified noraristeromycin derivatives and their inhibitory activity against human and *Plasmodium falciparum* recombinant S-adenosyl-l-homocysteine hydrolase. *Tetrahedron* **58**, 1271–1277 (2002).
42. Anderson, K. S. Perspectives on the molecular mechanism of inhibition and toxicity of nucleoside analogs that target HIV-1 reverse transcriptase. *Biochim. Biophys. Acta* **1587**, 296–299 (2002).
43. Maga, G. & Spadari, S. Combinations against combinations: associations of anti-HIV 1 reverse transcriptase drugs challenged by constellations of drug resistance mutations. *Curr. Drug Metab.* **3**, 73–95 (2002).
44. Pimblott, S. M. & LaVerne, J. A. Production of low-energy electrons by ionizing radiation. *Radiat. Phys. Chem.* **76**, 1244–1247 (2007).
45. International Commission on Radiation Units and Measurements. *ICRU Report* **31** (1979).

46. Huels, M. A., Boudaïffa, B., Cloutier, P., Hunting, D. & Sanche, L. Single, double, and multiple double strand breaks induced in DNA by 3-100 eV electrons. *J. Am. Chem. Soc.* **125**, 4467–4477 (2003).
47. Baccarelli, I., Bald, I., Gianturco, F. A., Illenberger, E. & Kopyra, J. Electron-induced damage of DNA and its components. Experiments and theoretical models. *Phys. Rep.* **508**, 1–44 (2011).
48. Bald, I., Langer, J., Tegeder, P. & Ingólfsson, O. From isolated molecules through clusters and condensates to the building blocks of life. *Int. J. Mass Spectrom.* **277**, 4–25 (2008).
49. Schulz, G. J. Resonances in Electron Impact on Diatomic Molecules. *Rev. Mod. Phys.* **45**, 423–486 (1973).
50. Allan, M. Study of triplet states and short-lived negative ions by means of electron impact spectroscopy. *J. Electron Spectrosc.* **48**, 219–351 (1989).
51. Hotop, H., Rul, M.-W. & Fabrikant, I. I. Resonance and Threshold Phenomena in Low-Energy Electron Collisions with Molecules and Clusters. *Phys. Scr.* **T110**, 22–31 (2004).
52. Rutherford, E. The scattering of particles by matter and the structure of the atom. *Philos. Mag.* **6**, 669–688 (1911).
53. Hofstadter, R. Electron Scattering and Nuclear Structure. *Rev. Mod. Phys.* **28**, 214–254 (1956).
54. Hertel, I. V. & Schulz, C.-P. *Atome, Moleküle und optische Physik 2* (Springer Berlin Heidelberg, Berlin, Heidelberg, 2010).
55. Meyne, J., Ratliff, R. L. & Moyzis, R. K. Conservation of the human telomere sequence (TTAGGG)<sub>n</sub> among vertebrates. *PNAS* **86**, 7049–7053 (1989).
56. Makarov, V. L., Hirose, Y. & Langmore, J. P. Long G tails at both ends of human chromosomes suggest a C strand degradation mechanism for telomere shortening. *Cell* **88**, 657–666 (1997).
57. Fernando, H., Reszka, A. P., Huppert, J., Ladame, S., Rankin, S., Venkitaraman, A. R., Neidle, S. & Balasubramanian, S. A conserved quadruplex motif located in a transcription activation site of the human c-kit oncogene. *Biochemistry* **45**, 7854–7860 (2006).

58. Cech, T. R. Life at the End of the Chromosome: Telomeres and Telomerase. *Angew. Chem. Int. Ed.* **39**, 34–43 (2000).
59. Blackburn, E. H. Switching and signaling at the telomere. *Cell* **106**, 661–673 (2001).
60. Bryan, T. M. & Cech, T. R. Telomerase and the maintenance of chromosome ends. *Curr. Opin. Cell Biol.* **11**, 318–324 (1999).
61. Greider, C. W. & Blackburn, E. H. Identification of a specific telomere terminal transferase activity in *Tetrahymena* extracts. *Cell* **43**, 405–413 (1985).
62. Kim, N., Piatyszek, M., Prowse, K., Harley, C., West, M., Ho, P., Coviello, G., Wright, W., Weinrich, S. & Shay, J. Specific association of human telomerase activity with immortal cells and cancer. *Science* **266**, 2011–2015 (1994).
63. Rezler, E. M., Bearss, D. J. & Hurley, L. H. Telomere inhibition and telomere disruption as processes for drug targeting. *Annu. Rev. Pharmacol.* **43**, 359–379 (2003).
64. Williamson, JR, Raghuraman, M. K. & Cech, T. R. Monovalent cation-induced structure of telomeric DNA: the G-quartet model. *Cell* **59**, 871–880 (1989).
65. Parkinson, G. N., Lee, M. P. H. & Neidle, S. Crystal structure of parallel quadruplexes from human telomeric DNA. *Nature* **417**, 876–880 (2002).
66. Adrian, M., Heddi, B. & Phan, A. T. NMR spectroscopy of G-quadruplexes. *Methods* **57**, 11–24 (2012).
67. Juskowiak, B. Analytical potential of the quadruplex DNA-based FRET probes. *Anal. Chim. Acta* **568**, 171–180 (2006).
68. Sannohe, Y., Endo, M., Katsuda, Y., Hidaka, K. & Sugiyama, H. Visualization of Dynamic Conformational Switching of the G-Quadruplex in a DNA Nanostructure. *J. Am. Chem. Soc.* **132**, 16311–16313 (2010).
69. Rajendran, A., Endo, M., Hidaka, K., Lan Thao Tran, P., Mergny, J.-L. & Sugiyama, H. Controlling the stoichiometry and strand polarity of a tetramolecular G-quadruplex structure by using a DNA origami frame. *Nucleic Acids Res.* **41**, 8738–8747 (2013).
70. Rajendran, A., Endo, M., Hidaka, K. & Sugiyama, H. Direct and Single-Molecule Visualization of the Solution-State Structures of G-Hairpin and G-Triplex Intermediates. *Angew. Chem. Int. Ed. Engl.* **126**, 4191–4196 (2014).

71. Wang, Y. & Patel, D. J. Solution structure of the human telomeric repeat dAG<sub>3</sub>(T<sub>2</sub>AG<sub>3</sub>)<sub>3</sub> G-tetraplex. *Structure* **1**, 263–282 (1993).
72. Markus, T. Z., Daube, S. S. & Naaman, R. Cooperative Effect in the Electronic Properties of Human Telomere Sequence. *J. Phys. Chem. B* **114**, 13897–13903 (2010).
73. Onoa, G. B., Cervantes, G., Moreno, V. & Prieto, M. J. Study of the interaction of DNA with cisplatin and other Pd(II) and Pt(II) complexes by atomic force microscopy. *Nucleic Acids Res.* **26**, 1473–1480 (1998).
74. Kopyra, J., Koenig-Lehmann, C., Bald, I. & Illenberger, E. A single slow electron triggers the loss of both chlorine atoms from the anticancer drug cisplatin: implications for chemoradiation therapy. *Angew. Chem. Int. Ed. Engl.* **48**, 7904–7907 (2009).
75. Reedijk, J. Platinum Anticancer Coordination Compounds. Study of DNA Binding Inspires New Drug Design. *Eur. J. Inorg. Chem.* **2009**, 1303–1312 (2009).
76. Malinge, J.-M., Giraud-Panis, M.-J. & Leng, M. Interstrand cross-links of cisplatin induce striking distortions in DNA. *J. Inorg. Biochem.* **77**, 23–29 (1999).
77. Bruso, C. E., Shewach, D. S. & Lawrence, T. S. Fluorodeoxyuridine-induced Radiosensitization and Inhibition of DNA Double Strand break repair in human colon cancer cells. *Int. J. Radiat. Oncol.* **19**, 1411–1417 (1990).
78. Abouaf, R., Pommier, J. & Dunet, H. Negative ions in thymine and 5-bromouracil produced by low energy electrons. *Int. J. Mass Spectrom.* **226**, 397–403 (2003).
79. Abdoul-Carime, H., Huels, M. A., Illenberger, E. & Sanche, L. Formation of negative ions from gas phase halo-uracils by low-energy (0–18 eV) electron impact. *Int. J. Mass Spectrom.* **228**, 703–716 (2003).
80. Chu, C. K., Ma, T. & Cheng, Y.-C. Use of 2'-Fluoro-5-Methyl-b-L-Arabinofuranosyluracil as a Novel Antiviral Agent for Hepatitis B Virus and Epstein-Barr Virus. *Antimicrob. Agents Ch.* **39**, 979–981 (1995).
81. Willis, M. C., Hicke, B. J., Uhlenbeck, O. C., Cech, T. R. & Koch, T. H. Photocrosslinking of 5-Iodouracil-substituted RNA and DNA to Proteins. *Science* **262**, 1255–1257 (1993).
82. Heidelberger, C., Danenberg, P. V. & Moran, R. G. Fluorinated pyrimidines and their nucleosides. *Adv. Enzymol. RAMB* **54**, 58–119 (1983).

83. Harbers, E., Chauduri, N. K. & Heidelberger, C. Studies on fluorinated pyrimidines. VIII. Further biochemical and metabolic investigations. *J. Biol. Chem.* **234**, 1255–1262 (1959).
84. Shewach, D. S. & Lawrence, T. S. Antimetabolite radiosensitizers. *J. Clin. Oncol.* **25**, 4043–4050 (2007).
85. Gumina, G., Schinazi, R. F. & Chu, C. K. Synthesis and potent anti-HIV activity of L-3'-fluoro-2',3'-unsaturated cytidine. *Org. Lett.* **3**, 4177–4180 (2001).
86. Chong, Y., Gumina, G., Mathew, J. S., Schinazi, R. F. & Chu, C. K. 1-2',3'-Didehydro-2',3'-dideoxy-3'-fluoronucleosides: synthesis, anti-HIV activity, chemical and enzymatic stability, and mechanism of resistance. *J. Med. Chem.* **46**, 3245–3256 (2003).
87. Zhou, W., Gumina, G., Chong, Y., Wang, J., Schinazi, R. F. & Chu, C. K. Synthesis, structure-activity relationships, and drug resistance of beta-d-3'-fluoro-2',3'-unsaturated nucleosides as anti-HIV Agents. *J. Med. Chem.* **47**, 3399–3408 (2004).
88. Lee, K., Choi, Y., Gumina, G., Zhou, W., Schinazi, R. F. & Chu, C. K. Structure-activity relationships of 2'-fluoro-2',3'-unsaturated D-nucleosides as anti-HIV-1 agents. *J. Med. Chem.* **45**, 1313–1320 (2002).
89. Huang, P., Robertson, L. E., Wright, S. & Plunkett, W. High molecular weight DNA fragmentation: a critical event in nucleoside analogue-induced apoptosis in leukemia cells. *Clin. Cancer Res.* **1**, 1005–1013 (1995).
90. Liu, P., Sharon, A. & Chu, C. K. Fluorinated Nucleosides: Synthesis and Biological Implication. *J. Fluorine Chem.* **129**, 743–766 (2008).
91. Duschinsky, R., Plevin, E. & Heidelberger, C. The Synthesis of 5-fluoropyrimidines. *J. Am. Chem. Soc.* **79**, 4559–4560 (1957).
92. Isanbor, C. & O'Hagan, D. Fluorine in medicinal chemistry: A review of anti-cancer agents. *J. Fluorine Chem.* **127**, 303–319 (2006).
93. Cozzarelli, N. R. The Mechanism of Action of Inhibitors of DNA Synthesis. *Annu. Rev. Biochem.* **46**, 641–668 (1977).
94. Keeney, R. E. & Buchanan, R. A. Clinical application of adenine arabinoside. *Ann. NY Acad. Sci.* **255**, 185–189 (1975).

95. Montgomery, J. A., Shortnacy-Fowler, A. T., Clayton, S. D., Riordan, J. M. & Secrist, J. 3. Synthesis and biologic activity of 2'-fluoro-2-halo derivatives of 9-beta-D-arabinofuranosyladenine. *J. Med. Chem.* **35**, 397–401 (1992).
96. Faderl, S., Gandhi, V. & Kantarjian, H. M. Potential role of novel nucleoside analogs in the treatment of acute myeloid leukemia. *Curr. Opin. Hematol.* **15**, 101–107 (2008).
97. Xie, C. & Plunkett, W. Metabolism and actions of 2-chloro-9-(2-deoxy-2-fluoro-beta-D- arabinofuranosyl)-adenine in human lymphoblastoid cells. *Cancer Res.* **55**, 2847–2852 (1995).
98. Cariveau, M. J., Stackhouse, M., Cui, X. L., Tiwari, K., Waud, W., Secrist, J. 3. & Xu, B. Clofarabine acts as radiosensitizer in vitro and in vivo by interfering with DNA damage response. *Int. J. Radiat. Oncol.* **70**, 213–220 (2008).
99. Anderson, V. R. & Perry, C. M. Fludarabine: a review of its use in non-Hodgkin's lymphoma. *Drugs* **67**, 1633–1655 (2007).
100. Heidelberger, C., Chauduri, N. K., Danneberg, P., Mooren, D., Griesbach, L., Duschinsky, R., Schnitzer, R. J., Plevin, E. & Scheiner, J. Fluorinated pyrimidines, a new class of tumor-inhibitory compounds. *Nature* **179**, 663–666 (1957).
101. World Health Organization. WHO model list of essential medicines. 18th edition. Available at <http://www.who.int/medicines/publications/essentialmedicines/en/> (2013).
102. Plunkett, W., Huang, P., Xu, Y. Z., Heinemann, V., Grunewald, R. & Gandhi, V. Gemcitabine: metabolism, mechanisms of action, and self-potential. *Semin. Oncol.* **22**, 3–10 (1995).
103. Rieger, J., Durka, S., Streffer, J., Dichgans, J. & Weller, M. Gemcitabine cytotoxicity of human malignant glioma cells: modulation by antioxidants, BCL-2 and dexamethasone. *Eur. J. Pharmacol.* **365**, 301–308 (1999).
104. Fehlauer, F., Muench, M., Smid, E. J., Slotman, B., Richter, E., van der Valk, P. & Sminia, P. Combined modality therapy of gemcitabine and irradiation on human glioma spheroids derived from cell lines and biopsy tissue. *Oncol. Rep.* **15**, 97–105 (2006).
105. Keller, A., Rackwitz, J., Cauët, E., Liévin, J., Körzdörfer, T., Rotaru, A., Gothelf, K. V., Besenbacher, F. & Bald, I. Sequence dependence of electron-

- induced DNA strand breakage revealed by DNA nanoarrays. *Sci. Rep.* **4**, 7391-1–7391-6 (2014).
106. Wang, C. R. & Lu, Q. B. Molecular mechanism of the DNA sequence selectivity of 5-halo-2'-deoxyuridines as potential radiosensitizers. *J. Am. Chem. Soc.* **132**, 14710–14713 (2010).
107. Solomun, T., Hultschig, C. & Illenberger, E. Microarray technology for the study of DNA damage by low-energy electrons. *Eur. Phys. J. D* **35**, 437–441 (2005).
108. Solomun, T., Seitz, H. & Sturm, H. DNA Damage by Low-Energy Electron Impact. Dependence on Guanine Content. *J. Phys. Chem. B* **113**, 11557–11559 (2009).
109. Andersen, E. S., Dong, M., Nielsen, M. M., Jahn, K., Subramani, R., Mamdouh, W., Golas, M. M., Sander, B., Stark, H., Oliveira, C. L. P., Pedersen, J. S., Birkedal, V., Besenbacher, F., Gothelf, K. V. & Kjems, J. Self-assembly of a nanoscale DNA box with a controllable lid. *Nature* **459**, 73–76 (2009).
110. Douglas, S. M., Dietz, H., Liedl, T., Högberg, B., Graf, F. & Shih, W. M. Self-assembly of DNA into nanoscale three-dimensional shapes. *Nature* **459**, 414–418 (2009).
111. Jiang, Q., Song, C., Nangreave, J., Liu, X., Lin, L., Qiu, D., Wang, Z.-G., Zou, G., Liang, X., Yan, H. & Ding, B. DNA origami as a carrier for circumvention of drug resistance. *J. Am. Chem. Soc.* **134**, 13396–13403 (2012).
112. Perrault, S. D. & Shih, W. M. Virus-inspired membrane encapsulation of DNA nanostructures to achieve in vivo stability. *ACS Nano* **8**, 5132–5140 (2014).
113. Bald, I. & Keller, A. Molecular Processes Studied at a Single-Molecule Level Using DNA Origami Nanostructures and Atomic Force Microscopy. *Molecules* **19**, 13803–13823 (2014).
114. Fu, J., Liu, M., Liu, Y., Woodbury, N. W. & Yan, H. Interenzyme Substrate Diffusion for an Enzyme Cascade Organized on Spatially Addressable DNA Nanostructures. *J. Am. Chem. Soc.* **134**, 5516–5519 (2012).
115. Prinz, J., Schreiber, B., Olejko, L., Oertel, J., Rackwitz, J., Keller, A. & Bald, I. DNA Origami Substrates for Highly Sensitive Surface-Enhanced Raman Scattering. *J. Phys. Chem. Lett.* **4**, 4140–4145 (2013).

116. Acuna, G. P., Moller, F. M., Holzmeister, P., Beater, S., Lalkens, B. & Tinnefeld, P. Fluorescence Enhancement at Docking Sites of DNA-Directed Self-Assembled Nanoantennas. *Science* **338**, 506–510 (2012).
117. Olejko, L., Cywinski, P. J. & Bald, I. An ion-controlled four-color fluorescent telomeric switch on DNA origami structures. *Nanoscale* **8**, 10339–10347 (2016).
118. Kuzuya, A., Sakai, Y., Yamazaki, T., Xu, Y. & Komiyama, M. Nanomechanical DNA origami 'single-molecule beacons' directly imaged by atomic force microscopy. *Nat. Commun.* **2**, 1–8 (2011).
119. Binnig, G., Quate, C. F. & Gerber, C. Atom Force Microscope. *Phys. Rev. Lett.* **56**, 930–934 (1986).
120. Howland, R. & Benatar, L. *A practical guide to scanning probe microscopy* (DIANE Publishing Company, Collingdale, PA, 1998).
121. Wiesendanger, R. *Scanning probe microscopy and spectroscopy. Methods and applications* (Cambridge University Press, Cambridge, New York, 1994).
122. Vogel, S., Rackwitz, J., Schürman, R., Prinz, J., Milosavljević, A. R., Réfrégiers, M., Giuliani, A. & Bald, I. Using DNA Origami Nanostructures To Determine Absolute Cross Sections for UV Photon-Induced DNA Strand Breakage. *J. Phys. Chem. Lett.* **6**, 4589–4593 (2015).
123. Green, N. M. Avidin. *Adv. Protein Chem.* **29**, 85–133 (1975).
124. Connolly, S. & Fitzmaurice, D. Programmed assembly of gold nanocrystals in aqueous solution. *Adv. Mater.* **11**, 1202–1205 (1999).
125. Lee, J., Govorov, A. O., Dulka, J. & Kotov, N. A. Bioconjugates of CdTe nanowires and Au nanoparticles: plasmon-exciton interactions, luminescence enhancement and collective effects. *Nano Lett.* **4**, 2323–2330 (2004).
126. Hoff, J. D., Cheng, L. J., Meyhofer, E., Guo, L. J. & Hunt, A. J. Nanoscale protein patterning by imprint lithography. *Nano Lett.* **4**, 853–857 (2004).
127. Voigt, N. V. & et al. Single-molecule chemical reactions on DNA origami. *Nat. Nanotechnol.* **5**, 200–203 (2010).
128. Helmig, S., Rotaru, A., Arian, D., Kovbasyuk, L., Arnbjerg, J., Ogilby, P. R., Kjems, J., Mokhir, A., Besenbacher, F. & Gothelf, K. V. Single molecule atomic

- force microscopy studies of photosensitized singlet oxygen behavior on a DNA origami template. *ACS Nano* **4**, 7475–7480 (2010).
129. Keller, A., Kopyra, J., Gothelf, K. V. & Bald, I. Electron-induced damage of biotin studied in the gas phase and in the condensed phase at a single-molecule level. *New J. Phys.* **15**, 083045-1–083045-14 (2013).
130. Cauët, E., Dehareng, D. & Lievin, J. Ab initio study of the ionization of the DNA bases: ionization potentials and excited states of the cations. *J. Phys. Chem. A* **110**, 9200–9211 (2006).
131. Olejko, L., Cywinski, P. J. & Bald, I. Ion-selective formation of a guanine quadruplex on DNA origami structures. *Angew. Chem. Int. Ed. Engl.* **54**, 673–677 (2015).
132. Kumar, S. V. K., Pota, T., Peri, D., Dongre, A. D. & Rao, B. J. Low energy electron induced damage to plasmid DNA pQE30. *J. Chem. Phys.* **137**, 045101-1–045101-7 (2012).
133. Mason, N. J., Smialek, M. A., Moore, S. A., Folkard, M. & Hoffmann, S. V. Probing Radiation Damage at the Molecular Level. *AIP Conference Proceedings* **876**, 3–14 (2006).
134. Gohlke, S., Abdoul-Carime, H. & Illenberger, E. Dehydrogenation of adenine induced by slow ( $< 3$  eV) electrons. *Chem. Phys. Lett.* **380**, 595–599 (2003).
135. Denifl, S., Sulzer, P., Huber, D., Zappa, F., Probst, M., Märk, T. D., Scheier, P., Injan, N., Limtrakul, J., Abouaf, R. & Dunet, H. Influence of functional groups on the site-selective dissociation of adenine upon low-energy electron attachment. *Angew. Chem. Int. Ed. Engl.* **46**, 5238–5241 (2007).
136. Kossoski, F., Kopyra, J. & Varella, M. T. do N. Anion states and fragmentation of 2-chloroadenine upon low-energy electron collisions. *Phys. Chem. Chem. Phys.* **17**, 28958–28965 (2015).
137. Rackwitz, J., Kopyra, J., Dabkowska, I., Ebel, K., Rankovic, M., Milosavljević, A. R. & Bald, I. Sensitizing DNA Towards Low-Energy Electrons with 2-Fluoroadenine. *submitted* (2016).
138. Denifl, S., Matejcik, S., Ptasinska, S., Gstir, B., Probst, M., Scheier, P., Illenberger, E. & Märk, T. D. Electron attachment to chlorouracil. A comparison between 6-CIU and 5-CIU. *J. Chem. Phys.* **12**, 704–709 (2004).

139. Bald, I., Kopyra, J. & Illenberger, E. Selective excision of C5 from D-ribose in the gas phase by low-energy electrons (0-1 eV): implications for the mechanism of DNA damage. *Angew. Chem. Int. Ed. Engl.* **45**, 4851–4855 (2006).
140. Abdoul-Carime, H., Gohlke, S. & Illenberger, E. Site-Specific Dissociation of DNA Bases by Slow Electrons at Early Stages of Irradiation. *Phys. Rev. Lett.* **92**, 168103-1–168103-4 (2004).
141. Abouaf, R. & Dunet, H. Structures in dissociative electron attachment cross-sections in thymine, uracil and halouracils. *Eur. Phys. J. D* **35**, 405–410 (2005).
142. Ptasíńska, S., Denifl, S., Grill, V., Märk, T. D., Illenberger, E. & Scheier, P. Bond- and Site-Selective Loss of H<sup>-</sup> from Pyrimidine Bases. *Phys. Rev. Lett.* **95**, 093201-1–093201-4 (2005).
143. Hanel, G., Gstir, B., Denifl, S., Scheier, P., Probst, M., Farizon, B., Farizon, M., Illenberger, E. & Märk, T. D. Electron Attachment to Uracil. Effective Destruction at Subexcitation Energies. *Phys. Rev. Lett.* **90**, 188104-1–188104-4 (2003).
144. Boudaiffa, B., Cloutier, P., Hunting, D., Huels, M. A. & Sanche, L. Cross sections for low-energy (10-50 eV) electron damage to DNA. *Radiat. Res.* **157**, 227–234 (2002).
145. Cauët, E. Unique hole-trapping property of the human telomere sequence. *J. Biomol. Struct. Dyn.* **29**, 557–561 (2011).
146. Phan, A. T., Modi, Y. S. & Patel, D. J. Two-repeat Tetrahymena Telomeric d(TGGGGTTGGGGT) Sequence Interconverts Between Asymmetric Dimeric G-quadruplexes in Solution. *J. Mol. Biol.* **338**, 93–102 (2004).
147. Phan, A. T. & Patel, D. J. Two-Repeat Human Telomeric d(TAGGGTTAGGGT) Sequence Forms Interconverting Parallel and Antiparallel G-Quadruplexes in Solution. Distinct Topologies, Thermodynamic Properties, and Folding/Unfolding Kinetics. *J. Am. Chem. Soc.* **125**, 15021–15027 (2003).



# Acknowledgements

This project was a splendid challenge, a wonderful opportunity to learn how to handle plenty of tools to construct and understand some tiny pieces of this world. None of it would have happened without my supervisor Prof. Ilko Bald. I am deeply grateful for all your support to meet this challenge.

I want to express my deepest gratitude also to the reviewers of this thesis, apl. Prof. Stephan Denifl and Prof. Heinz Sturm.

Furthermore I want to thank Ph.D. Janina Kopyra for two great weeks in Siedlce, Poland, and the opportunity to work with a sophisticated equipment for DEA gas phase experiments. The travel grant was generously given by the COST Action MP1002 “Nano-IBCT” network funding.

This project would have not been possible without the financial support by the Deutsche Forschungsgemeinschaft DFG, I am very grateful for that.

My very special thanks goes to Adrian Keller, without whom none of this would have been possible. You have not only improved my emotional well-being, but also brought structure into chaos. I am deeply indebted to you.



# Versicherung

Hiermit versichere ich, dass ich die vorliegende Arbeit ohne unzulässige Hilfe Dritter und ohne Benutzung anderer als der angegebenen Hilfsmittel angefertigt habe; die aus fremden Quellen direkt oder indirekt übernommenen Gedanken sind als solche kenntlich gemacht. Die Arbeit wurde bisher weder im Inland noch im Ausland in gleicher oder ähnlicher Form einer anderen Prüfungsbehörde vorgelegt.

Ich erkenne die Promotionsordnung der Universität Potsdam an.

Potsdam, 06.06.2016

*Jenny Rackwitz*



## Nachweis über Lehrerfahrung und Seminarteilnahme

### Lehrerfahrung

Aus dem Modul „Physikalische Chemie für Nebenfachstudenten“ an der Universität Potsdam wurde je eine Übungsgruppe von Frau Jenny Rackwitz mit 2 SWS in den Sommersemestern 2013, 2014 und 2015 geleitet.

### Seminarteilnahme

Frau Jenny Rackwitz hat während der gesamten Promotionszeit an den im Semester wöchentlich stattfindenden Seminaren der Arbeitsgruppen „Optische Spektroskopie und Chemical Imaging“ und „Physikalische Chemie“ teilgenommen. Im Seminar der erstgenannten Arbeitsgruppe wurde einmal im Semester der aktuelle Stand der wissenschaftlichen Arbeit in Form eines Vortrages präsentiert, anderenfalls einmal pro Jahr.

Hiermit bestätige ich die Angaben über Lehrerfahrung und Seminarteilnahme.

---

Jenny Rackwitz

---

JProf. Dr. Ilko Bald (Hauptbetreuer)



## Veröffentlichungen

1. **Low-energy electron induced damage in telomere derived DNA sequences – Influence of DNA sequence and topology;** J. Rackwitz, I. Bald, [Manuskript in Vorbereitung].
2. **A novel setup for oligonucleotide irradiation with LEE;** J. Rackwitz, I. Bald, [Manuskript in Vorbereitung].
3. **Sensitizing DNA Towards Low-Energy Electrons with 2-Fluoroadenine;** J. Rackwitz, J. Kopyra, I. Dabkowska, K. Ebel, M. Lj. Ranković, A. R. Milosavljević, I. Bald, [Revision submitted to *Angewandte Chemie*].
4. **Using DNA Origami Nanostructures To Determine Absolute Cross Sections for UV Photon-Induced DNA Strand Breakage;** S. Vogel, J. Rackwitz, R. Schürman, J. Prinz, A. R. Milosavljević, M. Réfrégiers, A. Giuliani, I. Bald, *J. Phys. Chem. Lett.* **2015**, *6*, 4589.
5. **Sequence dependence of electron-induced DNA strand breakage revealed by DNA nanoarrays;** A. Keller, J. Rackwitz, E. Cauët, J. Liévin, T. Körzdörfer, A. Rotaru, K.V. Gothelf, F. Besenbacher, I. Bald, *Sci. Rep.* **2014**, *4*, 7391.
6. **DNA Origami Substrates for Highly Sensitive Surface-Enhanced Raman Scattering;** J. Prinz, B. Schreiber, L. Olejko, J. Oertel, J. Rackwitz, A. Keller, I. Bald, *J. Phys. Chem. Lett.* **2013**, *4*, 4140.
7. **Structurally Diverse Polyamides Obtained from Monomers Derived via the Ugi Multicomponent Reaction;** Kreye, O., Türünç, O., Sehlinger, A., Rackwitz, J., Meier, M. *Chem. Eur. J.* **2012**, *18*, 5767.

## Konferenzbeiträge

- |                 |  |
|-----------------|--|
| 21 – 28/07/2015 | Poster: „Novel approaches to study low-energy electron-induced damage to DNA oligonucleotides“;<br>„ICPEAC“ Konferenz in Toledo                  |
| 16 – 20/07/2015 | eingeladener Vortrag: „ Novel approaches to study low-energy electron-induced damage to DNA oligonucleotides“;<br>„POSMOL“ Konferenz in Lissabon |
| 27 – 31/10/2014 | Poster: “Dissociative electron attachment to 2-Fluoroadenine“;<br>„Nano IBCT“ Konferenz in Boppard am Rhein                                      |
| 26 – 30/08/2014 | Poster: “Dissociative electron attachment to 2-Fluoroadenine“;<br>„SPIG“ Konferenz in Belgrad  |
| 29 – 31/05/2014 | Poster: “Sequence dependence of electron induced DNA strand breakage revealed by DNA nanoarrays“;<br>„Bunsentagung“ Konferenz in Hamburg         |
| 20 – 24/05/2013 | Poster: „Novel approaches to study low-energy electron-induced damage to DNA oligonucleotides“;<br>„Nano IBCT“ Konferenz in Sopot, Danzig        |